Charge State Control of Single Nitrogen-Vacancy Centers in Diamond

YUKI DOI

MARCH 2016

Charge State Control of Single Nitrogen-Vacancy Centers in Diamond

A dissertation submitted to
THE GRADUATE SCHOOL OF ENGINEERING SCIENCE
OSAKA UNIVERSITY
in partial fulfillment of the requirements for the degree of
DOCTOR OF PHILOSOPHY IN ENGINEERING

BY

YUKI DOI

MARCH 2016

Abstract

Quantum information in which spin is used as a source of non-classical computation and communication, attracts considerable interest. A long spin coherence (T_2) are required toward quantum processing. In addition, small spectral diffusion of single photon for realization of quantum cryptography and building quantum network is needed.

The nitrogen-vacancy center (NV) in diamond have long T_2 (up to several milliseconds at room temperature) and become single-photon emitter. Now a days, optically induced charge state interconversion on NV significantly extend T_2 of proximal nuclear spin owing to hyperfine interaction is weaken by motion narrowing. Theory predicts that T_2 exceeding 1 min with preventing heating of diamond due to high laser power excitation. This demonstration show potential of charge state and its non-optical control for spin properties of the NV center. Despite optical illumination is essential for NV to initialize and readout spin, optically induced charge state interconversion causes error in quantum control and spectral diffusion in emitted single photons.

In this study, charge state of single NV centers are deterministically controlled by non-optical method. Charge state of single NVs formed in the intrinsic layer of *p*-*i*-*n* diode are modulated by current injection. Transition rate and its dependence on current is revealed. Recent controllable direction of charge state is limited; however this non-optical charge state control on spin-active negatively charged state (NV^-) open the new way to spin related experiments. This study also realize purely populated charge state on the single NVs in phosphorus doped *n*-type diamond. Charge state is perfectly stabilized into NV^- state even under optical illumination (1 µW, 593 nm). After NV^- charge state is disturbed by strong laser excitation, state recovered to NV^- state under dark condition. This result pave the way to the single spin manipulation in high efficiency and suppress spectral diffusion of single emitted photons.

概要

近年、スピンを情報処理や通信に用いる量子情報が注目されている。当分野では量子情報処理の実現に向けて長いコヒーレンス時間 (T_2) を持つスピンが求められている。また量子暗号通信や量子ネットワーク形成のためにスペクトル拡散の小さい単一光子が要求される。ダイヤモンド中の窒素–空孔複合体中心 (NV 中心) は室温で比較的長い T_2 を持ち、単一光子源としての性質を持つことから研究が盛んに行われている。近年、光励起による NV 中心の電荷数（電荷状態）の変化が NV 中心と結合した核スピンの T_2 を大きく延伸させることがわかった。この際、光励起による温度上昇がなければ、理論上 1 分を超える T_2 が期待される。このようなスピンとの関連から、光励起に代わる手法での電荷状態制御は大きな可能性を秘めている。また光励起は NV 中心におけるスピンの初期化と検出に欠かせないが確率的な電荷状態の変化を起こす。これは光励起後の量子制御におけるエラーの原因となる。また単一光子のスペクトルに不均一広がりを生じる。

本研究では光励起に代わる手法としてダイヤモンド中への電流注入により、単一 NV 中心の電荷状態を制御した。電荷状態の非破壊測定を通じて、変化レートが電流に比例すること等を解明した。現時点では、制御の方向が一方向に限定されるが、 光励起以外の手法であること、スピンが利用できる単一 NV^- 電荷状態を制御したこと、具体的なレート等が明らかになったことで将来的な研究の広がりが期待される。 加えて本研究ではリンドナーを添加した別のダイヤモンド薄膜中において、電荷状態が NV^- へ安定化された単一 NV 中心を実現した。この NV 中心は光励起下（波長: 593 nm, 強度: 1 µW）においても電荷状態が変化しない。また強い光励起によって電荷状態の変化が引き起こされても、その後 $0.28\,\mathrm{ms}^{-1}$ のレートで完全に NV^- へと回復することがわかった。この成果は単一スピン操作の精度、並びに単一光子のスペクトルの安定性向上に繋がる。

Contents

List of Figures

List of Tables

List of Abbreviations

arb. units	arbitrary units
B	boron
C	carbon
cps	count per second
CVD	chemical vapor deposition
cw	continuous wave
ΔI_{PL}	difference in PL intensity
EL	electroluminescence
ESR	electron spin resonance
fluor.	fluorescence, fluorescent
γ	total rate (inverse of a time constant of transition)
γ_{-0}	ionization (from NV^- to NV^0) rate
γ_{0-}	recombination/recharge (from NV^0 to NV^-) rate
$g^{(2)}(\tau)$	second-order autocorrelation function
HTHP	high-temperature high-pressure
ISC	intersystem crossing
init.	initialization
I_F	forward current
I_R	reverse current
I_{EL}	electroluminescence intensity
I_{PL}	photoluminescence/fluorescence intensity
mw	microwave
MR	magnetic resonance
N	nitrogen
NA	numerical aperture
NMR	nuclear magnetic resonance
NV	nitrogen-vacancy center
NV^0	neutral charge state of nitrogen-vacancy center
NV^-	negatively charged state of nitrogen-vacancy center
ODMR	optically detected magnetic resonance
p	population probability of charge-state
$p(0)$	population probability of charge-state at initial state
p_-	population probability of NV^- charge state
p_0	population probability of NV^0 charge state
p_{eq}	population probability of charge-state at a state of the equilibrium

P	phosphorus
P	excitation laser power
FAM	fluorescence averaging measurement
PL	photoluminescence
ppb	part per billion ($1\,\mathrm{ppb} = 1.76 \times 10^{14}\,\mathrm{cm}^{-3}$ for diamond)
ppm	part per million ($1\,\mathrm{ppm} = 1.76 \times 10^{17}\,\mathrm{cm}^{-3}$ for diamond)
Q_s	stored charge
read.	readout
rf	radio frequency
SCM	single-shot charge-state measurement
t_{dark}	dark time
τ	time constant (inverse of a rate of transition)
τ	two photon delay, pulse length
τ_L	lifetime of carriers
V_F	forward bias voltage
V_R	reverse bias voltage
ZFS	zero-field splitting
ZPL	zero-phonon line
T_1	longitudinal spin relaxation time
T_2	transverse spin relaxation time
T_2^*	inverse inhomogeneous broadening; decay constant of FID

1. Introduction

Qubit Spin, quantum nature of subatomic particles and photons, enhance computational power for particular tasks as "qubit (quantum bit)", a source of non-classical processing [1–4]. As for communication, flying qubits (e.g. photons) are able to securely transfer quantum states to outside the system assured by fundamental laws of physics [5, 6]. With respect to sensing of small magnet, electron qubit has a potential to sense the faint magnetic moment of a single electronic or nuclear spin [7]. Imaging nuclear magnetism on the nanometer scale would allow to researchers to have new knowledge for chemical materials and dynamics in the living cells.

Since proposal of quantum computation [8], qubits have been realized on various physical systems; linear optical circuits [9, 10], trapped atoms [11, 12], nuclear magnetic resonance (NMR) [13–15], quantum dots [16, 17], and superconductors [18–20]. For those platforms of qubits, protecting qubits from decoherence is a matter of concern. Coherence of qubits can be destroying or decaying to interact with thermal environment. Trapped atoms and ions show coherence time as long as minutes; however they require complex systems for laser cooling and high vacuum. For other systems, ensembles of electronic and nuclear spins mark a long coherence time in bulk electron spin resonance (ESR) and NMR. However, individual preparation and addressing of spins are challenging. Therefore, achievement of long coherence time on the system which has high accessibility and scalability is common task for quantum physics.

The nitrogen-vacancy center in diamond The quantum system studied in this work is one of the point defects in diamond, the nitrogen-vacancy center (NV). A substitutional nitrogen atom next to a carbon vacancy form this structure in the diamond lattice. The NV has well-isolated electron and nuclear spins which can be readout via optical fluorescence. They record spin coherence time as long as 1.8 ms even under room temperature [21]. Strong emission of single photons by optical excitation supports high accessibility. However, longer coherence time and stability of photon energy is crucial in order to perform complex quantum gate operations and two-photon interference to connect among NVs [22].

This study focused on the charge state of the NV to improve versatility of qubits in the solid-state. Charge state is a different state of the NV in terms of the number of electrons reside in a single one. The most exploited one is negatively charged one (NV^-) which has 6 electrons in its structure. The second well-known state is neutral charge state (NV^0) which has 5 electrons. Charge state is strongly related to spin and photon of

the NV. One of the novel recent development in the charge-state is extended coherence time of proximal nuclear spin over 1 s using charge-state switching [23]. Charge state interconversion induces by strong laser illumination weaken hyperfine interaction among electron and nuclear. Such high power laser increase temperature of diamond and it causes decoherence on spin. Thus, first motivation is non-optical, electrical control of charge state, which has a potential to extend nuclear spin coherence time over 1 min owing to the prediction [23] and higher efficiency of charge state conversion via electron-electron interaction. Present works of non-optical control of charge state [24–27] lack quantitative information of switching speed and fidelity of control. These parameters are essential for applications of charge state. Thus investigation on non-optical method pave the way to extract potential of the NV.

Another interest in this study is stabilization of charge state to improve spin control efficiency and stability of photon energy. Spin initialization and readout via optical fluorescence is only available on NV^- charge state to date; however charge state interconversion, reduces the fidelity of spin operation [28] and causes unsuitability of photon energy (position of zero-phonon line (ZPL)) [29], is inevitable during optical illumination. Present works on stabilization of NV^- is performed by means of destructive measurement of charge state [27, 30–33]. Thus charge state population is not available and deterministic control is not achieved.

Thesis outline The non-optical controls of charge state are performed by using a *p*-*i*-*n* diamond diode and on phosphorus-doped *n*-type diamond layers. In both experiments, charge states of NVs are measured non-destructively. As for *p*-*i*-*n* diode, single NVs are formed in the *i*-layer and hole carriers are injected into them. Recombination of electron and hole carriers occurs at the NVs, then NV^- is ionize to NV^0, deterministically. This study gives the operation speed and show high efficiency of operation using electrical method. For stabilization of charge state, single NVs are formed in phosphorus doped *n*-type diamond layers. Thermally activated electrons from phosphorus donors stabilize NV^- charge state under dark condition. Under laser excitation (1 µW, 593 nm), photon emission from purely populated NV^- is detected.

This thesis consists of following chapters exclude the introduction and appendices. Chapter 2 explains properties of diamond and the NV. Chapter 3 introduce experimental setup (confocal microscope) and how to measure charge state and shortly explain spin resonance measurements. Chapter 4 shows experimental results and discussions of charge state control by using *p*-*i*-*n* diode. Chapter 5 exhibits purely populated NV^- charge state achieved on *n*-type diamond layers and discuss population of NV^- under arbitrary illumination power.

2. Single nitrogen-vacancy center in diamond

This chapter focused on the first of all to diamond as a host material of defects, second to the charge state and related phenomenon on the NV, third to the spin and optical properties of the nitrogen-vacancy center (NV). At last of chapter explains the experimental setup for fluorescence and charge-state detection of the individual single NVs, and shortly introduces spin resonance measurements.

2.1. Diamond

Lattice structure of diamond has highly symmetry and tight bounding. It is resulting extreme properties in the various aspect of applications. Due to the rigidity of the diamond lattice and the small carbon mass, the Debye temperature is unusually large (2220 K) [34]. As a result the phonon density is low and the electron-phonon coupling is small even under ambient conditions. This extend transverse spin relaxation time (T_2) of NV to 1.8 ms under room temperature experiments [21]. In naturally, diamonds are formed in the very deep from the surface of the earth. Almost such bare diamonds contains significant amount of impurities, nitrogen or boron. These contains are used to classify the types of diamond which is mentioned in the section 2.1.1. Diamond has excellent physical and electrical properties, e.g. high conductivity of carriers (660–4500 $\mathrm{cm^2\,V^{-1}\,s^{-1}}$), and high breakdown voltage (10–20 $\mathrm{MV\,cm^{-1}}$) [35]. However, relatively small dielectric constant (5.7) compared with other semiconductors (e.g. silicon: 11.8, SiC: 9.6, GaN: 9) results large ionization energy of donors and acceptors[1] (see figure 2.2).

All of diamond samples used in this studies are fabricated by the microwave plasma-enhanced chemical vapor deposition (CVD) technique. This technique uses reaction of methane (CH_4) and hydrogen (H_2) in plasma at low pressure (∼0.06–0.1 atm). Growth of diamond layer proceed on diamond substrate (typically commercially available) with temperature of ∼800–900 °C. The n- and p-type diamond layers can also be fabricated by the same technique to use impurities gas. Diborane (B_2H_6) and phosphine (PH_3) are used for p- and n-type layers synthesis, respectively. Details of sample synthesis are individually described in each section.

[1] Bonding energy of electron of impurities is inversely proportional to the square of dielectric constant [36].

Table 2.1.: Types of diamond regarding their impurities and their aggregations.

type	N content	feature	[N] in ppm
Ia	high	aggregated N (N pairs or 4N + V)	< 3000
Ib	high	isolated single N	< 500
IIa	low	very low N content	$< \sim 1$
IIb	low	boron content	$< \sim 1$

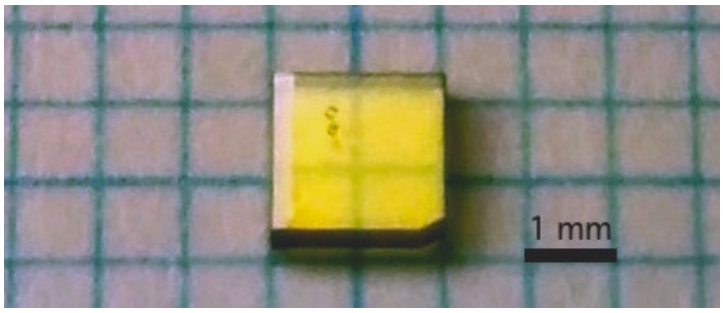

Figure 2.1.: Picture of a CVD synthesized diamond. This diamond contains large amount of nitrogen atoms (type Ib) which assume a color of yellow.

2.1.1. Categorization

Diamond is classified into 2 types, type I and type II, regarding their nitrogen impurities [37]. Type I diamond contains nitrogen atoms as its most abundant impurities. Almost all natural diamonds are classified into type I. Type II diamond contains few amount of nitrogen atoms. Type I diamonds are divided into types Ia and Ib, regarding their aggregation of nitrogen atoms. Type Ia diamonds contain aggregated nitrogen impurities which consist of pairs of nitrogen atoms[2] or are made up of four nitrogen atoms around a vacancy.[3] In type Ib, nitrogen atoms is isolated. Type II diamonds are divided into types IIa and IIb. Type IIa diamond contains few number of nitrogen or boron impurities. Type IIb diamonds contain boron impurities. It is thought that boron atoms are isolated and replace carbon in the diamond lattice. Type IIb diamonds are showing electrical conductivity due to boron impurities. Classifications and impurities content is summarized in table 2.1. Impurity in diamond assume various colors in diamond. For example, large amount of nitrogen atoms assume a yellow color in diamond (figure 2.1). Impurities also related to the functional defects in diamond lattice [38].

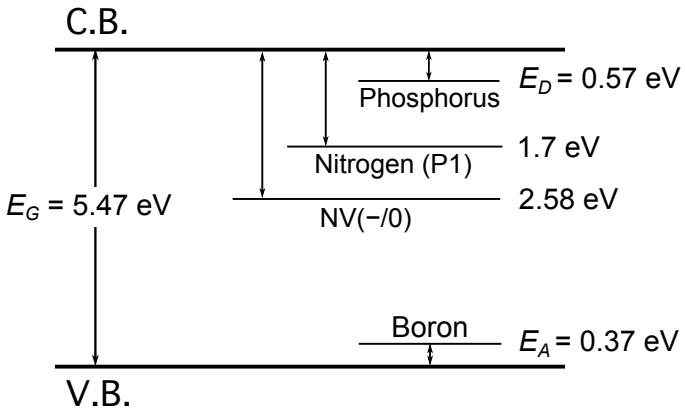

Figure 2.2.: Energy level diagram of various dopants in the bandgap of diamond. The ground state of NV^- is labeled with $NV(-/0)$. Energy levels of phosphorus, nitrogen, and NV are displayed with respect to conduction band minimum (C.B.). Energy level of boron is depicted with respect to valence band maximum (V.B.).

2.1.2. The *n*- and *p*-type diamond

This study use n- and p-type diamond to control charge-state of the NV. Figure 2.2 is an energy level diagram of nitrogen, phosphorus donors, and ground state of negatively charged state of nitrogen-vacancy center (NV^-) (labeled $NV(-/0)$) in diamond. The charge state of defects in diamond depends on the position of the Fermi level which are determined by the energy level of impurities and extra energy levels at the outside of the bulk. When the Fermi level positions above the energy level of defects, defects are charged. Energy level of impurities also determines the conduction properties of diamond as regarding the number of electron and hole carriers. Nitrogen donors (P1 center) attribute to conduction and free electrons in diamond. However, only few number of electrons are excited due to its deep donor level ($E_D = 1.7\,\mathrm{eV}$ [39]).

Phosphorus is shallower donor than nitrogen atoms in diamond ($E_D = 0.57\,\mathrm{eV}$). Nevertheless phosphorus is deep-lying compared with in silicon (in silicon, ionization energy $= 0.045\,\mathrm{eV}$), but phosphorus-doped diamond shows properties of n-type semiconductor. Concentration of phosphorus is controlled by the concentration ratio of phosphine and methane ($[PH_3]/[CH_4]$) in the gas phase during CVD synthesis. Phosphorus incorporation in (111) diamond has been controlled between 5×10^{17} and $2 \times 10^{20}\,\mathrm{cm}^{-3}$ [40]. Incorporation for (001) direction is two orders of magnitude smaller than that on (111) direction (between 5×10^{17} and $8 \times 10^{18}\,\mathrm{cm}^{-3}$). Thus heavily doping on (001) direction has been a challenging task. The (111) direction is a direction to easily incorporate not only phosphorus but also other atoms, e.g. nitrogen. Thus (001) orientation is preferred to reduce unwanted defects creations.

[2]This type of aggregation is called type IaA.
[3]This type of aggregation is called type IaB.

The electron concentration, n, in n-type semiconductor can be obtained as follows [41, 42]:

$$\frac{n\,(n+N_A)}{N_D-N_A-n} = \frac{N_C}{g_d}\exp\left(-\frac{E_D}{k_BT}\right) \tag{2.1}$$

$$\text{with } N_C = 2\left[\frac{2\pi m_e^* k_B T}{h^2}\right]^{3/2}, \tag{2.2}$$

where N_A and N_D are concentrations of acceptor and donor atoms, respectively. N_C is a density of state of the conduction band, $m_e^* = 1.81m_0$ is the electron effective mass [43], where m_0 is a free electron mass, $g_d = 2$ is a degeneration of the donor level in diamond, and h is a Planck constant.

For diamond, boron atom acts as acceptor. Boron can be found in natural diamond classified as type IIb (see table 2.1). In the same way as electron concentration, the hole concentration, p, in the p-type semiconductor can be written as follows [44]:

$$\frac{p\,(p+N_D)}{N_A-N_D-p} = \frac{N_V}{g_a}\exp\left(-\frac{E_A}{k_BT}\right) \tag{2.3}$$

$$\text{with } N_V = 2\left[\frac{2\pi m_h^* k_B T}{h^2}\right]^{3/2}, \tag{2.4}$$

where N_V is a density of state of the valence band, $m_h^* = 0.74m_0$ is the hole effective mass [45], $g_a = 4$ (or 6 at high temperature) is a degeneration of the acceptor level in diamond [46].

The overestimated value of electron concentration is derived from equation (2.1) for n-type diamond compared with experimental results. To obtain a more comprehensive understanding of the electrical conduction properties, the effect of carrier compensation should be taken into account. The compensation ration η is given by N_A/N_D, in which phosphorus-doped diamond has been several percent in (111) and approximately 50 % in (001) diamond. For example, Stenger et al. reported η of 0.11 in (111) diamond with $[\mathrm{P}] = 1.7\times10^{18}\,\mathrm{cm}^{-3}$ [41]. At room temperature, compensation dominantly affect to the carrier concentration. However to date, compensating centers have not yet been identified in phosphorus-doped diamond.

The reported value of activation energies of phosphorus and boron are listed up in tables 2.2 and 2.3. The activation energy of boron is well established, approximately $E_A = 0.37\,\mathrm{eV}$. For phosphorus, activation energy depends on measurement methods and its concentration. In this study the concentration of phosphorus in n-type layers are close to the value used in reference [47]. Thus the value $E_D = 0.57\,\mathrm{eV}$ is consistently used in discussions.

Table 2.2.: Activation energy of phosphorus donors (E_D) in diamond films.

E_D (eV)	[P] (cm^{-3})	measurement
0.43 [48]	2.5×10^{19}	Hall effect measurement
0.46 [49]	2.5×10^{19}	Hall effect measurement
0.53 [50]	n/a (cf. $[PH_3] \simeq 10^{19}$)	impedance spectra
0.56 [51]	10^{19}–10^{20}	photocurrent spectroscopy
0.57 [47]	7×10^{16}	Hall effect measurement
0.58 [52]	PH_3/CH_4: 1–10 %	Hall effect measurement
0.60 [45]	n/a	infrared absorption spectroscopy
0.63 [53]	10^{18}–10^{19}	cathodoluminescence spectra

Table 2.3.: Activation energy of boron acceptors (E_A) in diamond.

E_A (eV)	[B] (cm^{-3})	measurement
0.3680 ± 0.0015 [54]	n/a (natural diamond)	Hall effect measurement
0.368 [55]	10^{18}–10^{19}	four-point probe measurement

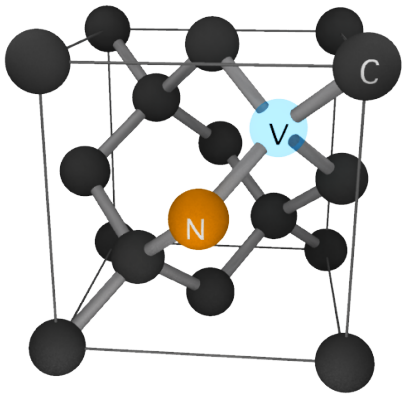

Figure 2.3.: Crystallographic structure of the NV in the diamond lattice. An unit cell of the diamond contains an NV. The substitutional nitrogen atom is labeled with "N" and the atomic vacancy is marked with "V". The dark gray spheres are carbon atoms, marked with "C".

Table 2.4.: Possible charge states of the NV.

state	# electrons	zero-phonon line	ground state spin	ref.
NV^+	4	optically inactive	?	[58–60]
NV^0	5	575 nm	$S = 1/2$	[61–64]
NV^-	6	637 nm	$S = 1$	[65–68]
NV^{2-}	7	optically inactive	?	[59, 69]

2.2. The nitrogen-vacancy center

The NV is a point defect in diamond consists of a substitutional nitrogen atom and an adjacent vacancy site. The structure of NV in diamond lattice is depicted in figure 2.3. The NVs are naturally formed in diamond layers during CVD growth by incorporation of nitrogen atoms as impurities in a chamber [56]. Incorporated nitrogen does not form NV as-is, high temperature is needed to make NVs in diamond. The temperature condition of CVD is suitable for NV generation. The NV can also be formed by the ion implantation of nitrogen atoms and annealing [57]. The ion implantation generate vacancy during the process ions are injected in the bulk diamond. During annealing (several hours at ∼600 °C) the vacancies migrate to nitrogen site and form NV.

2.2.1. Charge state

The possible charge states of the NV are listed up in the table 2.4. The charge transition level for NV^+ and NV^{2-} are stated in reference [70]. The position of ground state of NV^- and NV^0 are reported as 2.94 eV [71] and 1.2 eV [72] below the conduction band. This section only focused on NV^- and NV^0 charge states and discuss interconversion among

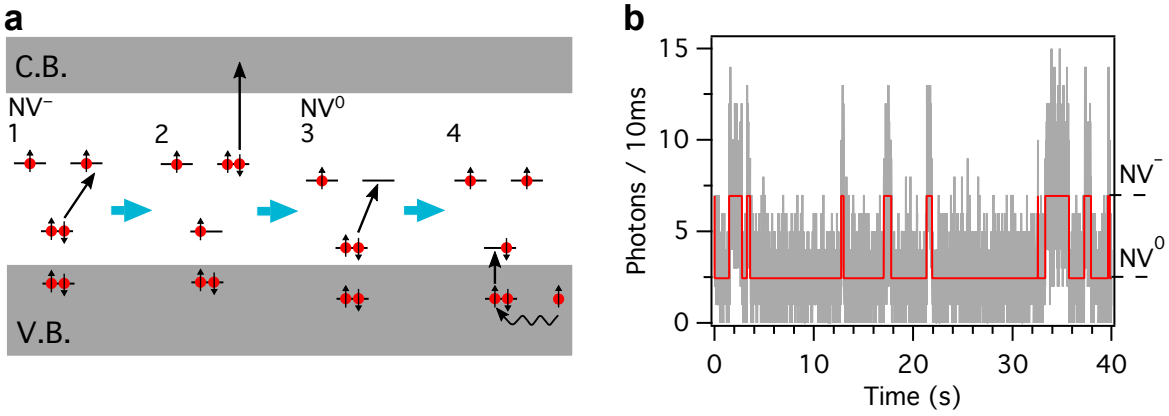

Figure 2.4.: Schematic picture and time trace of the charge state interconversion a, Charge state conversion process under optical illumination for the negatively charged (NV^-) and neutral charge (NV^0) state of a NV. 1, NV^- is excited by the first photon and 2, the second photon excites an electron into the conduction band (C.B.) thus NV turned into NV^0 (two-photon process). 3, within the neutral state, the first photon excite NV^0 and the second photon excites an electron from the lower energy level. 4, finally an electron migrates from valence band (V.B.) to the NV. Consequently the charge state turns back to NV^-. **b,** Time trace of fluorescence of a single NV under the weak (1 µW) orange laser (593 nm) excitation, in intrinsic (undoped) diamond. Bursts of photons are observed along with the stochastic charge state interconversion. Average lifetime of NV^0 and NV^- are 3.27 and 0.644 s, respectively in the measurement.

them under optical illumination. Nitrogen-vacancy complex has 5 electrons in itself, and an extra electron from outside of the structure is needed to form negatively charge state, NV^-. An electron might comes from a donor defects (e.g. substitutional nitrogen centers [73, 74]) or by two-photon conversion from NV^0 to NV^-. Figure 2.4a is process of the charge conversions for negative and neutral states of NV under optical illumination [29, 71]. The details are described in the figure caption. Generally used green laser (532 nm) can excite ground state electron of both NV^0 and NV^- thus charge state can easily transit among them (see ZPL in table 2.4). However orange laser (593 nm) hardly excite ground state of NV^0 because ZPL and absorption is higher than wavelength of 593 nm. Thus weak excitation by orange laser becomes charge state transition very slow then it can be recorded as transition of photoluminescence/fluorescence intensity (I_{PL}) in time trace. Figure 2.4b is a time trace of fluorescence of single NV under orange laser excitation with 1 µW. Using optical filter at 645–675 nm can selectively detect the fluorescence of NV^- charge state. The fluorescence of NV^- appears as highly photon counts and NV^0 is detected as lower counts. From this measurement, ionization (from NV^- to NV^0) rate (γ_{-0}) and recombination/recharge (from NV^0 to NV^-) rate (γ_{0-}) can be derived as follows:

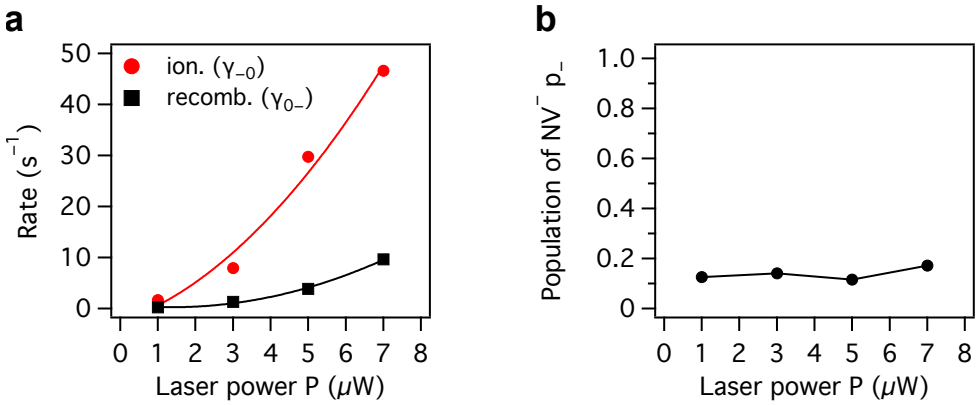

Figure 2.5.: Laser power dependence of charge state transition. **a,** Ionization (ion.) and recombination (recomb.) rates quadratically depend on illumination power P of orange laser. The solid carves are parabola fits ($f(P) = aP + bP^2$). **b,** Laser power dependence of NV^- population (p_-) under orange laser excitation calculated by $p_- = \gamma_{0-}/(\gamma_{-0} + \gamma_{0-})$.

$$\gamma_{-0} = \frac{1}{\tau_{NV^-}}, \tag{2.5}$$

$$\gamma_{0-} = \frac{1}{\tau_{NV^0}}, \tag{2.6}$$

where τ_{NV^-} and τ_{NV^0} are average lifetime of NV^- and NV^0, respectively. From figure 2.4b, ionization and recombination rates are, $\gamma_{-0} = 1/\tau_{NV^-} = 1/0.664 = 1.51\,s^{-1}$ and $\gamma_{0-} = 1/\tau_{NV^0} = 1/3.27 = 0.306\,s^{-1}$, respectively. Figure 2.5a is a laser power dependence of these rates measured under orange laser illumination. These rates show quadratic dependence to laser power because charge state transition process involve two-photon absorption. From transition rates, population probability of NV^- charge state (p_-) and population probability of NV^0 charge state (p_0) are obtained as follows:

$$p_- = \frac{\gamma_{0-}}{\gamma_{-0} + \gamma_{0-}}, \tag{2.7}$$

$$p_0 = \frac{\gamma_{-0}}{\gamma_{-0} + \gamma_{0-}}, \tag{2.8}$$

because both ionization and recombination rates quadratically depend on the laser power, population probability are constant to laser power is shown in figure 2.5b.

Equations (2.7) and (2.8) can only be adapted to state of the equilibrium. To consider charge transition under non equilibrium state, simple two-level diagram of charge state population (p_- and p_0) is introduced. In this model, two states are connected with γ_{-0} and γ_{0-} (occurrence of transition in the unit time). Thus the charge state dynamics of NV can be written by the following two first-order linear rate equations:

$$\begin{pmatrix} \dot{p}_-(t) \\ \dot{p}_0(t) \end{pmatrix} = \underbrace{\begin{pmatrix} -\gamma_{-0} & \gamma_{0-} \\ \gamma_{-0} & -\gamma_{0-} \end{pmatrix}}_{A} \underbrace{\begin{pmatrix} p_-(t) \\ p_0(t) \end{pmatrix}}_{p(t)}, \tag{2.9}$$

where $p_-(t)$ and $p_0(t)$ are time dependent population probabilities of NV^- and NV^0, respectively. Equation (2.9) can be solved to diagonalize A. Consequently matrix $p(t)$ can be written as follow with the population probability of charge-state at initial state for NV^- and NV^0 ($p_-(0)$ and $p_0(0)$, respectively):

$$\begin{pmatrix} p_-(t) \\ p_0(t) \end{pmatrix} = \frac{1}{\gamma_{-0}+\gamma_{0-}} \begin{pmatrix} \gamma_{0-} \\ \gamma_{-0} \end{pmatrix} + \begin{pmatrix} 1 \\ -1 \end{pmatrix} \frac{p_-(0)\gamma_{-0} - p_0(0)\gamma_{0-}}{\gamma_{-0}+\gamma_{0-}} \exp\left\{-\left(\gamma_{-0}+\gamma_{0-}\right)t\right\}. \tag{2.10}$$

The derivation of equation (2.10) is explained in appendix C.

The enough time after, $p_-(t)$ and $p_0(t)$ reach to population probability of charge-state at a state of the equilibrium (p_-^{eq} and p_0^{eq}, respectively) as follows:

$$\begin{pmatrix} p_-^{\mathrm{eq}} \\ p_0^{\mathrm{eq}} \end{pmatrix} = \begin{pmatrix} p_-(t) \\ p_0(t) \end{pmatrix}\Big|_{t\to\infty} = \frac{1}{\gamma_{-0}+\gamma_{0-}} \begin{pmatrix} \gamma_{0-} \\ \gamma_{-0} \end{pmatrix}, \tag{2.11}$$

here this equation shows that the equilibrium populations do not depend on their initial states ($p_-(0)$ and $p_0(0)$) only be determined by the ratio of transition rates. Equation (2.11) equals to equations (2.7) and (2.8). In addition, following important relation is derived from equation (2.11):

$$\begin{pmatrix} \gamma_{0-} \\ \gamma_{-0} \end{pmatrix} = \begin{pmatrix} p_-^{\mathrm{eq}} \\ p_0^{\mathrm{eq}} \end{pmatrix} \underbrace{(\gamma_{-0}+\gamma_{0-})}_{\gamma}, \tag{2.12}$$

this relation is used to extract one-directional, ionization and recombination rates from averaged rate measurements when p_-^{eq} and p_0^{eq} are known in the system. Here $\gamma = \gamma_{-0}+\gamma_{0-}$ is called as "total rate".

2.2.2. Electronic and optical properties

NV^-

Figures 2.6a-b are the electronic levels and level structures of the NV^- within the bandgap of diamond. The left side of figure 2.6a, a ground state occupation of 6 electrons in 4 orbitals is displayed. The lowest state $a_1^{'}$ is lying in the valence band. This state and the second lowest state (a_1) are fully occupied in ground state. These states have a symmetry of a_1. The highest two states are degenerate into e_x and e_y orbitals of e symmetry. The remaining electrons occupy the two e symmetry. Therefore electrons form a triplet ($S = 1$). The right side of figure 2.6a is an excited state of the NV^-.

One electron are excited from a_1 state to one of the e state. The exited state also form triplet. Figure 2.6b is a level structure of NV^- state. The spin state of ground ($^3A_2$) and excited state (^3E) are splitting by spin-spin interaction between unpaired electrons under no magnetic field ($D_{gs} \simeq 2.87\,\mathrm{GHz}$) [75]. Irradiated photons excite an electron from the ground to corresponding vibrational mode (phonon sideband) of the excited state is indicated by green arrows. When an electron is excited from $m_s = 0$, the electron decays to $m_s = 0$ state of the excited state. Consequently it decays to the most likely vibrational mode in the ground state. This vibrational mode contribute to the broadening of fluorescence spectra (phonon sideband). When an electron is in $m_s = \pm 1$ state, an electron is excited to the $m_s = \pm 1$ state of the excited state. In this path the another channel to the metastable state is available by inter system crossing (ISC), assisted by spin-orbit interaction. A decaying to and from metastable state is non-radiative. In addition the transition at the inside of the metastable state have a fluorescence at infrared wavelength (1042 nm [76]), but this wavelength is beyond the detectable region of detectors. Thus fluorescence of this decay path is weaker than decay path from $m_s = 0$. This enable us to detect single spin state at the ground state of NV^- via optical fluorescence. The ZPL of this state is assigned to 637 nm [65, 77]. A spin Hamiltonian of NV^- state in the ground state is written as $H_{tot} = H_S + H_{SI} + H_I$ [76]. Here H_S is a term of an interaction between two electrons, H_{SI} is a hyperfine term with nitrogen spin ($I = 1$ for ^{14}N, 99.6 % of natural abundance), H_I is the nuclear term.

$$\begin{cases} H_S = D_{gs} S_z^2 + E(S_x^2 - S_y^2) + g_s \mu_B \vec{B} \cdot \vec{S} \\ H_{SI} = A_\parallel S_z I_z + A_\perp (S_x I_x + S_y I_y) \\ H_I = P I_z^2 - g_I \mu_N \vec{B} \cdot \vec{S}, \end{cases} \tag{2.13}$$

the meanings and values of parameters appear in the Hamiltonian are listed up in table 2.5. The most important factor for this study is zero-field splitting (ZFS) parameter, $D_{gs} \simeq 2.87\,\mathrm{GHz}$. Spin-spin interaction among two unpaired electrons splits ground state spin without external magnetic field. Due to other factors, the energy level of the ground state of NV^- split by external magnetic field and proximal nuclear spins (hyperfine interaction). Schematic illustration of splittings are shown in figure 2.6d. At the situation that the nitrogen nuclear is surrounded by ^{13}C, the hyperfine interaction strength varies drastically (0–126 MHz [78, 79]) depending on their position in the lattice.

NV^0

Figure 2.6c is an energy structure of NV^0 charge state [62, 64, 86]. The 5 electrons configure doublet levels ($S = 1/2$) at ground (^2E) and excited states ($^2A_2$). On the contrast to NV^-, magnetic resonance associated with these states of NV^0 are not detectable. It is believed that the absence of a NV^0 ground state magnetic resonance to be due to the presence of dynamic Jahn-Teller effect [62]. The electron spin resonance (ESR) studies on the exited state reveals that quartet state ($^4A_2$) can be optically populated via decay-

Table 2.5.: Experimental value of parameters in the ground-state Hamiltonian of negatively charged state. Axial, transverse hyperfine interaction and quadrupole splitting are for ^{14}N. Note that ^{15}N has no quadrupole moment.

coefficient	description	value	ref.
D_{gs}	axial ZFS parameter	2.87 GHz	[75]
E	transverse ZFS parameter	kHz – MHz	[68, 80]
g_s	g-factor of electron spin	2.003	[81]
μ_B	Bohr magneton	927.4×10^{-26} J T^{-1}	[82]
$A_\parallel$	axial hyperfine constant	−2.16 MHz	[83, 84]
$A_\perp$	transverse hyperfine constant	−2.7 MHz	[81]
P	nuclear electric quadrupole parameter	−4.95 MHz	[83, 84]
g_I	g-factor of nuclear spin	0.403	[81]
μ_N	nuclear magneton	5.1×10^{-27} J T^{-1}	[85]

ing from $^2A_2$ level [62, 87]. However, no optically detected magnetic resonance (ODMR) or optical readout of the quartet spin state have been demonstrated to date. Further evidence for mechanism of intersystem crossing between $^2A_2$ and $^4A_2$ levels are required.

The ZPL of this state is assigned to 575 nm [61, 64]. The ground state Hamiltonian of NV^0 is shown in references [28, 62, 64, 88]. The hyperfine interaction among NV^0 and surrounding nucleus is different from that among NV^- [28]. Thus nuclear rotation operations for NV^- is failed by charge state interconversion.

On the other hand, difference of hyperfine interaction is used to decouple the interaction among electron and nuclear spins. As for nuclear coupled with electron spin of NV, hyperfine interaction caused decoherence in nuclear spin state. This decoherence is suppressed via fast fluctuation (grater than hyperfine interaction) of charge state, corresponds to the fluctuation of spin states between $S = 1/2$ and $S = 1$. This process is analogous to motional averaging in nuclear magnetic resonance (NMR) [23, 89–91].

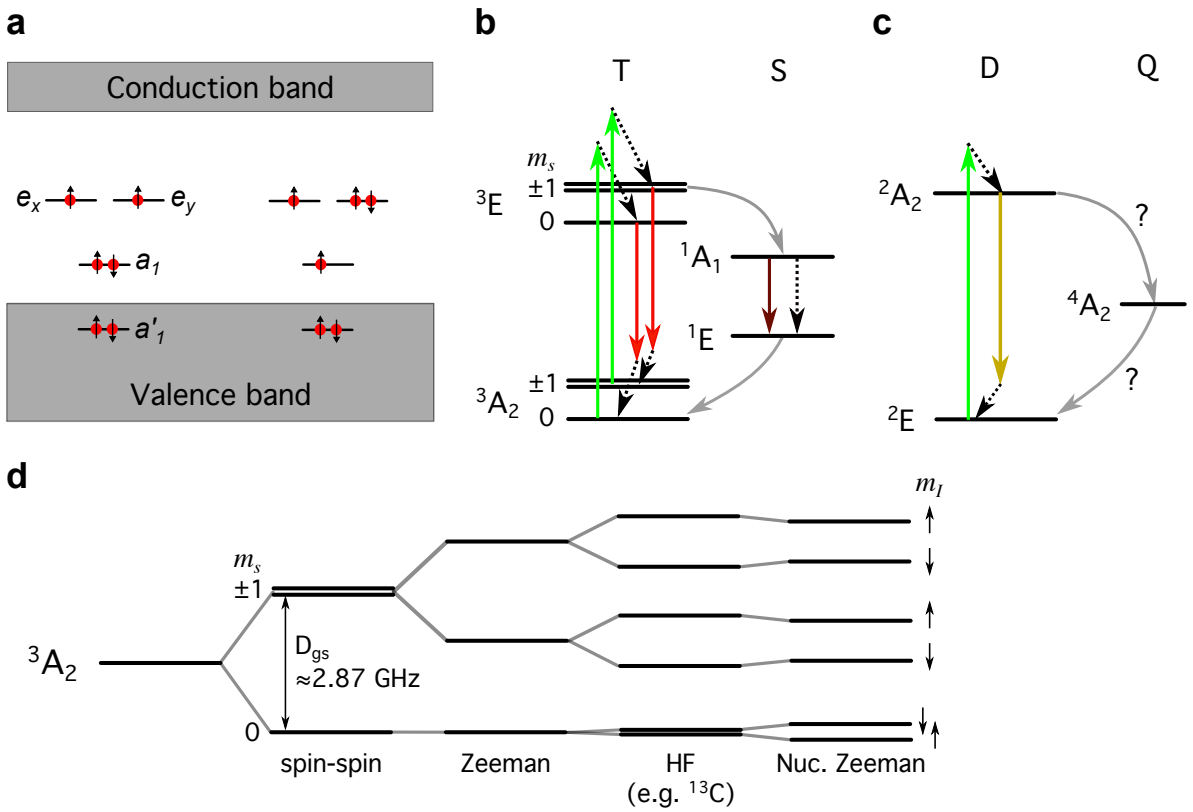

Figure 2.6.: Electronic structure of the NV. a, Electron configuration of NV^- within the band gap of diamond. Left and right are electronic ground and first excited state configuration respectively. **b,** Level structure of NV^-. Non-resonate optical excitation into the vibrational mode (phonon sideband) is illustrated by green arrow. Excited electron decays non-radiatively to lower vibrational mode into each states (dashed arrow). Gray arrow is showing the non-radiative transition assisted by intersystem crossing (ISC). At room temperature, fluorescence (red arrows) also ends up in the corresponding vibration mode of phonon. The transition within metastable states ($^1A_1$ and ^1E) has fluorescence at infrared region which is beyond the detection rage of silicon avalanche photodiode (ADP). **c,** Level structure of NV^0. No ODMR has been demonstrated to date in this charge state. An optically dependent spin polarization of $^4A_2$ is reported by ESR measurement but optically readout of the quartet spin state are still missing. It is thought that spin-orbit mixing between $^2A_2$ and $^4A_2$ levels are very small or a very different process to that which occurs in NV^-. **d,** Ground state splitting of NV^- coupled with a ^{13}C nuclear. Electron spin states split under zero magnetic field with spin-spin (magnetic dipole), Zeeman, and hyperfine interaction (HF). A small nuclear Zeeman splitting also exists.

3. Experiments

This chapter focused on the concept of several experiments on the NV. First explains the common measurement setup for fluorescence detection of the NV in diamond. Second explains single-shot charge-state measurement (SCM) and fluorescence averaging measurement (FAM) to evaluate charge state dynamics of the NV. Finally, spin resonance measurements are briefly introduced.

3.1. Basic experimental setup

The task of experiments is especially to seek single NVs in bulk diamond and perform charge state measurement on a single NV. The core-technology of the requirements has been developed in the fluorescence detection on single dye molecules [92]. The confocal microscopic system has been used to address and manipulation of such molecules. In this study, similar techniques are used to detect fluorescence from single NVs.

All of measurements in this study has been conducted by a home-build confocal microscope. It consists of a microwave radiation system for spin resonance and voltage sources for charge state manipulations in the *p-i-n* diode. All measurements are conducted under ambient condition. The key elements of a confocal microscope are shown in figure 3.1a which contains excitation lasers, objective, a pinhole, two-avalanche photodiodes (APDs), and optional elements. Configuration of an objective and a pinhole are essential because they determine the optical resolution and signal intensity of the microscope. A high-numerical aperture (NA) apochromatic objective is suitable for effective experiments. The NA is defined as $\mathrm{NA} = n \sin\theta$, where n is refractive index of a medium (here immersion oil) and θ is the half the open-angle of the light cone that enter or exit the lens. NA determines a spot size of an image and substantially influences the minimum optical slice thickness. A pinhole prevents detection of out-of-focus light and its diameter decides a depth discrimination. In this study, a commercial-available objective (Olympus UPLSAPO 100XO, magnification: 100x) which has NA of 1.4 with immersion oil ($n_{\mathrm{oil}} = 1.518$) had been used. The diameter of the pinhole is $\phi = 30\,\mu\mathrm{m}$. The lateral and axial resolution can be calculated on the basis of the following formulae [93, 94]:

$$\text{Lateral resolution} = \frac{0.51\lambda_{\text{exc}}}{\text{NA}}, \tag{3.1}$$

$$\text{Axial resolution} = \frac{0.88\lambda_{\text{exc}}}{n_{\text{oil}} - \sqrt{n_{\text{oil}}^2 - \text{NA}^2}}, \tag{3.2}$$

where λ_{exc} is excitation wavelength of the laser and n_{oil} is a refractive index of the immersion medium. The ideal lateral and axial resolution would be 193 nm and 701 nm with ideal pinhole size, however actual resolutions are limited by several factors especially the incident beam size to the objective. The objective is mounted on a 3-axes piezoelectric-nanopositioner which makes it enable to take tomographic fluorescence mappings of a sample. acosto-optic modulators (AOMs) chop continuous wave (cw) laser to make pulse shaped laser. Optical elements consist of a variable neutral density (ND) filters, single mode optical fibers, polarizing beam splitter (PBS), and wave plates. The ND filter modulate incident laser power. A single mode optical fiber makes clear circular-polarized Gaussian-shaped beam. A PBS make a liner polarizing right and the direction of polarization is rotated by a half-wave plate (HWP). A PBS also conducts reflection right from the surface of the sample to a charge coupled device (CCD) camera in order to observe the surface of a sample. Dichroic filters reflect excitation beam, however they pass fluorescence right which is longer than excitation wavelength. A flipper is set after pinhole which conducts fluorescence to a spectrometer and a cryogenic CCD camera. The CCD camera is connected to a computer and it displays spectra of fluorescence. The 645 or 675 nm-longpass filter (LPF) blocks fluorescence of neutral charge state of nitrogen-vacancy center (NV^0) and the remains are finally conducted to two APDs. Two APDs are connected to a computer with delay electric cables (approximately 80 ns delay) for coincident measurement of photons. Continuous-wave or pulsed microwave (mw) or radio frequency (rf) wave for spin resonance experiments are generated by oscillator and applied to samples with antenna made of a copper wire (cross-sectional diameter: 25 µm).

3.2. Basic measurement results

Figures 3.1b–d is a set of basic measurement results. A fluorescence mapping of single NVs is a most basic measurement. Figure 3.1b is a raster scan image of an intrinsic (undoped) diamond which contains single NVs. Green laser was used to take this image. Single NVs are spotted as bright circles in the mapping. This figure has 300×300 pixels size and accumulation time is 3 ms per pixel. Fluorescence from off-focused NVs are cut by a confocal microscope (pin hole), make it enable to distinguish a single NV.

To identify NV as a single photon emitter, the second-order autocorrelation function ($g^{(2)}(\tau)$) measurement had been performed. The $g^{(2)}(\tau)$ is expressed as follow:

$$g^{(2)}(\tau) = \frac{\langle I_{PL}(t) I_{PL}(t+\tau) \rangle}{\langle I_{PL}(t) \rangle^2}, \tag{3.3}$$

where I_{PL} (t) is photoluminescence intensity at time t and brackets indicate a time average. A characteristic dip ($g^{(2)}(\tau)(0) = 0$) appears in coincident measurements of photons by a pair of APDs. For a three-level system (e.g. , NV^-), $g^{(2)}(\tau)$ is written like as follows [95, 96]:

$$g^{(2)}(\tau) = 1 - (1+\alpha) \exp\left(-\frac{|\tau|}{\tau_1}\right) + \alpha \exp\left(-\frac{|\tau|}{\tau_2}\right). \tag{3.4}$$

This notation does not take into account background fluorescence. I modified equation (3.4) as follows to fit it into actual experiments:

$$g^{(2)}(\tau) = 1 - \frac{I_{\text{sat}} + \alpha}{I_{\text{back}} + I_{\text{sat}}} \exp\left(-\frac{|\tau|}{\tau_1}\right) + \frac{\alpha}{I_{\text{back}} + I_{\text{sat}}} \exp\left(-\frac{|\tau|}{\tau_2}\right), \tag{3.5}$$

where I_{sat} and I_{back} are the number of photons at $t \to \infty$ and $t = 0$, respectively. Figure 3.1c is $g^{(2)}(\tau)$ on a NV with different excitation powers of green laser. At high power excitation, $g^{(2)}(\tau)$ show bunching behavior ($g^{(2)}(\tau) > 1$) due to existence of metastable state. This phenomenon can be used to distinguish charge state of NV, because NV^0 does not show bunching at any excitation power, because of few possibility of decaying to its $^4A_2$ state [64]. Solid carves in the figure are the fitting by equation (3.5).

Figure 3.1d is a laser power dependence of I_{PL} of a single NV in intrinsic diamond under green laser excitation. I_{PL} can be fitted with a function $I_{PL} = I_{PL\text{sat}} \times P/(P + P_{\text{sat}})$ [97], here $I_{PL\text{sat}}$ is a saturation PL intensity, P is a excitation laser power, and P_{sat} is a P where I_{PL} has a half value of $I_{PL\text{sat}}$. By the fitting of the result, $P_{\text{sat}} = 471\,\mu\text{W}$ and $I_{PL\text{sat}} = 294\,\text{kcps}$ is obtained. At that saturation of fluorescence, pumping in NV is saturated and it is known that NV emits photons per every 11.6 ns at saturation [98, 99]. Therefore, the total photon collection efficiency (η_m) of the experimental setup can be derived to $\eta_m = 294\,\text{kcps}/11.6^{-1}\,\text{ns}^{-1} \approx 0.003$.

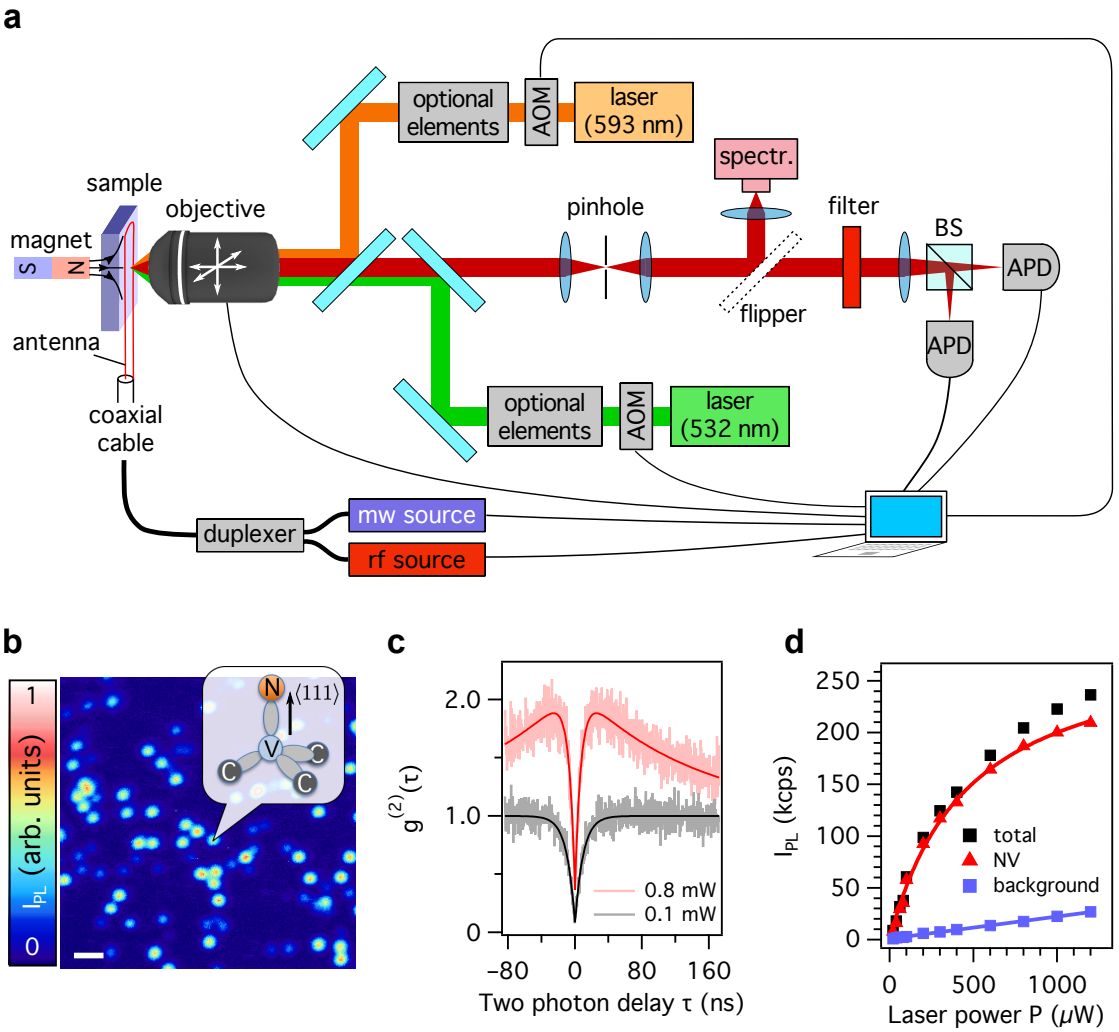

Figure 3.1.: Experimental setup and basic measurements. **a,** The setup consists of a confocal microscope with two lasers and a spin resonance system. Optional elements consist of a variable neutral density (ND) filter, a single mode optical fiber, and polarizers. Longpass filter (LPF) mainly passes photons from NV^- then improve contrast of fluorescence during charge state measurements. **b,** Raster scan image of single NVs in intrinsic (undoped) diamond. An image was taken by green laser. Single NVs are resolved as high fluorescent spots. The resolution of this image is $300 \times 300\,\mathrm{pixels}$ and accumulation time is $3\,\mathrm{ms}$ per pixel. Scale bar, $1\,\mu\mathrm{m}$. An inset illustrate a single NV structure and that symmetry axis of NV coincides with the $\langle 111 \rangle$ direction of the diamond lattice. **c,** The second order autocorrelation measurement of photons from a single NV with different excitation power of green laser. Bunching behavior is clearly seen in higher pumping power. **d,** Excitation laser power (P) dependence of PL intensity (I_{PL}) on a single NV. Laser color is green. Triangle points are bare fluorescence of NV which is obtained to subtract background signals from total fluorescence.

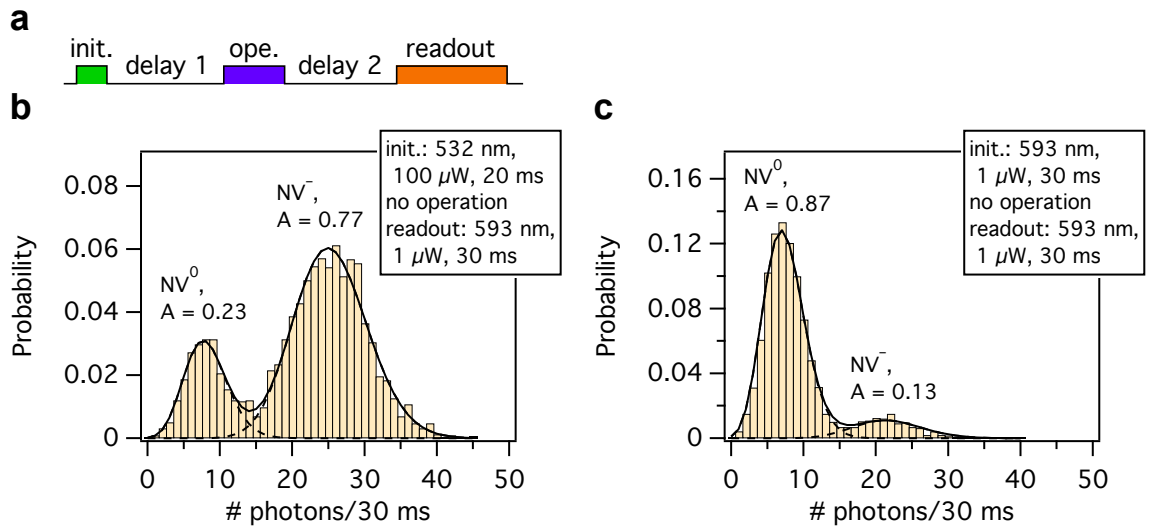

Figure 3.2.: Concept of the single-shot charge-state measurement. **a,** Typical sequence of the measurement contains an initialization (init.), operations to the NV (ope.), and a readout. Delay 1 (between init. and ope.) and delay 2 (between ope. and readout) are also parameters. Usually sequences are repeated more than 1000 times. **b,** Measurement results on an NV in intrinsic diamond with the initialization by green (532 nm) illumination. The population of the charge state is calculated by the area of distributions (displayed as "A" in the graph). **c,** The NV^- population drastically decreased when the charge state is initialized by the orange (593 nm) laser. The orange laser brings NV^- to NV^0 because it is hardly excite NV^0 which necessary to turn back charge state into NV^- in the charge conversion process. All results are normalized their integral to unity.

3.3. Charge state measurements

In this study charge-state population and transition rates are evaluated by means of single-shot charge-state measurement (SCM) and fluorescence averaging measurement (FAM). In both measurements charge state is detected as difference of photoluminescence/fluorescence intensity (I_{PL}). By the filtering fluorescence from single NV at longer than 645 or 675 nm, NV^- shows higher I_{PL} than that of NV^0. Here the difference in filtering wavelength have no special meanings.

The single-shot charge-state measurement

The SCM have been performed to obtain population probability of charge-state (p). SCM measurements rely on that the charge state transition is drastically suppressed under weak orange (593 nm) excitation and it enables us to count photon number non-destructively. Figure 3.2a is a measurement sequence of this measurement. Generally the SCM consists of an initialization, an operation, and a readout of photon counts from an NV. Usually the initialization is irradiation of laser with arbitrary wavelength

and power. It sets the charge states into several population probabilities. After the initialization, the operation (i.e. optical illumination, voltage applying, etc.) to the NV may change the charge state. The readout is irradiations of weak orange laser light ($P \leq 1\,\mu W$) to nondestructively excite the NV and readout a number of emitted photons. The sequence is repeated 1000–2000 times usually. The charge state is detected as the difference of a number of photons. The point is that the readout time length should be shorter than the average life times of every charge state during the readout excitation. From figure 2.4b, the average life time of NV^0 and NV^- are 3.27 and 0.644 s during 1 µW of orange laser excitation, respectively. Therefore, the readout time length should be shorter than 0.644 s at least to ensure nondestructive measurement. These lifetime of intrinsic NV are almost same in the whole of measurement shown in this thesis. The photon statistic results with several initializations are shown in figures 3.2b,c. These are histograms of a number of photons after initialization by green and orange laser and readouts with 30 ms laser irradiations (orange 1 µW). Peaks in the results are fitted by Poisson distribution function. In the measurement without operations between initialization and readout, results reflect charge state populations during initializations. Two peaks in the each histograms are photon distributions from NV^0 and NV^-, respectively, which correspond to I_{PL} of each charge states in figure 2.4b. The populations are determined from the area of each peaks.

The fluorescence averaging measurement

This measurement provides us time resolved dynamics of charge state. Averaging of I_{PL} reflects time evolution of charge state following equation (2.10). Figure 3.3a shows a typical pulse sequence of this measurement. Averaging of I_{PL} is performed during readout with comparably high power of laser irradiations. Figure 3.3b is a readout with green laser ($P = 70\,\mu W$) after initialization by the same power of orange laser. Increase of I_{PL} correspond to increase of p_-. The curve is fitted by an exponential function. The inverse of time constant of transition equals to the total rate. Under green laser illumination, transition rate is determined as $\gamma = 1/\gamma = 0.130\,\mu s^{-1}$. Figure 3.3c is a readout with orange laser ($P = 70\,\mu W$) after initialization by green laser. The decrease of I_{PL} means decrease of p_- during orange laser illumination. Transition is 13 times slower than that under green laser illumination.

Figure 3.4 is a total (fluor. increase) rate under various green laser excitation power. This rate shows quadratic dependence to laser power. Usually the measurement sequence are repeated 10^6–10^7 times to obtain a result.

3.4. Spin resonance measurements

In this study, few number of spin measurements were performed; however it is important to explain spin measurements more or less to indicate how NV works as qubit system.

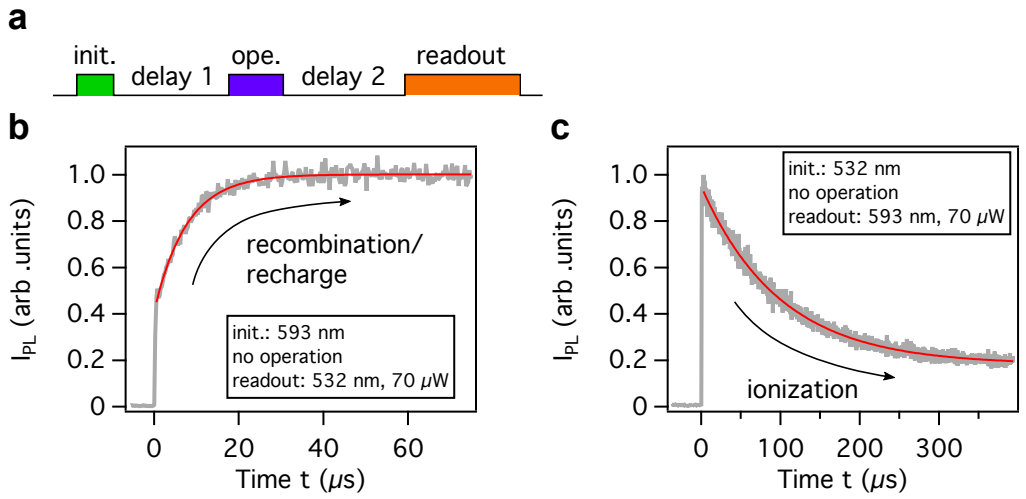

Figure 3.3.: Concept of the fluorescence averaging measurement. **a,** Typical sequence of the measurement. Averaging intensity of photoluminescence (I_{PL}) reflects the time evolution of the charge state during readout. **b,** A readout with green laser after initialization by orange laser. Exponential increase of I_{PL} corresponds to recombination (or recharge) of charge-state. The curve is fitted by a function $y = y_0 + C\exp(-\gamma t)$, where $\gamma = \gamma_{-0} + \gamma_{0-}$ is total rate. Time constant of transition ($\tau = 1/\gamma$) is 7.68 µs in the measurement. **c,** I_{PL} exponentially decrease during orange laser excitation after initialized by green laser. This corresponds to that ionization of charge-state. A τ is 99.3 µs. Total rate during orange laser illumination is 13 times smaller than that during green laser illumination. Arrows indicate transition direction of charge state population.

Most fundamental spin measurement is optically detected magnetic resonance (ODMR). magnetic resonance (MR) at ground state is detected via optical fluorescence. Figure 3.5a is pulse sequence and result of a cw-ODMR. Static magnetic filed splits degeneration of electron spin at $m_s = \pm 1$ (single asterisk in the figure). The hyperfine interaction also splits the electron state (double asterisk). In this case ^{13}C in the third shell coupled to a single NV [100]. Laser initialize electron spin into its $m_s = 0$ state and consequently read spin state. During optical pumping, cw-mw with varying frequency sweep NV. If electron resonant to mw, it flips to $m_s = -1$ or 1 state then NV goes to singlet metastable state during optical cycle (see figure 2.6b). This path is non-fluorescence. Thus decrease of I_{PL} is observed at resonance, corresponds to dips in figure 3.5a. Figure 3.5b indicates splitting of electron spin by external magnetic field and hyperfine interaction (e.g. ^{13}C).

Using the same concept as ODMR, coherent dynamics of spin by MR is observed as Rabi oscillation [101]. Figure 3.5c is a pulse sequence of the measurement and electron Rabi oscillation in the ground state. This measurement frequency of mw is fixed to the resonance frequency of electron. Duration of pulse (τ) is modulated after spin initialization by laser. Spin state of electron is shown as and in the graph. The spin state is written as follows using Bloch spherical representation [102]:

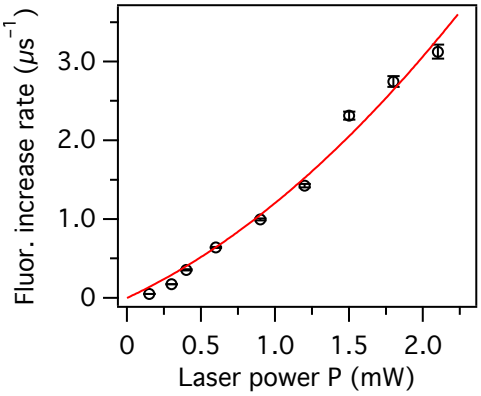

Figure 3.4.: Fluorescence increase rate during green laser excitation. Fluorescence (fluor.) increase rate is derived by a fitting with single exponential function $\exp(-\gamma t)$ to I_{PL}. A solid carve is a fitted by $f(P) = aP + bP^2$, where $a = 0.893\,\mu s^{-1}\,mW^{-1}$, $b = 0.319\,\mu s^{-1}\,mW^{-2}$.

$$|\Psi\rangle_e = \cos\left(\frac{\theta}{2}\right)|0\rangle_e + e^{i\phi}\sin\left(\frac{\theta}{2}\right)|-1\rangle_e\,, \tag{3.6}$$

where $|0\rangle_e$ and $|-1\rangle_e$ indicate a spin state $m_s = 0$ and $m_s = -1$ of ground state, respectively. This is a simplest 1 qubit system. The change in pulse duration corresponds to modulation of θ. Here $\theta = \pi$ makes state to $|\Psi\rangle = |-1\rangle_e$ (meanwhile azimuthal angle $\phi = 0$). The mw pulse duration makes such state is called "π pulse". At the long pulse duration, the development of the phase term $e^{i\phi}$ is appearing as decaying of inverse inhomogeneous broadening; decay constant of FID (T_2^*) and is shown as the decaying of the envelop of Rabi oscillation (blue dotted line in figure 3.5c[1]).

As well as electron Rabi measurement, nuclear spin nutation can be seen. Figure 3.5d is a pulse sequence used in this measurement and a result. First pulses (init.) set electron state in $|0\rangle_e$. After initialization of electron spin, the system is found in either $|0\rangle_e|\uparrow\rangle_n = |0\uparrow\rangle_{en}$ or $|0\rangle_e|\downarrow\rangle_n = |0\downarrow\rangle_{en}$. Next mw is set to the one of the resonance frequency out of four possible transition in figure 3.5b. Here transition between $|0\downarrow\rangle_{en}$ and $|-1\downarrow\rangle_{en}$ is taken. Therefore the final mw pulse only affect to the state $|-1\downarrow\rangle_{en}$. The rf wave rotate the nuclear spin from $|\downarrow\rangle_n$ into $|\uparrow\rangle_n$ in $|-1\rangle_e$ state which results in nuclear Rabi oscillation. Thus, this is a controlled rotation and therefore a CROT gate [78].

[1]Strictly speaking, spin-locking must be taken into account [103]

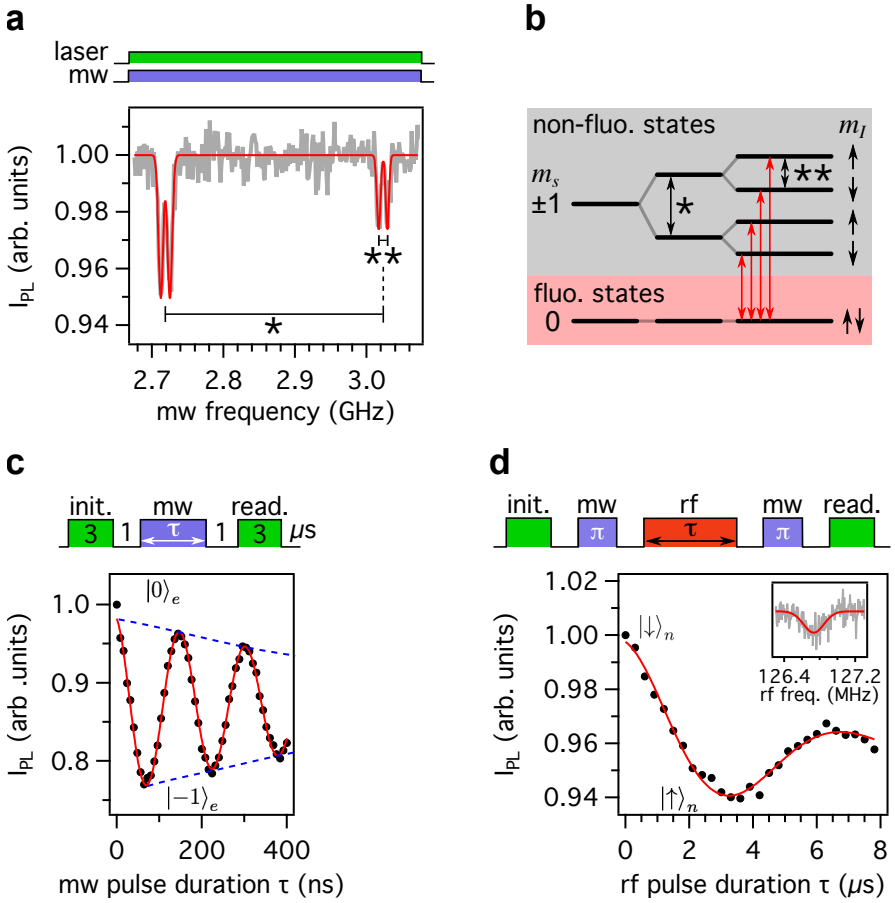

Figure 3.5.: Measurements of spin resonance on a single NV. **a,** Pulse sequence of a continuous-wave optically detected magnetic resonance (cwODMR) and a spectrum of the ground state spin of NV^- coupled with ^{13}C in the third shell. Static magnetic field is applied parallel to the NV axis. Magnetic resonance induced by microwave (mw) and four dips in I_{PL} correspond to the transitions within electron state splitted by zero-field, Zeeman (single asterisk), and hyperfine splitting (double asterisk). The difference of signal intensity between $m_s = +1 \leftrightarrow 0$ and $m_s = -1 \leftrightarrow 0$ comes from impedance mismatching between a coaxial cable and a mw antenna (copper wire). **b,** Transition diagram of the ground state of NV^- for panel **a**. Four possible transitions are indicated with red arrows. $m_s = 0$ state is fluorescent (red shaded) and $m_s = \pm 1$ states are non-fluorescent states (gray shaded). **c,** Electron Rabi oscillation in the ground state of a single NV. Coherent oscillation between two electron spin states is induced by varying mw pulse duration and is detected as a periodical vibration of PL intensity. **d,** Nuclear Rabi oscillation of ^{13}C in the first shell. Radio frequency wave (rf) sweeps NV to rotate proximal nuclear spin, after spin state of electron is set to non-fluorescence state ($m_s = \pm 1$). Inset is an electron nuclear double resonance (ENDOR) signal.

4. Charge state control on a diode

This chapter focuses on the electrical control of charge state by using a p-i-n diamond diode which is suitable for current injection into single NVs to control their number of electrons. Current injection through diamond requires dopants to generate electrons or hole carries. However, donor doping leads to defects that have electroluminescence in the visible spectral range. Thus an extremely high-quality undoped region (i-layer) is needed to investigate single NVs individually. Single NVs are generated into i-layer region by ion-implantation technique, and major hole carriers are injected into the NVs whose depth are around 300 nm from the surface of i-layer. Hole carrier deterministically ionize single NVs and switching between NV^- and NV^0 by mean of combination of optical and electrical methods. As a result of single-shot measurement and fluorescence averaging measurement, one-directional electrical ionization rate is derived independently from bi-directional total rate. These insights enable us to quantitatively compare optical and electrical method as for control efficiency. The relation of stored charge in the i-layer and charge state of a single NV is also discussed.

4.1. Preparation of the sample

Phosphorus-doped n-type and i-layer were independently grown by microwave-plasma-enhanced chemical vapor deposition (CVD) technique using a mixture of methane (CH_4) and hydrogen (H_2) gas on high-temperature high-pressure (HTHP) synthetic IIb (001) p-type single-crystalline diamond. Joint researchers in the National Institute of Advanced Industrial Science and Technology (AIST) had performed synthesis. The condition of the growth is summarized in table 4.1. For the i-layer, oxygen (O_2) was added into the feed gas to reduce the contamination from boron and other impurity atoms. For the n-type layer, phosphine (PH_3) diluted with H_2 was used for phosphorus doping. The thickness and the contents of each layers were listed up in table 4.2. The electron and hole Hall mobility of n and p-type layers are around 150 and 10 $\mathrm{cm^2\,V^{-1}\,s^{-1}}$, respectively. After growth, round mesa structures of n-type layer with diameters of 220 µm were fabricated by conventional photolithography and inductively coupled plasma (ICP) etching.

Nitrogen was subsequently implanted to the i-layer by ion implant with a density of 1×10^9 atoms $\mathrm{cm^{-2}}$ after mesa structure synthesis. The kinetic energy of ion implantation was 180 keV which resulted NV center at the depth of 300 nm. Subsequent annealing at 800 °C for 60 min produced NV center with concentration of below 0.1 ppb. To remove

Table 4.1.: CVD growth condition of the *i* and *n*-layer.

	i-layer	*n*-layer
input power (W)	4200	750
CH_4/H_2 (%)	4	0.4
gas pressure (Torr)	170	250
substrate temperature (°C)	850	900
O_2/CH_4 (%)	2.5	–
PH_3/CH_4 (%)	–	5

Table 4.2.: Major contents and thickness of the *p-i-n* diamond.

layer	contents	thickness (µm)
p	$[B] = 10^{19}\,cm^{-3}$	500
i	$<10^{14}\,cm^{-3}$ (1 ppm)	10
n	$[P] = 10^{18}\,cm^{-3}$	0.5

residual surface contamination and terminate surface with oxygen, The sample was kept in a mixture of sulfuric acid (H_2SO_4) and nitric acid (HNO_3) at 200 °C for 60 min.

Titanium(30 nm)/platinum(100 nm)/gold(200 nm) electrodes with diameters of 200 µm and square area of 1.5 mm × 1.5 mm were formed on the *n*-type layer and the substrate, respectively. Electrodes on *n*-type layers were connected by gold wire, and the electrodes on the *p*-type layer was attached to copper plate which makes common ground. Surface hydrogenation was carried out by irradiation with H_2 radicals for 10 min at 4 kPa using a hot filament system. The flow of high-purity H_2 (99.999 999 9 %) gas was set to 400 sccm. The sample temperature was maintained below 550 °C during hydrogenation. Oxidation was carried out by ICP etching in the presence of oxygen gas, which was also used to remove residual photoresist material. The sample was annealed at 420 °C for 30 min in an argon environment. The sample has 49 electrodes in total and whole experiments are carried out on the one of them.

The schematic out look of the sample is illustrated in figure 4.1a. A bottom electrode is attached to a copper plate to avoid over heating of the sample. Top and bottom electrodes are connected to a current pulse generator with Au wires. The space between an objective and the sample surface is filled by immersion oil during optical measurement and current injection. Figure 4.1b is a photoluminescence (PL) scan image of the surface of the *i*-layer. Red dots in the layer is a single NVs. This sample has slightly high background fluorescence intensity than other sample. However after surface cleaning processes, the signal-to-background ratio was sufficiently high to indicate whether second order autocorrelation function $g^{(2)}(0)$ is smaller than 0.5 (see figure D.2).

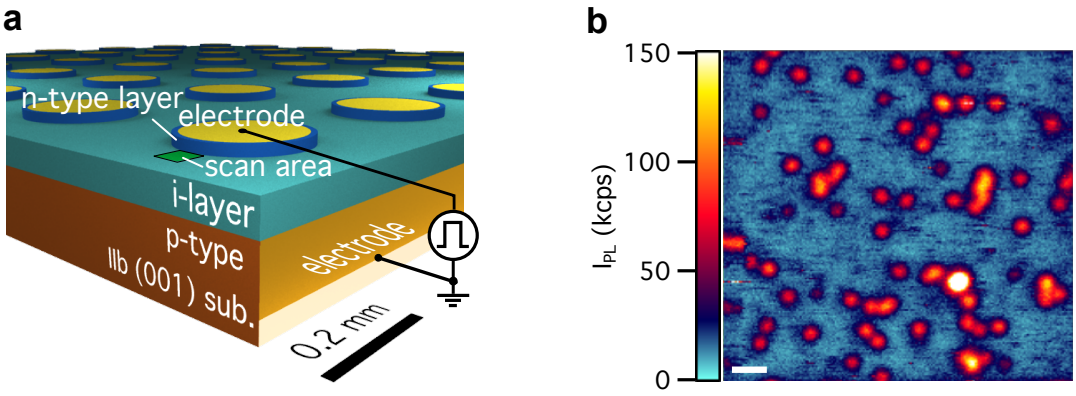

Figure 4.1.: Schematic illustration and a scan image of the *p-i-n* diode. a, The *p-i-n* sample has mesa structures of *n*-type layers on an *i*-layer. Diameter of mesas is 220 µm. Electrodes (each diameter is 200 µm) are fabricated on each mesa and on the *p*-type layer. They are connected to a current source with an Au wire. A green square is a typical scan area (e.g. $50 \times 50\,\mu m^2$) with a confocal microscope. A scale bar is appropriate only to the lateral direction. **b,** A PL scan image of the *i*-layer with the area of $10 \times 10\,\mu m^2$. Ion implanted single NVs (red dots) are found in the layer. Experiments had been performed on one of the NV which has distance of ∼1 µm from the mesa. Scale bar, 1 µm.

4.2. Fluorescence dynamics

Current injection into the sample modulates the charge state of NV from NV^- to NV^0 in the *i*-layer. It is recorded as differences of spectra shapes and photoluminescence/fluorescence intensity (I_{PL}). Figures 4.2a,b are PL spectra of a single NV and difference of the spectra. PL spectra were taken under 300 µW of green laser illumination. The NV shows a characteristic spectrum shape populated toward NV^- under no current injection. The zero-phonon line (ZPL) of NV^- is marked with single asterisk in the figure. The distance from the NV to *n*-type layer is ∼1 µm. Under continuous wave (cw) current injection ($I_F = 70\,\mu A$), the NV shows spectrum populated toward NV^0 (a blue carve). The characteristic ZPL of NV^0 is appears in the spectrum (double asterisk in the figure). The profiles of phonon side band under off- and on-states of diode are similar to NV^- and NV^0 appears in the previous report [24]. Resulting phonon sideband are broad and both spectra overlapped to ZPLs of each charge state. Thus NV^0-populated spectrum under on-state may contain ZPL of NV^- and vise versa. This obstruct evaluation of charge state population from PL spectra. The difference of spectra shows high contrast of I_{PL} at wavelength longer than 650 nm (see figure 4.2b). Selective measurement of I_{PL} longer than 650 nm enable us to detect charge state from difference in PL intensity (ΔI_{PL}). An optical filter which selectively pass the fluorescence longer than 675 nm[1] is put in the

[1]During measurement, there are no stocks of proper (around 650 nm) longpass filter in Lab. Thus this wavelength of 675 nm is used in the study on the *p-i-n* diode.

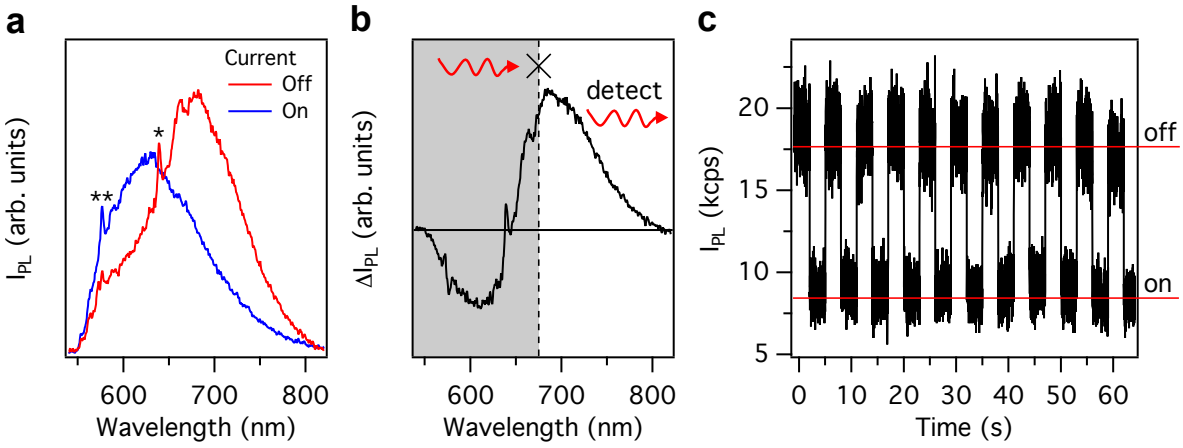

Figure 4.2.: Fluorescence dynamics under current injection. **a,** PL spectra of NV with and without current injection. The phonon side band peak shifts toward the shorter wavelength during current injection. Sharp peak at 637 nm (single asterisk) and 575 nm (double asterisk) are zero-phonon line of NV^- and NV^0, respectively. Background fluorescence is subtracted from spectra. **b,** Difference of the spectra at on and off states. Fluorescence of a gray shaded area is cut by a long-pass filter (675 nm) which is put in the front of two photon detectors. **c,** Time trace of PL intensity with periodic current pulse train. State of current is shown as "on" and "off" at the right axis.

front of two avalanche photodiodes (APDs).

Figure 4.2c is a real-time trace of I_{PL} under injection of periodic current pulse train (width: 3 s, I_F: 0.2 mA) and cw-green laser excitation (532 nm, 600 µW). Oscillating of I_{PL} according to current pulse are clearly observed thanks to the optical filtering. Note the amplitude of switching contrast of charge-state population can be modulated with arbitrary shape of current pulse. For example, if sin-wave current is injected to the *p-i-n* sample, charge state follow this current and show sin-wave like I_{PL}. Result is shown in figure D.3 in appendix D.

Fluorescence dynamics of I_{PL} reflect charge-state transitions between two equilibrium states at on- and off-states of the *p-i-n* diode. Here I_{PL} is proportional to the charge state thus population probability of charge-state (p) in each equilibrium state can be written as follows, determined by equation (2.11), with four transition rates of charge states transients:

$$I_{PL} \propto \begin{pmatrix} p_-^{\mathrm{eq}} \\ p_0^{\mathrm{eq}} \end{pmatrix} = \frac{1}{\gamma_{-0}+\gamma_{0-}} \begin{pmatrix} \gamma_{0-} \\ \gamma_{-0} \end{pmatrix} = \frac{1}{\gamma_{-0}^{\mathrm{ele}}+\gamma_{-0}^{\mathrm{opt}}+\gamma_{0-}^{\mathrm{ele}}+\gamma_{0-}^{\mathrm{opt}}} \begin{pmatrix} \gamma_{0-}^{\mathrm{ele}}+\gamma_{0-}^{\mathrm{opt}} \\ \gamma_{-0}^{\mathrm{ele}}+\gamma_{-0}^{\mathrm{opt}} \end{pmatrix}, \tag{4.1}$$

where notations "opt" and "ele" represent "optically" and "electrically" induced rate, respectively. The ratio between these four transition rates determine the charge state population during operations combined with optical illumination.

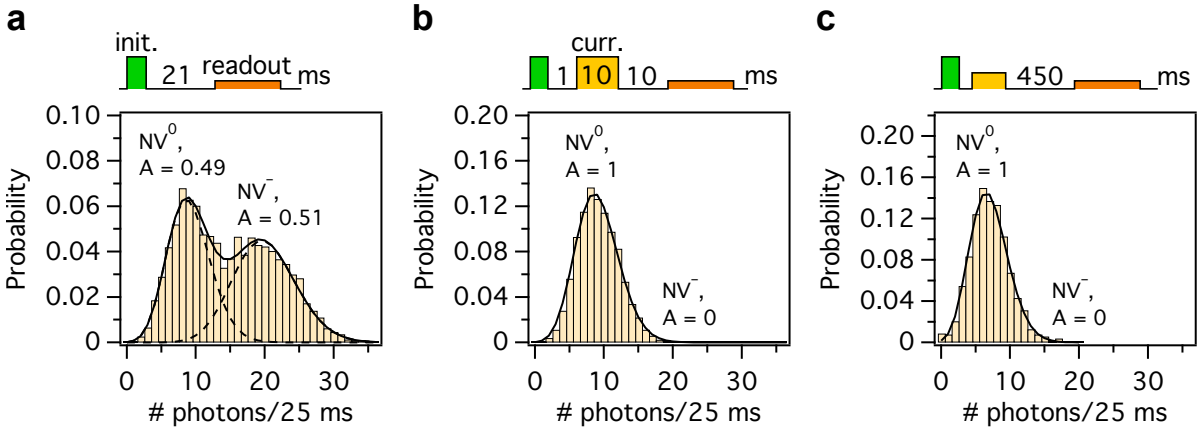

Figure 4.3.: Single-shot charge-state measurements under current injection. **a,** Without current injection, NV shows two charge states. Their population probabilities are determined by area calculation on Poisson distribution in the histogram. **b,** Charge state completely turns into NV^0 after current injection ($I_F = 0.1\,\mathrm{mA}$). **c,** Ionized charge state is detected after long time delay ($0.45\,\mathrm{s}$).

4.3. Single-shot charge-state measurement

The aim of this study is to obtain the electrical induced transition rates, $\gamma_{-0}^{\mathrm{ele}}$ and $\gamma_{0-}^{\mathrm{ele}}$ and population probability after current injection. The single-shot charge-state measurement (SCM) can derive not only population of charge state but also ratio of these two rates because during the measurement, optically induced rates ($\gamma_{-0}^{\mathrm{opt}}$ and $\gamma_{0-}^{\mathrm{opt}}$) are zero. Figures 4.3a–c are results of the SCM carried out on the initialization by green laser excitation. Figure 4.3a is a measurement without current injection. The charge state populates into both NV^- and NV^0 with amplitude of $p_0^{\mathrm{eq}} : p_-^{\mathrm{eq}} = 0.49 : 0.51$ derived from area of each peak. Here p_0^{eq} (p_-^{eq}) is slightly larger (smaller) than that of an intrinsic diamond (cf. $p_0^{\mathrm{eq}} : p_-^{\mathrm{eq}} = 0.27 : 0.73$ is observed in an intrinsic diamond, at the same experimental setup). This might comes from that the Fermi level of the i-layer is modulated to downward then reaches to the NV(0/−) level (see figure 2.2).

Evaluation of charge state under operation of the p-i-n diode is investigated to insert current injection between initialization and readout of charge state. Figure 4.3b is a measurement with single current pulse (amplitude $0.1\,\mathrm{mA}$, width $10\,\mu\mathrm{s}$). As a result, current injection completely ionize charge state, $p_0^{\mathrm{eq}} : p_-^{\mathrm{eq}} = 1 : 0$. This indicate apparently current injection is a deterministic control of charge state.

After current injection, 450-ms of delay time is set after current then readout is performed. Only NV^0 is detected in the measurement is displayed in figure 4.3c. This result supports that no rates are existing during a relatively long delay time. Note that the delay time is limited by the experimental setup (capacity of a buffer memory on the photon counting board), not by the properties of NV and diamond.

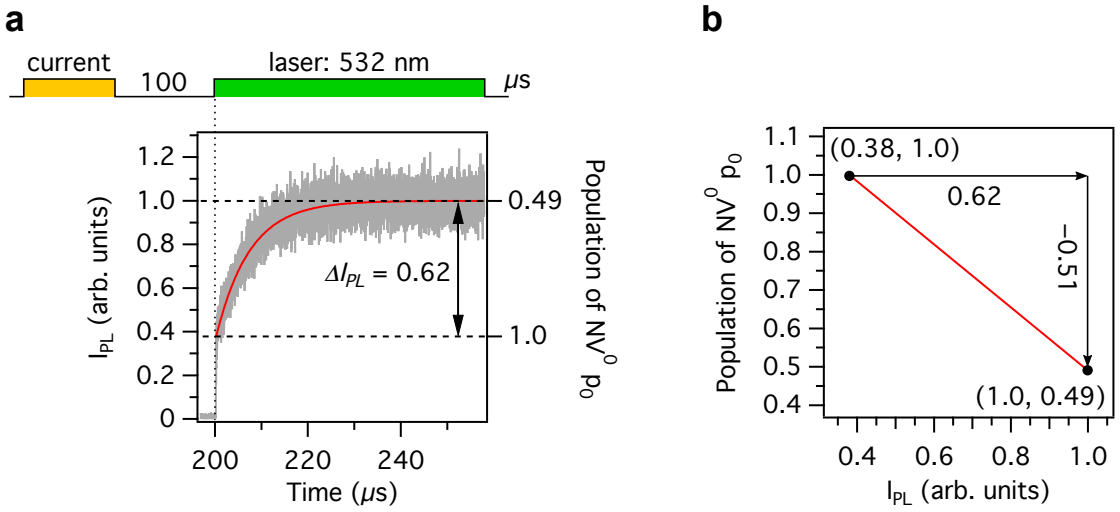

Figure 4.4.: Link fluorescence intensity and population probability of charge-state. a, Induce and detect charge state transition by green laser illumination after target NV is deterministically ionized by current. Increase of I_{PL} ($\Delta I_{PL} = 0.62$) corresponds to decrease of population probability of NV^0 (p_0) from 1.0 (see figure 4.3b,c) to 0.49 (see figure 4.3a). **b,** Population probability is displayed as a function of I_{PL}. It enables to link I_{PL} to p_0 with a simple linear equation.

The results of SCM determine $\gamma_{0-}^{\mathrm{ele}}$ as zero and from equation (4.1), electrically induced rate and population probability of charge-state at a state of the equilibrium (p_{eq}) are determined as follows:

$$\begin{pmatrix} p_-^{\mathrm{eq}} \\ p_0^{\mathrm{eq}} \end{pmatrix} = \begin{pmatrix} 0 \\ 1 \end{pmatrix} = \frac{1}{\gamma_{-0}^{\mathrm{ele}} + \gamma_{0-}^{\mathrm{ele}}} \begin{pmatrix} \gamma_{0-}^{\mathrm{ele}} \\ \gamma_{-0}^{\mathrm{ele}} \end{pmatrix}. \tag{4.2}$$

4.4. Fluorescence averaging measurements

Link fluorescence intensity and population probability of charge-state

The value of charge state transition rate, $\gamma_{0-}^{\mathrm{ele}} = 0$, is determined by SCM in the section 4.3. Next the fluorescence averaging measurement (FAM) had been carried out to obtain the value of $\gamma_{-0}^{\mathrm{ele}}$. At first, in order to obtain $\gamma_{-0}^{\mathrm{ele}}$ from FAM, the relation between I_{PL} and charge state population is required. At the beginning of consideration, the following two facts already known by SCM, are essentials.

1. Population probability of NV^0 is 0.49 under (after) initialization by green laser (see figure 4.3a).

2. Population probability of NV^0 is 1.00 under (after) initialization by current injection (see figures 4.3b,c)

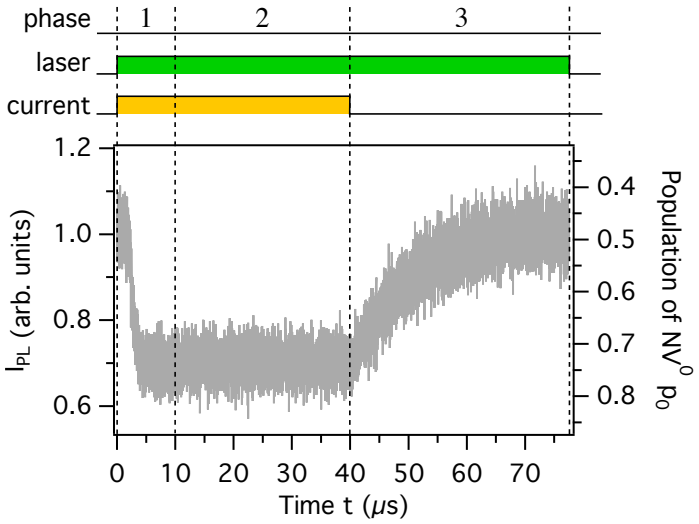

Figure 4.5.: Fluorescence averaging measurement on the *p-i-n* diode. Time resolved measurement of I_{PL} when 40 µs-width current pulse is applied. Transition is separated into three phases. At the beginning of Phase 1 ($0\,\mu s < t < \sim 10\,\mu s$), diode is turned on (on-state) and charge state transition is induced by current. At Phase 2 ($\sim 10\,\mu s < t \leq 40\,\mu s$), charge state population reaches to a state of the equilibrium. Phase 3 ($t > 40\,\mu s$) is recharge (recovery) process of charge state induced by optical illumination, after current is turned off (off-state).

If we can see time response of I_{PL} along with evolution of population betweem $p_0^{eq} = 1$ and $p_0^{eq} = 0.49$, relation between I_{PL} and p_0^{eq} is acquired. This is done by performing FAM after current injection.

Figure 4.4a is a measurement sequence and a result of the measurement. The first current pulse (width: 100 µs, $I_F = 0.4\,mA$) completely ionize NV. The second green laser is used to induce recombination of charge state and readout I_{PL}. Note that I_{PL} is normalized by value at a state of equilibrium,$t > 240\,\mu s$. As a result, the exponential increase of I_{PL} from 0.38 to 1.0 (ΔI_{PL}=0.62) is observed. It corresponds to the increase of p_0 triggered by the green laser. Here the population p_0 at the initial of the laser excitation ($t = 0$) and a state of the equilibrium ($t > 40\,\mu s$) are determined from the above enumerate. Measured value of p_0 is displayed in the right axis of figure 4.4a. Finally, the relation between I_{PL} and population of NV^0 is shown in figure 4.4b. The relation between arbitrary p_0 and I_{PL} can be obtained from following equation:

$$p_0\left(I_{PL}\right) = 1 - \frac{0.51}{0.62}\left(I_{PL} - 0.38\right), \ \left(0.38 \leq I_{PL} \leq 1\right). \tag{4.3}$$

Time resolved measurement of transition

Figure 4.5 is a transient of I_{PL} and p_0 during cw green laser excitation ($P = 0.2\,mW$) and current pulse ($I_F = 0.3\,mA$, width: 40 µs). The current pulse starts at $t = 0\,s$. The

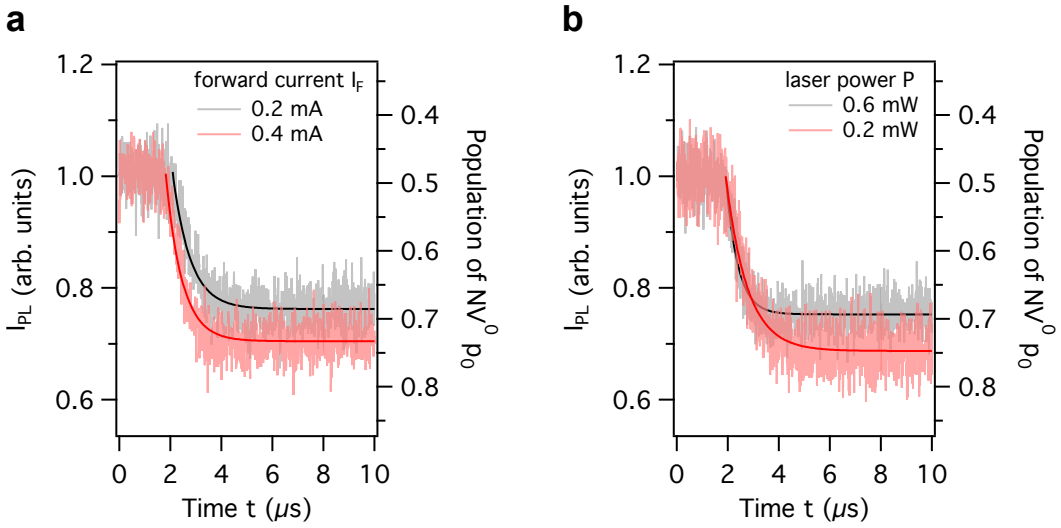

Figure 4.6.: Charge state transition at phase 1 (on-state). **a,** Transient at the phase 1 in figure 4.5 depends on forward current under fixed laser power. Laser power is 0.4 mW. Transition rates γ are 1.45 µs^{-1} ($I_F = 0.2$ mA) and 1.56 µs^{-1} ($I_F = 0.4$ mA). **b,** Transient depends on laser power. Forward current is fixed to 0.3 mA. Transition rates γ are 1.20 µs^{-1} ($P = 0.2$ mW) and 2.12 µs^{-1} ($P = 0.6$ mA).

p_0 starts to increase at $t = \sim$2 µs after of current is turned on. This delay may comes from the response time of the electrical circuit and other factors (see appendix D). The transition ends up within ∼5 µs (phase 1) and charge state is in a state of the equilibrium (phase 2). After current injection stopped at $t = 40$ µs, recombination of charge state starts and it ends at around $t = 70$ µs (phase 3). Further on, charge state dynamics are discussed in terms of these three phases. Note: in all of FAM in *p-i-n* diode, I_{PL} are normalized to unity by I_{PL} at delay time in phase 1 or a state of the equilibrium at phase 3.

Phase 1

Figures 4.6a,b are laser power and current dependence of I_{PL} transition. A population probability of NV^0 charge state (p_0) and transition rate depend on laser power and forward current because optical ($\gamma_{-0}^{\text{opt}} + \gamma_{0-}^{\text{opt}}$) and electrical ($\gamma_{-0}^{\text{ele}}$) induced rates are modulated by laser and current, respectively. From equation (2.10) and (4.3), I_{PL} is proportional to $\exp\left\{-\left(\gamma_{-0}^{\text{opt}} + \gamma_{0-}^{\text{opt}} + \gamma_{-0}^{\text{ele}}\right) t\right\}$. Thus total rate $\gamma = \gamma_{-0}^{\text{opt}} + \gamma_{0-}^{\text{opt}} + \gamma_{-0}^{\text{ele}}$ can be obtained by exponential fitting to time response of I_{PL} in the phase 1.

Owing to equation (4.1), one-directional ionization rates and p_0 are described as following relation:

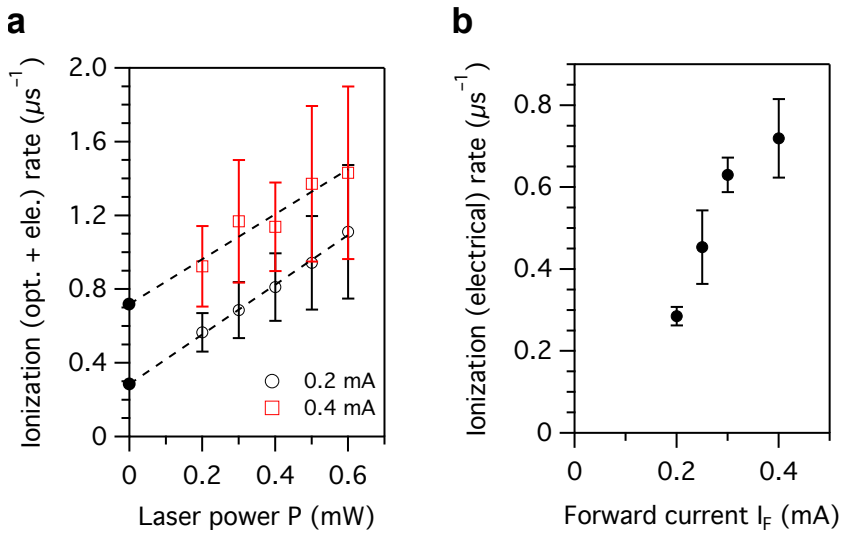

Figure 4.7.: Electrical induced ionization rate. **a,** Ionization rate ($\gamma_{-0} = \gamma_{-0}^{\text{opt}} + \gamma_{-0}^{\text{ele}}$) is obtained from the series of fluorescence averaging measurements. The rate γ_{-0} has a linear dependence to current and laser power. Electrical induced rate γ_{-0}^{ele} is obtained to interpolate data points to where the laser power equal to zero (displayed as dots on the left axis). **b,** Current dependence of electrical induced rate (γ_{-0}^{ele}) is derived from the panel **a** by interpolation.

$$\begin{aligned} \gamma_{-0} &= p_0^{\text{eq}} \left(\gamma_{-0} + \gamma_{0-}\right), \\ \gamma_{-0}^{\text{ele}} + \gamma_{-0}^{\text{opt}} &= p_0^{\text{eq}} \left(\gamma_{-0}^{\text{opt}} + \gamma_{0-}^{\text{opt}} + \gamma_{-0}^{\text{ele}}\right). \end{aligned} \tag{4.4}$$

Population at state of the equilibrium (p_0^{eq}) can be obtained by using equation (4.3), from FAM. Conclusionary, ionization rate $\gamma_{-0}^{\text{ele}} + \gamma_{-0}^{\text{opt}}$ is obtained.

Figure 4.7a is a laser power and current dependence of ionization rate $\gamma_{-0}^{\text{opt}} + \gamma_{-0}^{\text{ele}}$, calculated by using equation (4.4). Almost linear dependence of ionization rate to laser power and current is shown in the figure[2]. In order to derive γ_{-0}^{ele} from ionization rate $\gamma_{-0}^{\text{ele}} + \gamma_{-0}^{\text{opt}}$, interpolation of results has been performed. At the point where the laser power $P = 0$, the optical induced rate (γ_{-0}^{opt}) also becomes zero. These points are marked with black dots in the left axis of figure 4.7a. Figure 4.7b is a current dependence of the rate γ_{-0}^{ele} derived from the interpolation. Electrical induced rate linearly depends to current is shown. The maximum rate is 0.7 ± 0.1 µs at 0.4 mA current. The amplitude of current is limited to below 0.4 mA because the non-negligible electroluminescence (EL) from the NV or i-layer appears when current exceed 0.4 mA ($I_{EL} \simeq 1$ kcps).

Results of the electrical induced rate allow us to quantitative comparison of control efficiency between electrical and optical charge state manipulations. Here calculation

[2] Under this range of laser power ($0.2 < P\,(\text{mW}) < 0.6$), quadratic dependence of transition rate is shown in figure 3.4. Linear dependence in p-i-n diode indicate some different mechanics for charge state transition are involving but details is not available.

of energy costs in charge state controls are shown. First, in order to calculate energy consumption by current, voltage across each layer of the *p*-*i*-*n* diamond must be considered. Resistivity of boron doped diamond is obtained as approximately 0.1–10 Ω cm for 10^{18}–10^{20} cm^{-3} of boron concentrations [104]. Therefore, resistivity of the *p*-type layer of the sample used in this study ($[\mathrm{P}] = 10^{19}\,\mathrm{cm}^{-3}$, thickness: 500 µm) thought to be 10 Ω cm at most. Thus resistance of *p*-type layer under the top electrode on the mesa structure of *n*-type layer (area: $A = 100^2\pi\,\mu\mathrm{m}^2$) is estimated to $R_{p\text{-type}} = 10^5\,\Omega\,\mu\mathrm{m} \times 500\,\mu\mathrm{m}/A = 1.59\,\mathrm{k}\Omega$. The total resistance R of the *p*-*i*-*n* diode at $I_F = 0.40\,\mathrm{mA}$ ($V_F = 24.6\,\mathrm{V}$) is 61.5 kΩ (see figure D.1a). Therefore divided voltage across the *n*-type and *i*-layer is $V = V_F \times (R - R_{p\text{-type}})\,/R = 24.0\,\mathrm{V}$. Thus energy consumption by current flow under the top electrode is $J_{\mathrm{ele}} = V \times I_F/A = 0.000\,306\,\mathrm{mW}\,\mu\mathrm{m}^{-2}$. Next, optical-induced ionization rate $\gamma_{-0}^{\mathrm{opt}}$ is needed to compared optical rate with $\gamma_{-0}^{\mathrm{ele}}$. It is obtained from population of NV^0 (p_0^{eq}) and total rate with $\gamma_{-0}^{\mathrm{opt}} = p_0^{\mathrm{eq}}\left(\gamma_{-0}^{\mathrm{opt}} + \gamma_{0-}^{\mathrm{opt}}\right)$ (see equation (2.12)). Here $p_0^{\mathrm{eq}} = 0.49$ and total rate $\gamma_{-0}^{\mathrm{opt}} + \gamma_{0-}^{\mathrm{opt}}$ are obtained from figures 4.3a and 3.4, respectively. Required laser power P to achieve amplitude of rate $\gamma_{-0}^{\mathrm{opt}} = 0.70\,\mu\mathrm{s}^{-1}$ ($= \gamma_{-0}^{\mathrm{ele}}$ at 0.40 mA), equals to laser power which induce total rate of $\gamma_{-0}^{\mathrm{opt}} + \gamma_{0-}^{\mathrm{opt}} = \gamma_{-0}^{\mathrm{opt}}/p_0^{\mathrm{eq}} = 1.47\,\mu\mathrm{s}^{-1}$. It is $P = 1.20\,\mathrm{mW}$ derived from figure 3.4. Determination of laser spot size has not been done, but it might not be more than 1 µm. Thereby, the power density of laser at the focal point is calculated to $J_{\mathrm{opt}} = P/0.5^2\pi\,\mu\mathrm{m}^2 = 1.53\,\mathrm{mW}\,\mu\mathrm{m}^{-2}$. Conclusionary, the energy difference between electrical and optical method is estimated to $J_{\mathrm{ele}}/J_{\mathrm{opt}} = 0.000\,306/1.53 = 2 \times 10^{-4}$. The required energy for electrical method is four order of magnitude smaller than optical method to achieve the same ionization rate.

Phase 2

At phase 2, time evolution of charge state completed. Where charge state population is written as follow:

$$p_0^{\mathrm{eq}} = \frac{\gamma_{-0}^{\mathrm{ele}} + \gamma_{-0}^{\mathrm{opt}}}{\gamma_{-0}^{\mathrm{opt}} + \gamma_{0-}^{\mathrm{opt}} + \gamma_{-0}^{\mathrm{ele}}}, \tag{4.5}$$

when laser power reaches to 0, optical rates $\gamma_{-0}^{\mathrm{opt}}$ and $\gamma_{0-}^{\mathrm{opt}}$ also become 0. Then p_0^{eq} reaches to 1 in the phase in the dark condition.

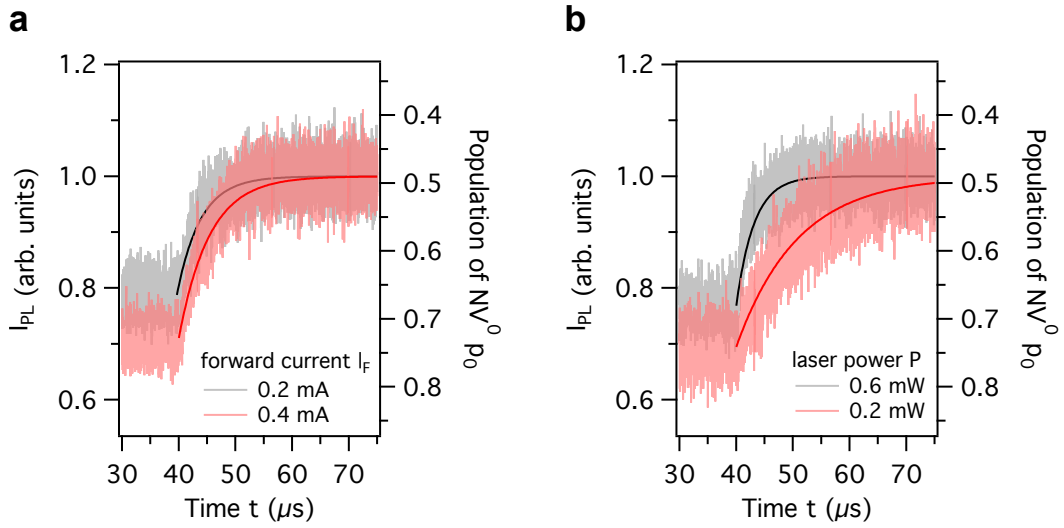

Figure 4.8.: Transition of charge-state during on- to off-state. **a,** Under fixed laser ($P = 0.4\,\mathrm{mW}$), transition rate slightly depend on forward current. Transition rates are $\gamma = 0.24\,\mu\mathrm{s}^{-1}$ ($I_F = 0.2\,\mathrm{mA}$) and $\gamma = 0.19\,\mu\mathrm{s}^{-1}$ ($I_F = 0.4\,\mathrm{mA}$). **b,** Under fixed current ($I_F = 0.3\,\mathrm{mA}$), transient depend on laser power. Transition rates are $\gamma = 0.093\,\mu\mathrm{s}^{-1}$ ($P = 0.2\,\mathrm{mW}$) and $\gamma = 0.32\,\mu\mathrm{s}^{-1}$ ($P = 0.6\,\mathrm{mA}$).

4.5. Recombination rate and reverse bias (phase 3)

Transition of charge-state population at off-state of the *p-i-n* diode (phase 3 in figure 4.5) is slower than that of on-state (phase 1) because there is no contribution of $\gamma_{-0}^{\mathrm{ele}}$ for the transition. Therefore, transition of charge state should be only assisted by laser excitation. However, optical induced total rate (fluorescence increase rate) at phase 3 is slower than total rate measured after 100 µs of current pulse (net optical induced rate, see figures 3.4 and 4.4a). This phenomenon can be explained by recombination of stored charge carriers in the intrinsic layer of sample. This section focused on how stored charge affect to charge state transition.

First, forward current and laser power dependence of charge state transition in phase 3 is discussed. Figures 4.8a,b are measurement results of I_{PL} at phase 3 with different forward current and laser power P. Under fixed laser power, transition rate slightly depends on forward current. Under fixed forward current, transition rate become 3 times large with 3 times increase of laser power.

More details of forward current and laser power dependence of transition rate is displayed in figure 4.9. In addition, net optical induced rate is also plotted (see figure 3.4). If increase of I_{PL} in phase 3 is only assisted by laser excitation, increase rate of I_{PL} should have same rate as net optical rate. However in figure 4.9, relatively large difference exists.

In order to understand this phenomenon, on- to off-state transition of *p-i-n* diode must be took into account. After carrier injected by forward bias applying, the *i*-layer

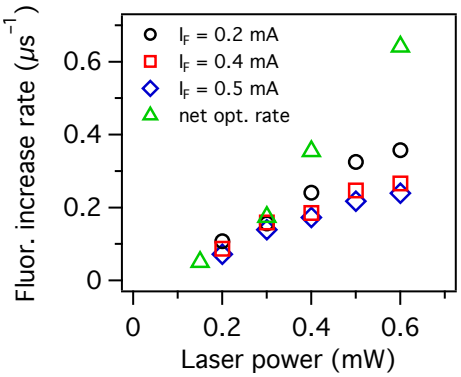

Figure 4.9.: Fluorescence increase rate in off-state and optically induced rate. Transition rate of I_{PL} at the phase 3 in figure 4.5 after different forward current injection and net optical induced rate.

is filled with major hole carriers. These carriers still remain in the i-layer even after forward bias is turned off. Then they recombine with electron carriers. It is thought that these remaining hole carriers might suppress recombination of single NVs and electrons. Recombination rate of injected hole and electron carriers is called carrier lifetime. The reported value is $\tau_L = 2.3\,\mu s$ in diamond [105]. In this section, stored charges in the i-layer, Q_s is considered. It is expressed as following equation [106]:

$$\frac{dQ_s}{dt} = -\frac{Q_s}{\tau_L} + I_F, \tag{4.6}$$

where I_F is a constant forward bias current. Under steady state conditions, $dQ_s/dt = 0$ and equation (4.6) reduces to:

$$Q_s = \tau_L I_F, \tag{4.7}$$

After forward current is turned off, charge carrier are eliminating by $Q_s(t) = Q_s(0)\mathrm{e}^{-\frac{t}{\tau_L}} = \tau_L I_F \mathrm{e}^{-\frac{t}{\tau_L}}$. This rate may affect to recombination of charge state in the on to off-state transition of the diode.

To gain insight into the carrier dynamics in the i-layer of the sample, reverse bias applying to the sample has been performed. It is known that stored charges in the i-layer are removed by reverse bias pulse after bias voltage pulse [106]. Figure 4.10 shows a typical current carve during reverse current I_R flow after forward current I_F. Removed charges during reverse bias is the same as stored charge during forward bias. Thus it can be written as:

$$Q_s = \tau_L I_F = \int_{t_0}^{\infty} i_R dt, \tag{4.8}$$

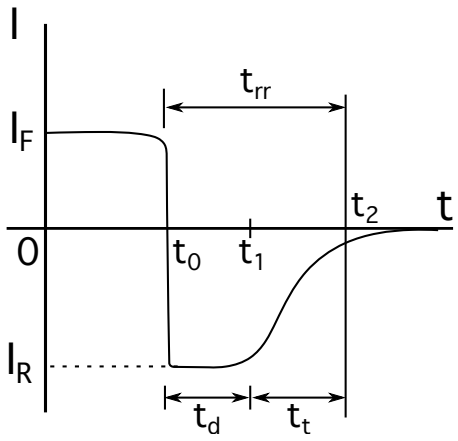

Figure 4.10.: Turn-off current model of a *p-i-n* diode. The diode is turned off from I_F (forward current) to I_R (reverse current) at t_0. t_{rr} is called recovery time.

here i_R is time dependent reverse current. The stored charges are removed during recovery time t_{rr} which is calculated by the following expression [107, 108]:

$$t_{rr} \approx \tau_L \ln\left(1 + \frac{I_F}{I_R}\right). \tag{4.9}$$

From this expression, recovery time becomes shorter when large reverse bias current flows in diode. To confirm this effect on the *p-i-n* diode, transition of I_{PL} with reverse bias applying is measured. Figure 4.11a is I_{PL} measurement on off- to on- state transition (the phase 3 in figure 4.5a) with reverse bias applying. The pulse sequence is displayed on the above of the graph. Reverse bias V_R is applied after constant forward bias voltage ($V_F = 25.3\,\mathrm{V}, I_F = 0.5\,\mathrm{mA}$). As a result, fluorescence increase rate becomes faster with increase of reverse bias. It is seen on solid fitting curves by exponential in figure 4.11a. The dependence is summarized in Figure 4.11b. Increase rate exponentially increase with increase of reverse bias voltage. Finally at the saturation, increase rate reaches to net optical induced rate under $P = 0.4\,\mathrm{mW}$ (see figure 3.4). From the measurements, it is thought that the stored hole carriers are eliminated by reverse bias and it helps NV to recombination with electron carriers.

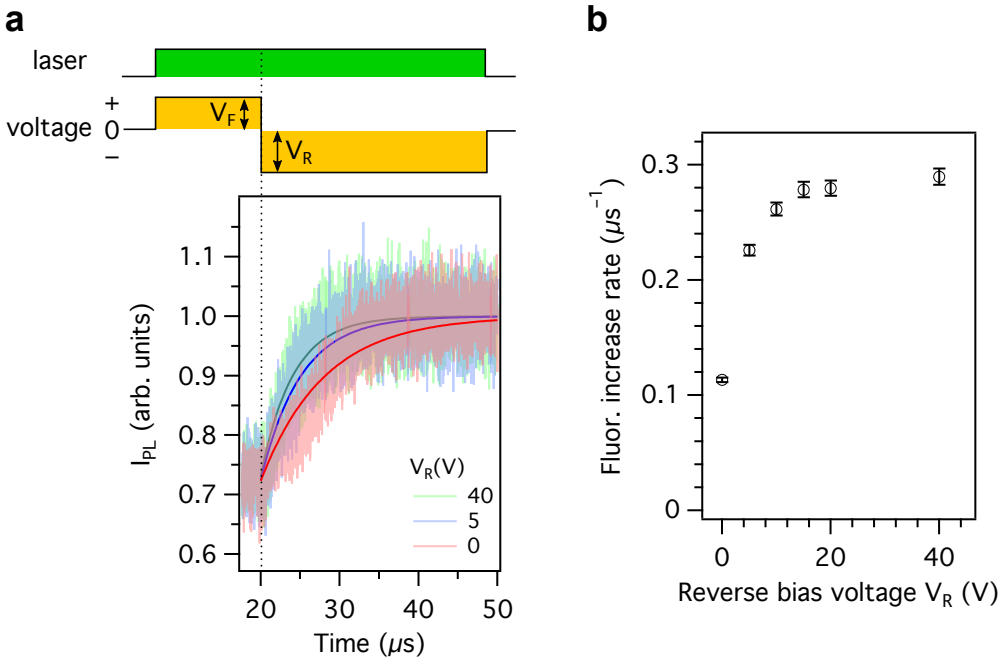

Figure 4.11.: Reverse bias and fluorescence increase rate. **a,** Reverse bias V_R modulates fluorescence increase rate during the recovery of charge state. V_R is applied after forward bias V_F at $t = 20\,\mu s$. **b,** Reverse bias dependence of fluorescence increase rate. Laser power and forward bias current was fixed to $0.4\,mW$ and $0.5\,mA$ $(25.3\,V)$, respectively.

4.6. Summary

First interest in the charge state dynamics of single NVs in *p-i-n* diode is that whether charge-state of a single NV is controllable or not. Spectra and intensity monitoring of photoluminescence during current injection reveal that injected hole carriers switch charge state of a single NV from NV^- ($S = 1$) to NV^0 ($S = 1/2$). Switching between two charge states which have different spin states open the new way to decouple among spins by means of electrical method.Control of charge state is purely electrical, deterministic, and transition rate is quantitatively revealed to $0.7\,\mu s^{-1}$ at 0.4 mA. Electrical induced ionization rate linearly depends on current is indicating that transition of charge state under this control is occurred in direct process.

In addition, quantitative estimation of electrical induced transition rate have impact because amplitude of decoupling is depends on the charge state switching rate versus hyperfine interaction among multiple spins. The present framework limits switching direction to one direction. Toward applying this method to such decoupling applications, bidirectional operation, both of ionization and recombination of charge state is a next task. However, present control speed is comparable to optical method and the energy costs for charge-state control are four order of magnitude smaller than that of optical. These facts show high potential of electrical charge state control of the NV.

5. Stabilize negatively charged state in *n*-type layers

This chapter focuses on the stabilization of negatively charge state (NV^-) of single NVs generated into *n*-type diamond layers. Phosphorus atoms are incorporated into layers to increase number of free electrons in bulk diamond. Thermally activated electrons recharge single NVs and perfectly stabilize into NV^- under weak optical illumination. Such effects are clearly seen in photodynamics (i.e. fluorescence intensity) of NVs. After NV is force ionized by strong laser excitation, recovery of charge state during dark condition (time region with no-optical illumination) is detected by fluorescence averaging measurement (FAM). In addition, phosphorus induced recharge rate is proportional to orange laser power under optical illumination. Thus NV^- keep high population ($p_- > 0.8$) even under high excitation power. Stabilization of charge state also appears in the difference in intensity of optically detected magnetic resonance (ODMR) of ground state of NV^-.

5.1. Preparation of *n*-type layers

The *n*-type layers were epitaxially grown on the (111)-oriented diamond substrates by chemical vapor deposition (CVD) technique. The incorporated amount of phosphorus atoms are controlled by the ratio of phosphine (PH_3) and hydrogen (H_2) mixed gas during CVD growth [47].

Nitrogen atoms are expected to naturally incorporated into diamond during CVD growth. The incorporation depends on the growth conditions (growth temperature, contamination in the chamber, etc.). Nitrogen atoms form a nitrogen-vacancy structure by high temperature in the chamber during CVD growth. If sufficient amount of nitrogens (more than $1 \times 10^{15}\,\mathrm{atoms\,cm^{-3}}$) are incorporated into the layer during growth, they are optically detectable with confocal microscope.

Total six *n*-type layers have been fabricated by CVD technique. Formation of these samples are listed up in table 5.1. Incorporation for (111) directions are two orders of magnitude lager than that on (001) (see section 2.1.2). Single NVs which have stable photon emission were founded in two samples. These samples are labeled are called h443 and h578. These labels are repeatedly used in this thesis. All of NVs in h443 stabled into NV^- has been revealed by single-shot charge-state measurement (SCM). Unfortunately, more insight of their charge state dynamics could not be obtained on

Table 5.1.: List of *n*-layers grown on (111) substrates. Nitrogen atoms are expected to naturally incorporated into the layers during growth of layers by the CVD technique to generate single NVs.

name	substrate	thickness (µm)	[P] (cm^{-3})	condition
h442	Ib (111)	10	1×10^{16}	single NVs, blinking
h443	Ib (111)	10	5×10^{15}	single NVs, stable emission
h445	Ib (111)	5	1×10^{16}	no single emitters
h446	Ib (111)	5	1×10^{14}	no single emitters
h466	IIa (111)	6	5×10^{15}	no single emitters
h578	Ib (111)	3∼5	5×10^{16}	single NVs, stable emission

h443. Because after measurement of SCM, ^{15}N atoms were ion-implanted to the sample to investigate charge-state stability of NVs in shallower region. However, it may have generated many defects which make charge-state of NVs unstable. Thus charge state dynamics measurements have been performed on h578 sample. More details of situation on h443 sample are exhibited in appendix E.

5.2. Raster scan images and fluorescence time traces

Raster scan image and measurement under green laser Fluorescence from single NVs is detected in h578 sample under green (532 nm) illumination is shown in figure 5.1a. There are no blinking and photobleaching on these NVs. Background fluorescence is almost same as intrinsic diamond and is sufficiently low to distinguish them as single photon emitters (see figure E.2). Here if charge state of NVs are stabilize into NV^-, photoluminescence/fluorescence intensity (I_{PL}) of them should be higher than that of NVs in intrinsic diamond. However, fluorescence intensity from all NVs are the same as NVs in intrinsic diamond due to green laser intensely affects to charge-state transition (13 times lager than orange laser, see figures 3.3a–c) then it hides the contribution from phosphorus atoms. In addition, results showing, PL spectra, and ODMR intensity between dim and bright NVs are also the same are displayed in figures 5.2a–c. These results imply that under green laser illumination, the charge-state population of dim and bright NVs are same. Then laser color is switched to orange which gently affects to the charge state in order to resolve charge state dynamics. Figure 5.1b is a scan image taken under 100 µW of orange laser illumination. Scan area is the same as the image taken under green laser excitation, figure 5.1a. In general, under this illumination condition, fluorescence intensity of NVs become lower compared with green laser because orange laser strongly ionize NVs (see figure 3.2b). An NV labeled "dim NV" in figure 5.1b is one of such ionized NV. However, some NVs (red circled in figures) are about five times brighter than dim NVs under orange laser excitation (∼50 versus ∼10 kcps). NV

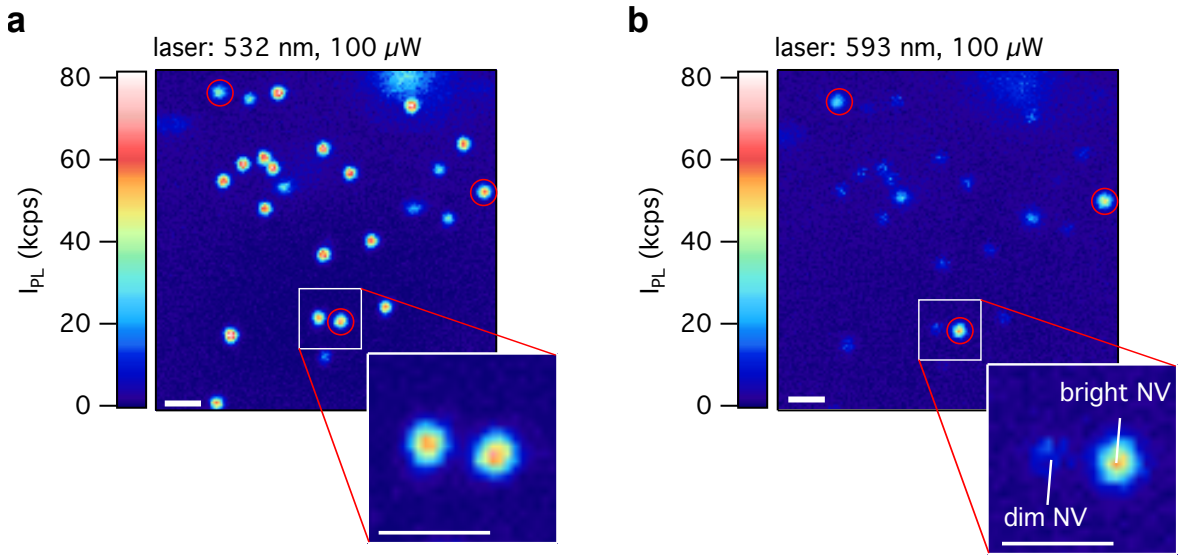

Figure 5.1.: Raster scan image of an *n*-layer under green and orange laser excitation. a, Under 100 µW, 532 nm illumination. All NVs show same optical behavior under green illumination. **b,** Scan image of the same area under orange illumination. Some NVs show five times larger fluorescence than that of dim ones. Scale bar, 1 µm.

marked with "bright NV" is a one of the bright NV. These bright NVs are recharged by activated electrons from phosphorus atoms and only slightly ionized by 100 µW, orange laser. In the latter discussions, investigations of photodynamics are performed on these dim and bright NVs.

Figure 5.3 is a orange laser power dependence of I_{PL} of dim and bright NVs. Bright NV produces larger photon counts than dim NV under wide range (1–500 mW) of excitation power. The difference of photodynamics between bright and dim NVs are clearly resolved by weak excitation intensity. Note: it is conceivable that some defects, which has shallower donor level than NV, exist vicinity of dim NV. This defects capture electrons from conduction band and NV cannot be recharged effectively. Differences of environment around these NVs also appear in transverse spin relaxation time (T_2) measurement. It is mentioned in chapter 5.6.

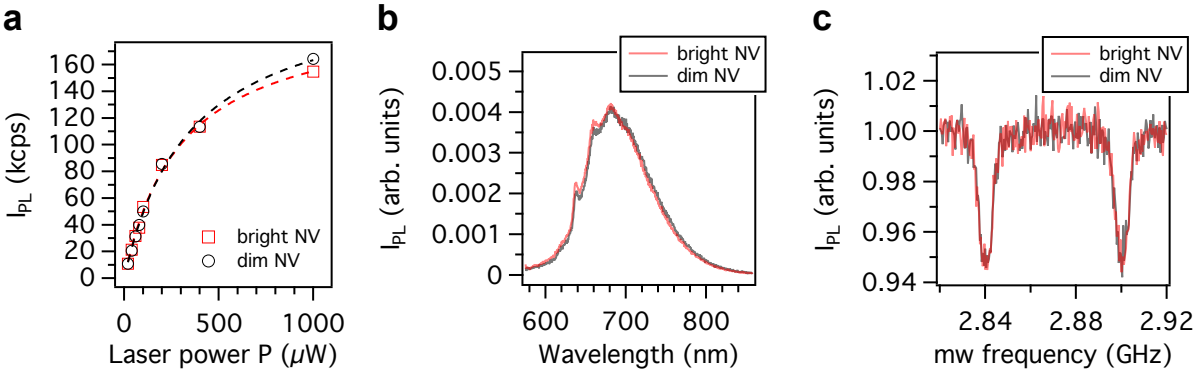

Figure 5.2.: Photodynamics and ODMR of dim and bright NVs under green laser excitation. **a,** Laser power dependence of photoluminescence (PL) intensity (dotted curves are fitted by equation shown in page 29). **b,** PL spectra. **c,** Optically detected magnetic resonance spectra. ODMR and PL spectra are taken under $532\,\mathrm{nm}$, $100\,\mu\mathrm{W}$ excitation. There are no significant differences between dim and bright NVs in every measurements.

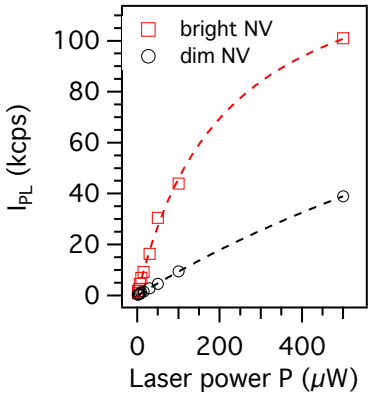

Figure 5.3.: Fluorescence intensity of dim and bright NVs under orange laser excitation. Red squares and black triangles are for the bright and the dim NVs, respectively. Dashed curves are data fits using a function $I_{PL} = I_{PL\mathrm{sat}} \times P/(P + P_{\mathrm{sat}})$ shown in the last paragraph of page 29.

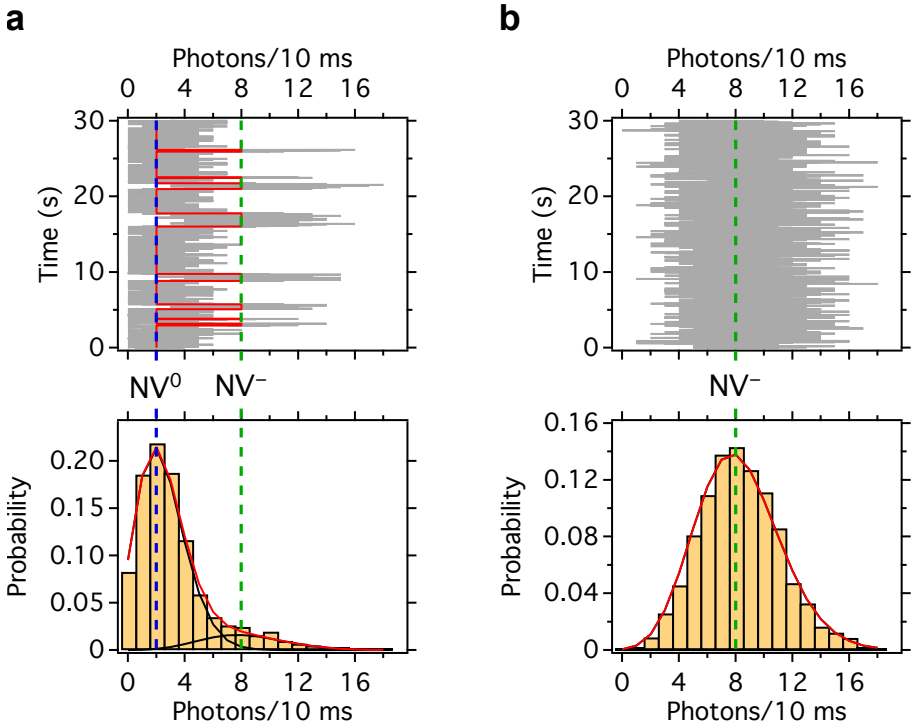

Figure 5.4.: Photoluminescence time trace of dim and bright NVs. a, (Upper panel) Under continuous 1 µW, 593 nm illumination, photon bursts occur when the charge state transforms into the NV^- state on dim NV. A solid red line shows the most probable fluorescence levels. Here the average lifetimes of the two charge states are 2.92 s (NV^0) and 0.589 s (NV^-). (Bottom panel) corresponding histogram of photon counts. **b,** (Upper panel) bright NV does not show photon bursts in the trace. (Bottom panel) corresponding histogram indicates that the peak position of photon counts is almost the same as that of NV^- of dim NV.

Fluorescence time trace Figure 5.4a is a fluorescence time trace of dim NV under orange laser 1 µW excitation. The optically induced charge-state interconversion is recorded as clearly separated two fluorescence levels from NV^- (high fluorescence counts) and NV^0 (low fluorescence counts). Distribution of photon counts are shown as histogram in the bottom panel of the figure. Photon counts of two peaks are distributed into 0.12 : 0.88. In addition, ionization and recombination rates are calculated to $\gamma_{-0} = 1/\tau_{NV^-} = 1/0.589 = 1.70\,s^{-1}$ and $\gamma_{0-} = 1/\tau_{NV^0} = 1/2.92 = 0.342\,s^{-1}$, respectively. Population and rate are also same as charge-state population detected by SCM measurement and time trace of NVs in intrinsic diamond (see figures 3.2b and 2.4b). Therefore, charge state dynamics of dim NV is same as NVs in intrinsic diamond. In contrast to dim NV, bright NV continuously keeps the fluorescence level of NV^- (fig-

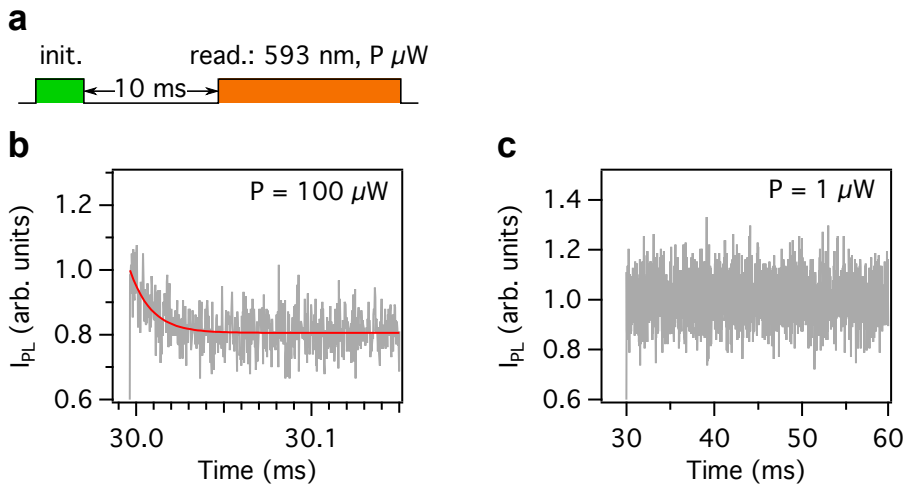

Figure 5.5.: Total transition rate during orange excitation on bright NV. **a,** Measurement sequence of the measurement. Total transition rate is detected as transition of I_{PL} during orange laser excitation. **b,** Ionization of charge state is detected under $P = 100\,\mu W$. **c,** Total transition rate depends on orange laser power P and become slower with decrease of P. At last under $P = 1\,\mu W$, no-transition is occurring means that total rate is zero ($\gamma_{-0} + \gamma_{0-} = 0$) under this illumination condition.

ure 5.4b[1]) and photon counts distribution has only one peak in its histogram. This histogram can be fitted by Poisson distribution function.

To elucidate whether bright NV has multiple charge states or not, transition rate measurement during orange laser illumination has been performed. If tremendously rapid transition is occurring during orange laser illumination, charge state interconversion cannot be resolved in time trace measurement. In such case, fluorescence intensity is averaged and a histogram should has only one peak, similar to figure 5.4b. Figure 5.5a is a measurement sequence of transition rate measurement. First, the charge state is initialized by green laser excitation. Charge state transition is measured by orange illumination. At laser power of orange laser $P = 100\,\mu W$, ionization of charge state is detected (see figure 5.5b) because laser power is relatively high. Total rate ($\gamma_{-0} + \gamma_{0-} = 0.08\,\mu s^{-1}$) is obtained by exponential fit to the result. Here total rate become slower with decrease of excitation power is obtained. At last in $P = 1\,\mu W$, total rate becomes to zero. This means no charge state transition is occurring during $1\,\mu W$, orange laser illumination.

[1]Photon counts of an eye guide (a red solid line) are rounded to integers, peak position of Poissonian in a histogram. In other cases, (i.e. figure 2.4b) most likely counts are derived by Baum-Welch algorithm [109].

5.3. Single-shot charge-state measurements

On n-type diamond layers, SCM has different meaning compared with that on NVs in intrinsic diamond and the p-i-n diamond diode. Basically in SCM, no-charge transition is hoped during dark condition (time region without optical illumination) between initialization and readout operation. Because SCM is aiming to measure charge state population during (and just after) initialization. However for bright NV, thermally activated electrons from phosphorus dopants recharged NV and change its charge state during dark condition. In other words, no matter how charge state is initialized into *any* populations by the initialization operation in the SCM , only one pattern, single peak at NV^- photon counts, appear in the results. Actually these facts is assured by SCM. On dim NV with the general measurement sequence of SCM shown in figure 5.6a, results (figure 5.6b) reflect charge-state population during initialization by green and orange laser and dim NV has same laser color dependence on charge state population as NVs in intrinsic layer (see figure 3.2). Differing from dim NV, bright NV has only one peak on the SCM with two initialization (see figure 5.6c). Peak profile are same as those of NV^- in figure 5.6b similar to time trace measurement in figure 5.4. Bright NV has only one peak in histogram of photon counts not only after initialization by orange laser but also after green laser initialization. If $p_- = 1$ (equals to A = 1 of NV^- in figure 5.6b) is satisfied not only under orange excitation but also under green laser illumination, it contradicts to photodynamics under green laser illumination (see figure 5.1a and 5.2a–c). Therefore, as for bright NV on n-type diamond layers, charge state population during and after arbitrary initialization condition (power and duration) cannot be measured nondestructively.

However SCM tells us important information of phosphorus induced transition rate. From results in figure 5.6b, it is apparent that charge state of bright NV is one-directionally recharged not depending on initialization condition. This means that phosphorus only affects to NV^0 and it turns charge state into NV^-, deterministically. Thereby, phosphorus induced ionization rate is $\gamma_{-0}^{\text{phos}} = 0$ and only recombination rate $\gamma_{0-}^{\text{phos}}$ have to be considered in discussions in after section.

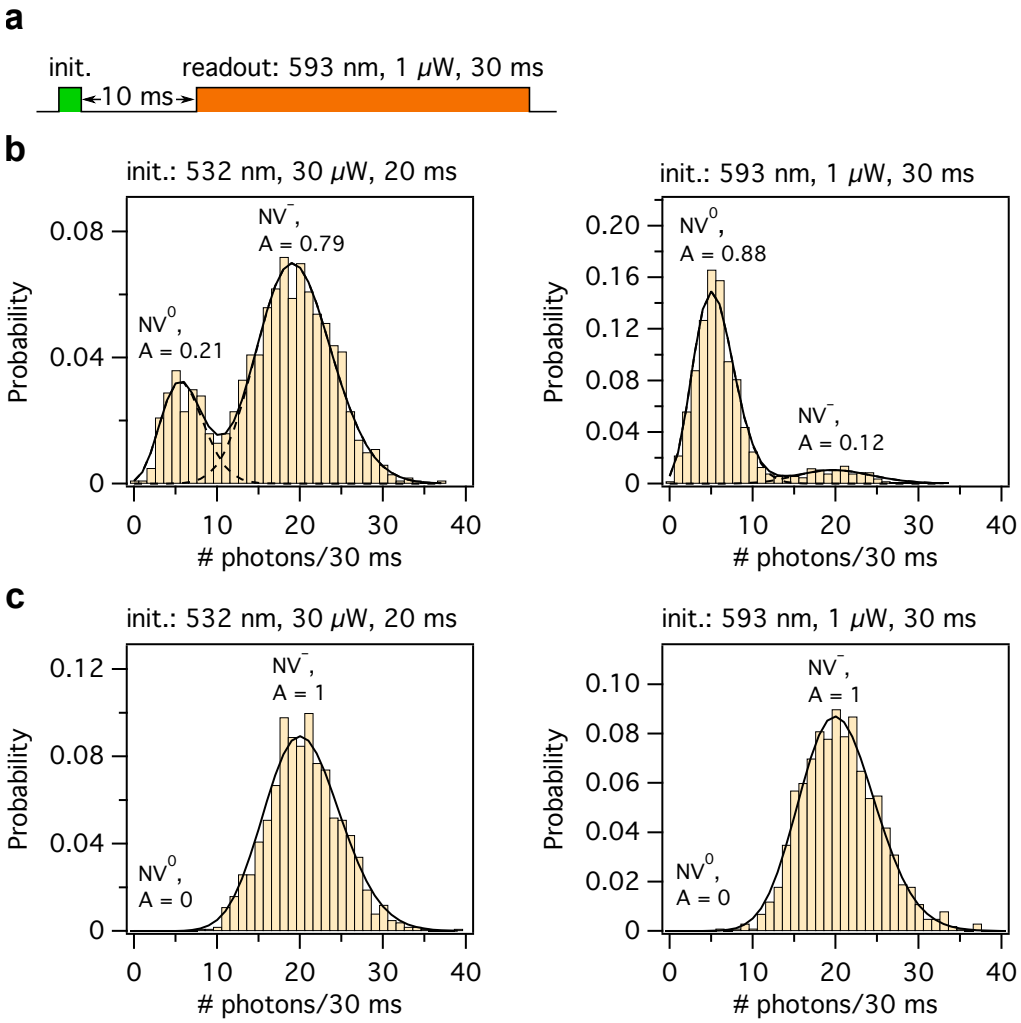

Figure 5.6.: Single-shot charge-state measurement on a dim and bright NVs. a, The pulse sequence used for single-shot measurement. **b,** Measurements on a dim NV with initialization by green (left) and orange (right) laser. Charge state population is the same as an NV in an intrinsic diamond. **c,** Measurements on a bright NV with initialization by green (left) and orange (right) laser. Both results have only photons from NV^-.

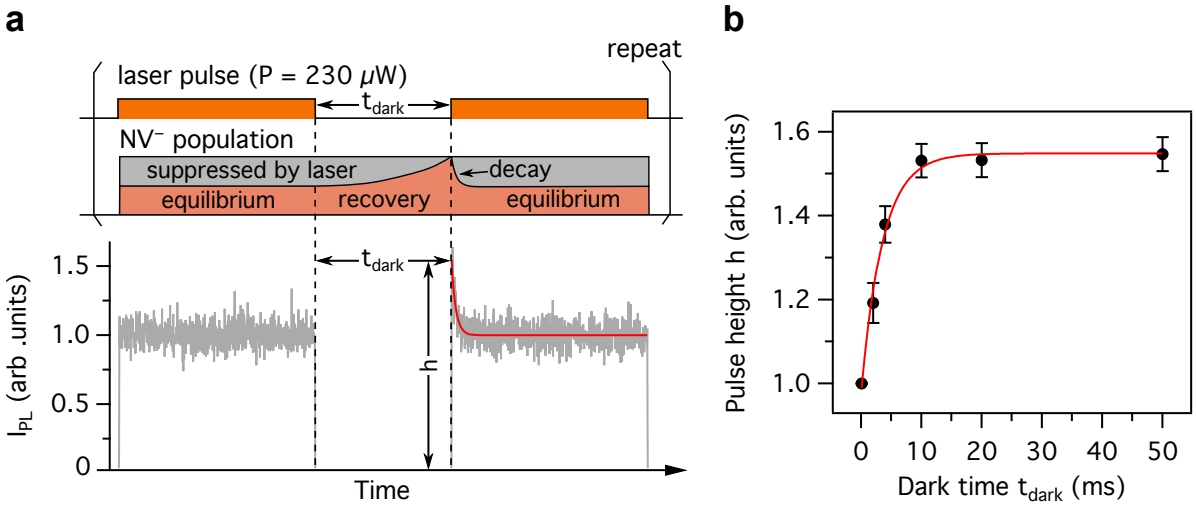

Figure 5.7.: Charge-state transition-rate during dark time. a, The pulse sequence used for a measurement of charge transition rate in the dark time t_{dark}. Photoluminescence intensity (I_{PL}) corresponds to the charge state population. The pulse height (h) reflects charge state recovering during t_{dark}. Laser power is set to 230 µW, can ionize both bright and dim NVs. **b,** Dark time dependence of pulse height h. The pulse height increase with t_{dark} increase. It corresponds to that increase of NV^- population during the dark time. A solid carve is fitting by a single exponential function $y = y_0 + C\exp(-t_{\text{dark}}/\tau_{\text{dark}})$. The rate $\gamma_{\text{dark}} = 1/\tau_{\text{dark}} = 0.28\,\text{ms}^{-1}$ which is charge state transition during t_{dark}.

5.4. Recombination/recharge rate in the dark condition

Bright NV is certainly recharged during dark condition is revealed from SCM. In order to detect this recharge dynamics, FAM with several time gaps of dark condition (dark time τ_{dark}) has been performed. Here recombination/recharge rate during dark condition is defined as γ_{dark}. Figure 5.7a is a concept of the measurement. Orange laser with relatively high power ($P = 230\,\mu\text{W}$) is used to force ionize NV and detect photon counts. During the first laser pulse, population probability of NV^- charge state (p_-) is suppressed by strong laser illumination and it is in a state of the equilibrium, $p_- < 1.0$. During dark condition τ_{dark}, after first pulse ends, p_- is start recovering to $p_- = 1$ assisted by phosphorus. Several dark time after, the second laser pulse again force ionize bright NV and consequently decay of I_{PL} is observed. Here the parameter h, the height of I_{PL} at the initial point of each pulse, reflects p_- at the end of each τ_{dark}.

Figure 5.7b is a dark time dependence of pulse height h. Pulse height does not change for short dark time, the first point of the figure ($t_{\text{dark}} = 0.1\,\text{ms}$). However, pulse height growth with increase of dark time after few millisecond of t_{dark}. By fitting with a single exponential function $y = y_0 + C\exp(-t_{\text{dark}}/\tau_{\text{dark}})$, γ_{dark} is estimated to

be $\gamma_{\mathrm{dark}} = 1/(3.6 \pm 0.4\,\mathrm{ms}) = 0.28 \pm 0.03\,\mathrm{ms}^{-1}$. Existence of γ_{dark} determines whether a NV has single peak in the SCM result or not. Conclusionary, charge-transition rate in n-type diamond during dark time (where laser power $P = 0$, literally dark condition) is expressed as:

$$\gamma_{0-}^{\mathrm{phos}}(P)\Big|_{P=0} = \gamma_{\mathrm{dark}} = 0.28 \pm 0.03\,\mathrm{ms}^{-1}. \tag{5.1}$$

Apparently time constant of recombination rate during dark condition (inverse of γ_{dark}) is almost one order of magnitude shorter than the detection window of SCM (3.6 ms versus 30 ms). This is why only one peak appears in the result of SCM at any initialization conditions, on bright NV.

5.5. Charge-state population and recombination rate under laser excitation

Transition rate during dark condition is only considering thermal activation of phosphorus. There is a possibility that phosphorus can be activated not only thermally but also photoionized by laser excitation [110, 111]. Optical excitation is a key tool in order to initialize and readout spin state of NVs. Thus it is important to investigate charge state dynamics under laser illumination in n-type diamond. The FAM provide us population probability and total transition rate on dim and bright NVs under optical illumination.

Figures 5.8a–c are FAM during orange laser excitation with several excitation power on dim and bright NVs. Figure 5.8a is a measurement sequence. First initialization pulse ($\lambda_{\mathrm{ext}} = 532\,\mathrm{nm}$, $P = 100\,\mu\mathrm{W}$) sets the population of NV^- (p_-) at $p_- = \sim 0.8$. After initialization, orange laser illuminate dim and bright NVs to force ionize them and detect transition of charge state. Dark time between initialization and readout pulse is set to 10 ms. This is long enough for bright NV that its population reaches to state of the equilibrium, $p_-^{\mathrm{eq}} = 1$, by γ_{dark} Figure 5.8b is a transition measurement under 100, 150 and 200 µW of laser power on dim NV. Decrease of I_{PL} are observed under all excitation powers and rate depends on laser power. Fluorescence intensity I_{PL} decay to the same amplitude ($\langle I_{PL} \rangle = 0.22$, $\sigma_{I_{PL}} = 8.72 \times 10^{-3}$) means that p_- does not depend on laser power under relatively higher illumination power as well as lower excitation (see figure 2.5b). Note that I_{PL} is normalized to 1 by $y_0 + C$ of fitting function ($y = y_0 + C\exp(-\gamma t)$) where $t = 0$. Here p_- during orange laser excitation can be calculated with same analogy used to link I_{PL} to population probability on p-i-n diamond diode. First, for dim NV, populations p_- after initialization by green and orange laser are determined to 0.79 and 0.12 by means of SCM (see figure 5.6b). Therefore, all transitions shown in figure 5.8b is started at $p_- = 0.79$ and end up to $p_- = 0.12$. These facts can be used to link I_{PL} to p_- quantitatively, thus relation between difference in PL intensity (ΔI_{PL}) and population of NV^- (Δp_-) is written as $\Delta p_- / \Delta I_{PL} = (0.12 - 0.79)/(0.22 - 1.00) = 0.67/0.78$. Population calculated by this relation is displayed in the right axis of figure 5.8b. As for bright NV, it is reveled that population probability p_- reaches to $p_- = 1$ after the enough long dark time. Therefore, $p_- = 1$ is satisfied at $t = 0\,\mathrm{s}$ for bright NV. Thus p_- during transition and at state of the equilibrium can be calculated with $p_- = 1.00 - (0.67/0.78)(1.00 - I_{PL})$. It is shown in the right axis of figure 5.8c. Measured population p_- at states of the equilibrium of dim and bright NVs are plotted in figure 5.8e as triangles (dim NV) and red circles (bright NV). Population of NV^- on bright NV is approximately 8–7 times larger than that of dim NV under 1–200 µW of illumination power.

Population probability p_- under other arbitrary laser power can be calculated by using relation of population and transition rate shown in equation (2.11). Total transition rate of dim and bright NVs under optical illumination are written as $\gamma_{\mathrm{dim}} = \gamma_{-0}^{\mathrm{opt}} + \gamma_{0-}^{\mathrm{opt}}$ and $\gamma_{\mathrm{bright}} = \gamma_{-0}^{\mathrm{opt}} + \gamma_{0-}^{\mathrm{opt}} + \gamma_{0-}^{\mathrm{phos}}$, respectively. Here superscripts "opt" denote that it is a

optically induced transition rate. Total transition rate of dim and bright NVs measured by FAM is shown in figure 5.8d. These points are fitted with the following functions:

$$\gamma_{\mathrm{dim}}(P) = \gamma_{-0}^{\mathrm{opt}} + \gamma_{0-}^{\mathrm{opt}} = aP + bP^2, \tag{5.2}$$

$$\gamma_{\mathrm{bright}}(P) = \gamma_{-0}^{\mathrm{opt}} + \gamma_{0-}^{\mathrm{opt}} + \gamma_{0-}^{\mathrm{phos}} = \gamma_{\mathrm{dark}} + cP + dP^2, \tag{5.3}$$

here fitting constants are $a = 2.28 \times 10^{-5}\,\mu\mathrm{s}^{-1}\,\mu\mathrm{W}^{-1}$, $b = 1.64 \times 10^{-6}\,\mu\mathrm{s}^{-1}\,\mu\mathrm{W}^{-2}$, $c = 5.42 \times 10^{-4}\,\mu\mathrm{s}^{-1}\,\mu\mathrm{W}^{-1}$, and $d = 2.13 \times 10^{-6}\,\mu\mathrm{s}^{-1}\,\mu\mathrm{W}^{-2}$. Ionization rate in the dark condition is already measured as $\gamma_{\mathrm{dark}} = 2.80 \times 10^{-4}\,\mu\mathrm{s}^{-1}$ in the previous section. From above fitting parameters, $\gamma_{0-}^{\mathrm{phos}}$ is written as follows:

$$\gamma_{0-}^{\mathrm{phos}}(P) = \gamma_{\mathrm{bright}} - \gamma_{\mathrm{dim}} = \gamma_{\mathrm{dark}} + (c-a)P + (d-b)P^2. \tag{5.4}$$

Fitting results of rates γ_{dim}, γ_{bright}, and calculated $\gamma_{0-}^{\mathrm{phos}}$ are plotted in figure 5.8d as solid carves. $\gamma_{0-}^{\mathrm{phos}}$ is linearly depends on laser power is shown.

Equations (5.2)–(5.4) allow us to calculate charge state population under arbitrary excitation laser power. By using equation (2.11), population probability of charge-state at a state of the equilibrium (p_{eq}) of dim and bright NVs are written as follows:

$$\begin{pmatrix} p_-^{\mathrm{eq}} \\ p_0^{\mathrm{eq}} \end{pmatrix} = \begin{cases} \frac{1}{\gamma_{-0}^{\mathrm{opt}} + \gamma_{0-}^{\mathrm{opt}}} \begin{pmatrix} \gamma_{0-}^{\mathrm{opt}} \\ \gamma_{-0}^{\mathrm{opt}} \end{pmatrix} & \text{(dim NV)}, \\ \frac{1}{\gamma_{-0}^{\mathrm{opt}} + \gamma_{0-}^{\mathrm{opt}} + \gamma_{0-}^{\mathrm{phos}}} \begin{pmatrix} \gamma_{0-}^{\mathrm{opt}} + \gamma_{0-}^{\mathrm{phos}} \\ \gamma_{-0}^{\mathrm{opt}} \end{pmatrix} & \text{(bright NV)}. \end{cases} \tag{5.5}$$

Total transition rate of dim NV ($\gamma_{-0}^{\mathrm{opt}} + \gamma_{0-}^{\mathrm{opt}}$) and bright NV ($\gamma_{-0}^{\mathrm{opt}} + \gamma_{0-}^{\mathrm{opt}} + \gamma_{0-}^{\mathrm{phos}}$) under arbitrary laser power are calculated by using equation (5.2) and (5.3). One-directional rates $\gamma_{0-}^{\mathrm{opt}}$ and $\gamma_{-0}^{\mathrm{opt}}$ are calculated as $\gamma_{-0}^{\mathrm{opt}} = p_0^{\mathrm{eq}}\left(\gamma_{-0}^{\mathrm{opt}} + \gamma_{0-}^{\mathrm{opt}}\right) = 0.88\gamma_{\mathrm{dim}}$ and $\gamma_{0-}^{\mathrm{opt}} = p_-^{\mathrm{eq}}\left(\gamma_{-0}^{\mathrm{opt}} + \gamma_{0-}^{\mathrm{opt}}\right) = 0.12\gamma_{\mathrm{dim}}$ by using equation (2.12) and from the SCM on dim NV (see figure 5.6b). Finally, $\gamma_{0-}^{\mathrm{phos}}$ is obtained by using equation (5.4). Calculation results of p_-^{eq} and p_0^{eq} are displayed in figure 5.8e. A red solid and black dashed-dotted carve are p_-^{eq} for bright and dim NVs, respectively. The calculation is good agreement with measurement results of charge-state population displayed as red circles and black triangles in the same figure. A green dotted carve is a calculation of population using $\gamma_{0-}^{\mathrm{phos}} = \gamma_{\mathrm{dark}}$ in equation (5.5), means only γ_{dark} is taken into account for bright NV in the calculation. Population p_-^{eq} rapidly decreases with laser power increases is shown. At 100 µW, p_-^{eq} is almost the same as that of dim NV. Admittedly, this fact contradict to the difference in fluorescence intensity between bright and dim NVs under orange excitation (e.g. figure 5.1). Thus phosphorus induced ionization rate surely enhanced by optical illumination with orange laser and it linearly increases with increase of orange-laser power.

On the contrary to orange laser, $\gamma_{0-}^{\mathrm{phos}}$ is not detectable under green laser excitation. Figure 5.9 is a measurement result of I_{PL} transition under green laser excitation, after initialization by orange laser pulse. Dark time between initialization and readout is set to 100 µs [2]. Opposite directions of transition are observed because initial population (equals to the population under orange laser illumination) of NV^- is different between the bright and dim NVs. From the data fit by single exponential function, transition rate is almost same between two NVs. This means that the ratio $\gamma_{0-}^{\mathrm{phos}}/(\gamma_{-0}^{\mathrm{opt}} + \gamma_{0-}^{\mathrm{opt}})$ for green laser illumination is quite smaller than that under orange laser illumination.

[2]Here the dark time length is shorter than the inverse of transition rate during dark time ($1/\gamma_{\mathrm{dark}}$). However, this does not affect to the transition rate during green laser excitation. See appendix E for more information.

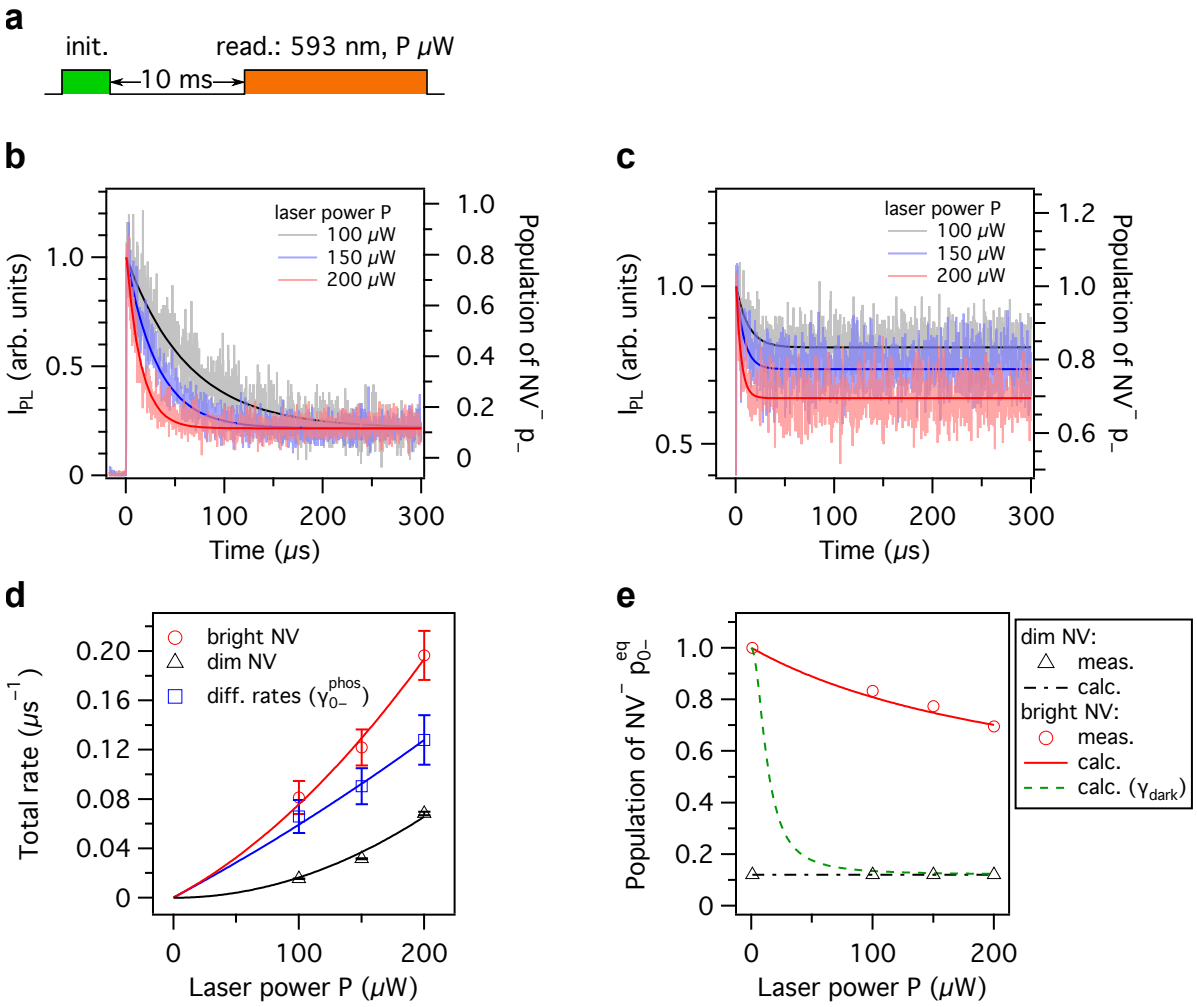

Figure 5.8.: Transition and population of charge state during orange laser excitation. **a,** Pulse sequence for the measurement. Measurement is performed on the several laser power (P) of orange laser with fixed power of initialization by green laser. **b,** Transition of fluorescence intensity of dim NV with laser power of 100, 150 and $200\,\mu\mathrm{W}$. The laser power become weaker, the transition become slower. I_{PL} decay to the same amplitude regardless of laser power. **c,** Transition rate of bright NV show higher transition rate and population depends on laser power. **d,** Laser power dependence of transition rate. Difference of rates $\left(\text{diff. rates} = \gamma_{\text{bright}} - \gamma_{\text{dim}} = \gamma_{0-}^{\text{phos}}\right)$ is linearly depends on laser power. **e,** Calculation and measurement results of charge state population of dim and bright NVs with arbitrary illumination power of orange laser. Error bars for measurement results are negligibly small ($<1\,\%$).

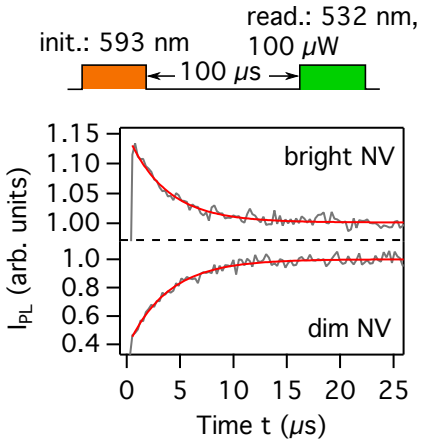

Figure 5.9.: Charge-state transition of dim and bright NVs under green laser excitation. Sign of transition is opposite between two NVs because initial population ($= p_-$ during orange laser excitation) is different. Dark time between green and orange excitation is set to $100\,\mu s$. These are no significant differences in transition rates for bright and dim NVs (0.27 ± 0.02 and $0.26 \pm 0.01\,\mu s^{-1}$, respectively).

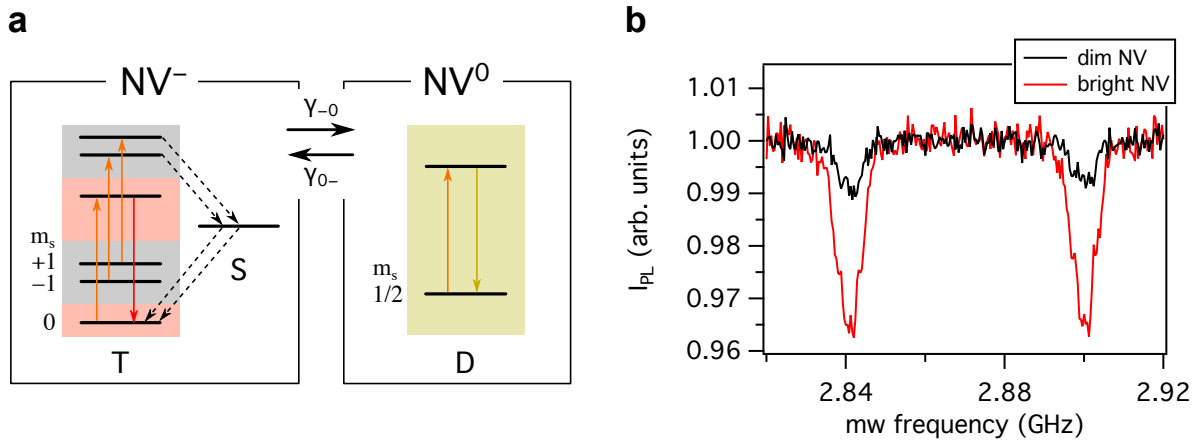

Figure 5.10.: Optically detected magnetic resonance on a dim and bright NVs. **a,** Energy diagram of NV^- and NV^0 which are linked with ionization and recombination rates. Both of NV^- and NV^0 have fluorescence in the off-resonance transition. ODMR signal is only detected on NV^- when microwave (mw) resonant to electron. Thus charge-state transition deteriorate ODMR signal intensity. **b,** ODMR spectrum taken under 200 µW pumping by orange laser. Signal intensity from bright NV is 4.18 times larger than that from dim NV with area calculation of each dip.

5.6. ODMR and spin coherence measurements

Different dynamics of the charge state between dim and bright NVs are revealed under orange laser excitation. The spin signal detection, for example ODMR measurement also reflect charge state stabilization in its signal intensity. Figure 5.10a is a schematic illustration of spin state of NV^- and NV^0 charge state. Two charge state is connected with transition rate γ_{-0} and γ_{0-}. The NV^0 charge state has spin dependent fluorescence. If NV resides in NV^- and spin resonance by microwave occurs in its ground state, decrease of I_{PL} is observed. When charge state changed into NV^0, decrease of I_{PL} cannot be seen at spin resonance frequency because NV^0 has no spin dependent fluorescence. Figure 5.10b display ODMR spectra of dim and bright NVs with a 1 mT magnetic field along the [111] direction of the diamond crystal under 200 µW, orange laser illumination. Dim NV is ionized by orange laser and population probability of NV^- (p_-) has small value, 0.12. Detectable spin signal from ODMR should be also suppressed to around 0.12. On the contrary to dim NV, p_- of bright NV is about 6 times lager ($0.70/0.12 = 5.83$) than that of dim NV at 200 µW of orange laser illumination (see figure 5.8e). Thus lager intensity of ODMR signal is detected on bright NV. As a result, ODMR intensity of bright NV is 4.18 times lager than that of dim NV. Here ODMR intensity is calculated by the area of ODMR spectra in the figure. The enhancement factor of ODMR intensity (4.18) is slightly smaller than ratio of charge-state population between dim and bright NVs. This might be contributed to difference in the dynamics of ODMR; however the details are unknown because these two NVs are in the exactly same condition of

quantization axis, laser polarization, and magnetic field intensity, whose miss align cause inhomogeneities in spectral shape and intensity [112].

Finally spin-coherence time T_2 has been measured by Hahn echo technique, because a long T_2 is critical for quantum information and sensing. Figures 5.11a–e are a T_2 measurement on bright and dim NVs in h578 sample. Pulse sequence used for this measurement is shown in figure 5.11a. Initialization by green laser bring spin state to its initial $|0\rangle_e$ state. The first $\pi/2$ (half pi) pulse set electron state to superposition states of $|0\rangle_e$ and $|-1\rangle_e$ state according to equation (3.6) (with $\theta = \pi/2$):

$$|\Psi\rangle = \frac{1}{\sqrt{2}}\left(|0\rangle_e + |-1\rangle_e\right). \tag{5.6}$$

on this coordinate, state $|\Psi\rangle$ start to decehere during time gap between first half pi and pi pulse ($\tau/2$ in the sequence). This decay of state is called inverse inhomogeneous broadening; decay constant of FID (T_2^*). By applying π pulse, dephased state can "refocus" at $|\Psi\rangle = \frac{1}{\sqrt{2}}\left(|0\rangle_e - |-1\rangle_e\right)$. The final half pi pulse is used to project spin state to fluorescence intensity at $m_s = 0$. Finally spin state is readout by final green laser. Here T_2 is measured as decrease of I_{PL} at readout.

As a result in h578 sample, T_2 is varied 16.6–19.8 µs for bright NVs and 2.4–3.1 µs for dim NVs. T_2 of dim NVs in h578 sample has much shorter than that of bright NV. This may comes from the difference of local environment among two nitrogen-vacancy centers (NVs). This difference may also affect to the charge state of two NVs.

For h443 sample ($[\mathrm{P}] = 5 \times 10^{15}\,\mathrm{atoms\,cm^{-3}}$), T_2 is estimated to be 50 ± 2 µs is shown in figure 5.12. In order to compare other diamond layer, investigation on T_2 of nitrogen atom (P1 centers) is considered. In previous report [113], T_2 are 1 ms and 100 µs for the P1 concentration of 5×10^{15} and $5 \times 10^{16}\,\mathrm{atoms\,cm^{-3}}$, respectively. Because the unpaired electrons localize on both of phosphorus and P1 center, Dependence of the phosphorus concentration on T_2 of NV centers might to be almost the same as that of the P1 center. However, the measurement results of T_2 are shorter than the expected values on h578 sample. It might be attributed to other impurities or defects [21, 114]. In other words, if these impurities or defects could be reduced and if ^{12}C could be enriched (reduce ^{13}C, $I = 1/2$), T_2 in n-type diamond should become comparable to the long (millisecond order) T_2 of high-quality intrinsic ^{12}C-enriched diamond [100].

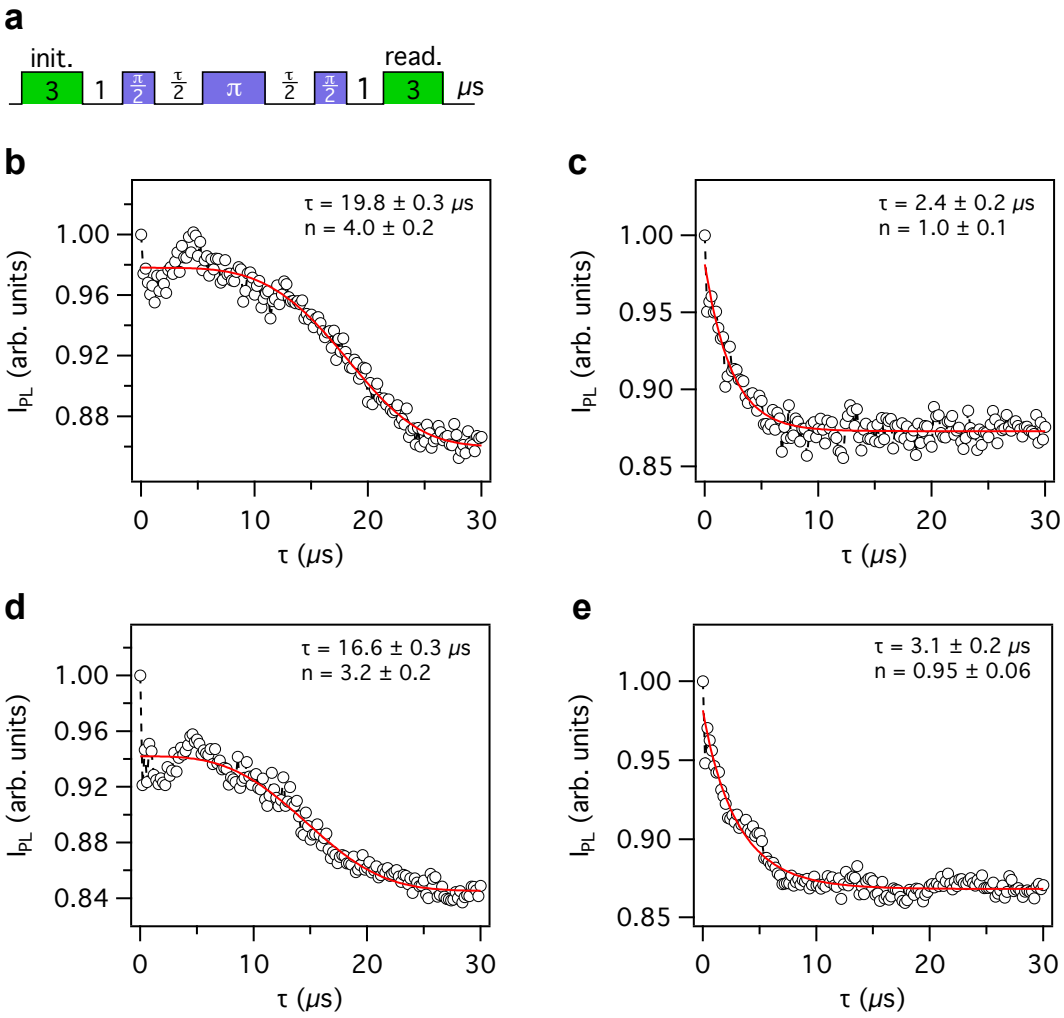

Figure 5.11.: Coherence time of dim and bright NVs. a, Pulse sequence of T_2 measurement. **b,** Echo signal on bright NV center. T_2 is $19.8\,\mu s$. **c,** On dim NV center. T_2 is $2.4\,\mu s$. **d, e,** Spin echoes on other bright and dim NVs show reproducible results. T_2 decay is found to fit with function $\exp\left[-\left(\tau/T_2\right)^n\right]$.

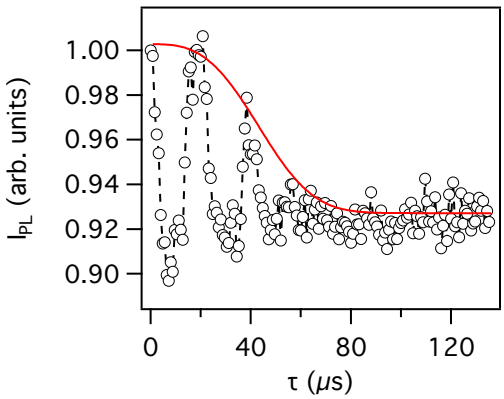

Figure 5.12.: Coherence time of a single NV in h443 sample. T_2 decay is found as $50 \pm 2\,\mu s$ to fit height of each envelop to function $\exp\left[-(\tau/T_2)^3\right]$. The concentration of phosphorus of this sample is $[P] = 5 \times 10^{15}\,\mathrm{atoms\,cm^{-3}}$.

5.7. Summary

The single NVs in n-type diamond layers show completely different charge state dynamics compared with those in intrinsic diamond. Under dark condition, recombination of charge state by activated electrons from phosphorus atoms are measured and recombination rate is determined to $0.28 \pm 0.03\,\mu s$. In addition, recombination rate depend on the laser power, this might comes from the activation of phosphorus atom by optical illumination. Thanks to this effect, large amplitude of ODMR is observed even under relatively high, orange laser of $200\,\mu W$ illumination. The spin coherence time of both dim and bright NVs are shorter than the expected value; however engineering of impurities other than phosphorus might lengthen the coherence time. Further investigations are needed to explain the difference behavior among NVs (dim and bright NVs), however this technique to stabilize charge state is promising to improve fidelity of quantum manipulation and stability of emitted photons.

6. Conclusion

In order to meet the requirement for applications of NV^- and gain insight of the charge state dynamics, this study control and investigate charge state of single NVs in two different platforms.

As for the *p-i-n* diode, charge state is completely ionized to neutral state (NV^0). This transition is caused by major hole carriers injected from a *p*-type layer. Consequently hole recombine occurs at NV site and an electron of NV recombined with hole. It makes charge state into neutral. Importantly, control is deterministically and NV keep its charge state longer than 0.45 ms after operation. To evaluate whether this method is hopeful or not, comparison with optical induced charge state switching is performed. As a result, ionization rate is comparable to optical induced one, $0.7\,\mu s^{-1}$. The direction of charge control on the *p-i-n* diode is limited to one direction to date. This must be overcome to perform all-electrical control of charge state for the spin related applications. However, energy costs for charge state switching is four order of magnitude smaller than that of optical methods. Furthermore, recombination of charge state can be controlled by applying reverse bias to the sample, means indeed charge state of NV are modulated by injected and stored carriers in the *i*-layer. This imply that it is possible to recharge NV (control NV^0 to NV^-) by introducing the highly phosphorous-doped *n*-type layer to inject electron into *i*-layer as majority carriers. This might pave the way to the stabilization and achievement of electroluminescence (EL) detection of negatively charged state (NV^-).

From the studying in the *n*-type layer, it is shown that the phosphorus doping is promising technique to stabilize NV^- charge state in diamond layer. NV does not show interconversion of charge state even under optical illumination of orange (593 nm) laser. It is revealed that recombination of NV occurs during dark condition with rate of $0.28\,ms^{-1}$. Thermally activated elections from phosphorus dopants assist recharging of single NVs. In addition, this recharging rate can be accelerated by orange laser illumination. Stabilization of charge state also appears in ODMR indicates that fluorescence bright NV is surely originated from NV^-. Toward qubit operation on *n*-type diamond, short T_2 of NV must be overcome and it is important to determine what impurities or defects be decoherence sources in *n*-type layer. Additional future tasks are to acquire more insight of phosphorus concentration dependence of recombination rate and spin coherence time.

A. Units and Physical Constants

quantity	unit	symbol	dimension
Magnetic field	Tesla	T=10^4 G	$\mathrm{Wb\,m^{-2}}$
Photon count (count rate)	counts per second	cps	$\mathrm{s^{-1}}$
Current	Ampere	A	A
Electric dipole moment	Debye	D or Debye	C m
Excitation laser intensity	Watt	W	$\mathrm{J\,s^{-1}}$

symbol	name	value
e	elementary charge	1.60×10^{-19} C
h	Planck constant	6.62×10^{-34} J s
m_0	free electron mass	9.11×10^{-31} kg
k_B	Boltzmann constant	1.38×10^{-23} J K^{-1}
μ_B	Bohr magneton	927.4×10^{-26} J T^{-1}

B. Raising time and beam size dependence on beam diameter

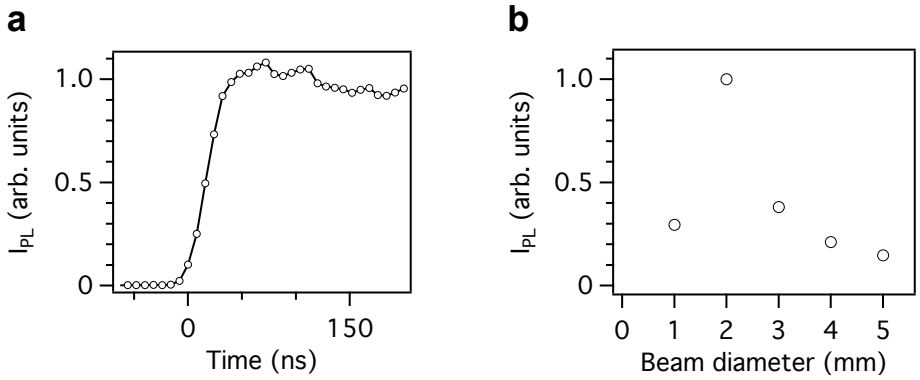

Figure B.1.: Response to pulse input and beam size dependence of fluorescence intensity. **a,** Fluorescence response of NV when green laser pulse is input. **b,** Beam diameter dependence of fluorescence intensity under orange laser excitation.

Raise time of the laser pulse Raise time of laser pulse is an important factor to measure charge-state transition in non-single-shot charge-state measurement (SCM). The raise time depends on electrical response time of acosto-optic modulator (AOM)s, and avalanche photodiode (APD)s. Especially, incident beam size and power to the AOM determine the raise time. Anyway, observed response of photoluminescence/fluorescence intensity (I_{PL}) contains these total effects. Figure B.1 is raising time measurement by using green laser (532 nm) illumination. I_{PL} is from a single NV excited by the laser. From this result, raising time of the pulse (the pulse raises from 10 to 90 % of the maximus) is approximately 32 ns. This time is sufficiently faster than the response of charge state transition induced by current and laser pulses.

Beam size of orange laser and excitation efficiency The beam size of the laser spot is significantly affects to the excitation efficiency of single defects in a sample. Figure B.1 is a beam diameter of orange laser and outcome I_{PL} from single NV. The NV shows maximum fluorescence at beam size of 2 mm. In the two-laser confocal microscopic system, it is important to precisely adjust two laser beam on the same optical axes.

C. The solution to the rate matrix of the charge-state transition

The solution to the rate equation (2.9) is given by following steps. A matrix A in equation (2.9) is a regular matrix, thus it can be diagonalized into a matrix D with an eigenvector matrix P:

$$D = P^{-1}AP = \begin{pmatrix} \lambda_1 & 0 \\ 0 & \lambda_2 \end{pmatrix}, \tag{C.1}$$

where λ_1 and λ_2 are the eigenvalues of the matrix A. Here the equation (2.9) can be simplified with D and $y = P^{-1}p(t)$:

$$P^{-1}\dot{p}(t) = \underbrace{P^{-1}AP}_{D} P^{-1}p(t), \tag{C.2a}$$

$$\frac{d}{dt}(P^{-1}p(t)) = DP^{-1}p(t), \tag{C.2b}$$

$$\frac{dy}{dt} = Dy. \tag{C.2c}$$

Write down y into its components:

$$\frac{d}{dt}\begin{pmatrix} y_1 \\ y_2 \end{pmatrix} = \begin{pmatrix} \lambda_1 & 0 \\ 0 & \lambda_2 \end{pmatrix}\begin{pmatrix} y_1 \\ y_2 \end{pmatrix}. \tag{C.3}$$

The equation (C.3) has solutions of:

$$y_1 = y_1(0)\mathrm{e}^{\lambda_1 t}, \tag{C.4a}$$

$$y_2 = y_2(0)\mathrm{e}^{\lambda_2 t}, \tag{C.4b}$$

$$y = \begin{pmatrix} y_1 \\ y_2 \end{pmatrix} = \begin{pmatrix} \mathrm{e}^{\lambda_1 t} & 0 \\ 0 & \mathrm{e}^{\lambda_2 t} \end{pmatrix}\begin{pmatrix} y_1(0) \\ y_2(0) \end{pmatrix}. \tag{C.4c}$$

Deform y into p with $p(t) = Py$ and $y(0) = P^{-1}p(0)$, then $p(t)$ is represented as:

$$p(t) = Py = P\begin{pmatrix} \mathrm{e}^{\lambda_1 t} & 0 \\ 0 & \mathrm{e}^{\lambda_2 t} \end{pmatrix} P^{-1}p(0). \tag{C.5}$$

The eigenvalues of the matrix A are $\lambda_1 = 0$ and $\lambda_2 = -(\gamma_{-0} + \gamma_{0-})$, respectively. Consequently the eigenvector matrix and its inverse matrix are derived as $P = \left(\begin{smallmatrix} \gamma_{0-} & 1 \\ \gamma_{-0} & -1 \end{smallmatrix}\right)$

and $P^{-1} = \frac{1}{\gamma_{-0}+\gamma_{0-}} \begin{pmatrix} 1 & 1 \\ \gamma_{0-} & -\gamma_{-0} \end{pmatrix}$, respectively. Therefore $p(t)$ will be:

$$\begin{aligned} p(t) = \begin{pmatrix} p_-(t) \\ p_0(t) \end{pmatrix} &= \frac{1}{\gamma_{-0}+\gamma_{0-}} \begin{pmatrix} \gamma_{0-} & 1 \\ \gamma_{-0} & -1 \end{pmatrix} \begin{pmatrix} 0 & 0 \\ 0 & \mathrm{e}^{-(\gamma_{-0}+\gamma_{0-})t} \end{pmatrix} \begin{pmatrix} 1 & 1 \\ \gamma_{0-} & -\gamma_{-0} \end{pmatrix} \begin{pmatrix} p_-(0) \\ p_0(0) \end{pmatrix} \\ &= \frac{p_-(0)+p_0(0)}{\gamma_{-0}+\gamma_{0-}} \left\{ \begin{pmatrix} \gamma_{0-} \\ \gamma_{-0} \end{pmatrix} + \begin{pmatrix} 1 \\ -1 \end{pmatrix} \{p_-(0)\gamma_{-0} - p_0(0)\gamma_{0-}\} \mathrm{e}^{-(\gamma_{-0}+\gamma_{0-})t} \right\}. \end{aligned} \tag{C.6}$$

From the rate equation (2.9), followings are apparently satisfied.

$$\frac{d}{dt}\{p_-(t)+p_0(t)\} = -\gamma_{-0}p_-(t) + \gamma_{0-}p_0(t) + \gamma_{-0}p_-(t) - \gamma_{0-}p_0(t) = 0, \tag{C.7a}$$

$$\frac{d}{dt}\{p_-(t)-p_0(t)\} = -\left(\gamma_{-0}+\gamma_{0-}\right)\{p_-(t)-p_0(t)\}. = \left(\gamma_{-0}+\gamma_{0-}\right)\{p_-(t)+p_0(t)\} \tag{C.7b}$$

If $\left(\begin{smallmatrix} p_- \\ p_0 \end{smallmatrix}\right) \propto \left(\begin{smallmatrix} \gamma_{0-} \\ \gamma_{-0} \end{smallmatrix}\right)$, then $\frac{d}{dt}\left(\begin{smallmatrix} p_- \\ p_0 \end{smallmatrix}\right) = 0$. This solution corresponds to the case $\lambda_1 = 0$. Normalizing as $p_-(t) + p_0(t) = 1$, I obtain the steady state shown in equation (2.11). If the states $\left(\begin{smallmatrix} p_- \\ p_0 \end{smallmatrix}\right)$ are not steady, the states are approaching by the time constant $(\gamma_{-0}+\gamma_{0-})$ in terms of the mode of $\{p_-(t)-p_0(t)\}$.

D. Additional data for the *p-i-n* diamond diode

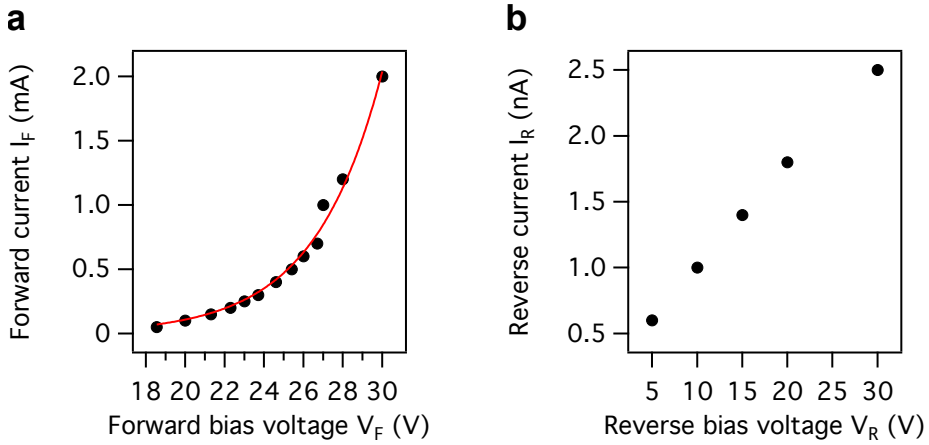

Figure D.1.: *I-V* properties of the *p-i-n* diamond diode. **a,** Forward bias voltage dependence of forward current I_F. A solid red curve is fitting by a function $I_F = I_0 \{\exp(V_F/V_T) - 1\}$. **b,** Reverse bias voltage dependence of reverse current I_R.

***I-V* properties of the *p-i-n* diode** Figures D.1a,b are I-V curves of the p-i-n diode when it is forward and reverse biased, respectively. Measurements were performed under continuous wave (cw) voltage applying. A solid red carve in I_F-V_F is a fitting by $I_F = I_0 \{\exp(V_F/V_T) - 1\}$. Saturation current I_0 is derived to $0.3 \pm 0.1\,\mu\mathrm{A}$. Thermal voltage V_T has extraordinary large value of $V_T = 3.4 \pm 0.1\,\mathrm{V}$ compared with p-i-n junction made by other materials ($V_T = \sim 26\,\mathrm{mV}$). This is thought to be due to a large junction resistance of the p-i-n diode.

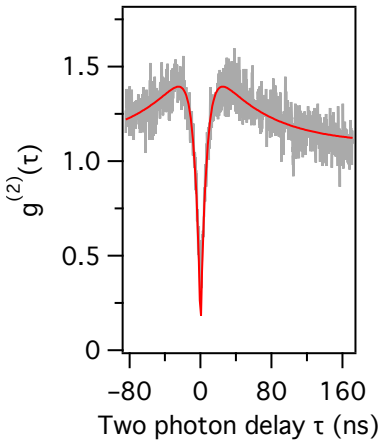

Figure D.2.: Autocorrelation measurement on the single NV in the *p-i-n* diamond diode. Characteristic dip at $\tau = 0$ indicate the single NV in the main text is a single photon emitter.

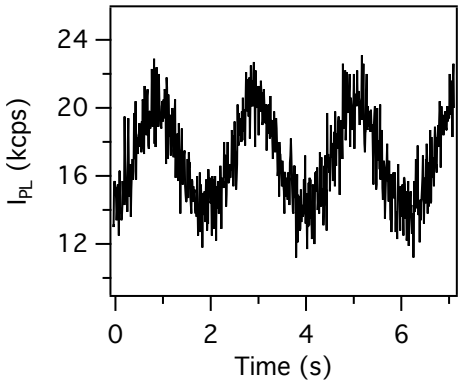

Figure D.3.: Charge state switching with sin-wave current. Real time-trace of I_{PL} with sin-wave current injection. Charge state follow current and is continuously modulated.

Autocorrelation measurement on a single NV Figure D.2 is a second-order autocorrelation function ($g^{(2)}(\tau)$) of a single NV in the *p-i-n* diode. It reveals an anti-bunching dip of < 0.5 at $\tau = 0$ indicating that the NV center in the main text is indeed a single one.

Sin-like switching of charge state Charge state population of NVs in *p-i-n* diode can be modulated by arbitrary shape of current wave. Figure D.3 is one of the example, monitoring of fluorescence intensity under sin wave of current.

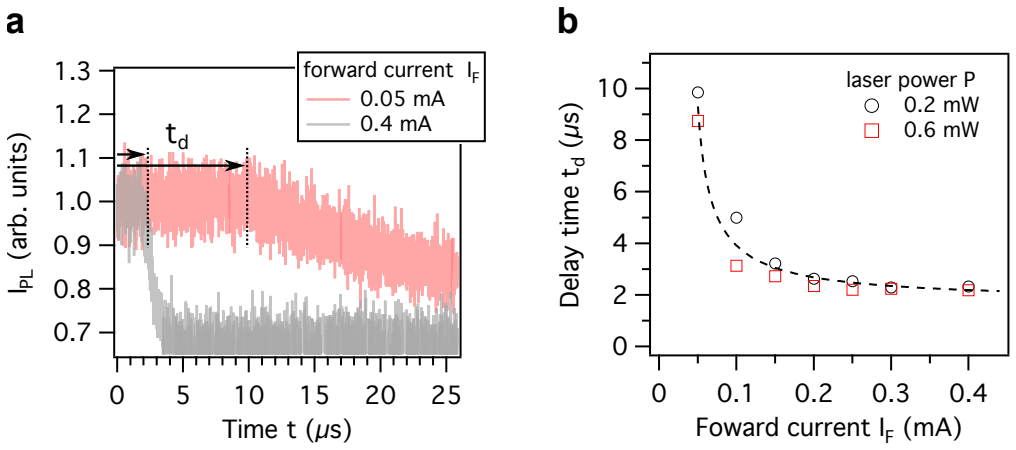

Figure D.4.: Forward current dependence of delay time. a, Delay time in the I_{PL} measurement on the *p-i-n* diode with different forward current I_F. Delay time t_d becomes longer with decrease of forward current. Laser power is fixed to 0.2 mW during the measurement in the panel. **b,** Forward current I_F and delay time t_d. Saturation behavior of t_d can be seen at $I_F \geq 0.2\,\mathrm{mA}$. A dashed carve is a fitting by using equation (D.3).

Delay time in the charge-state transition A delay time (t_d) is observed in the charge-state switching in the *p-i-n* diode, for example in figures 4.5–4.6a,b. This delay time t_d depends on the amplitude of forward current, is shown in figures D.4a,b. Figure D.4a is a transition of I_{PL} under $I_F = 0.05\,\mathrm{mA}$ and $I_F = 0.4\,\mathrm{mA}$. At a lower current, charge-state transition begins at $t_d = \sim 10\,\mu\mathrm{s}$ after diode is turned on. Under the higher current (0.4 mA), t_d becomes 2 µs, 5 times shorter than lower current injection. In the current range from 0.05 to 0.4 mA, forward current dependence of delay time is shown in figure D.4b. From 0.2 to 0.4 mA, the delay time show saturation behavior. Transition rate measurements in the main text is performed within the range.

Modeling delay time This paragraph is about modeling of delay time with considering transient response of the equivalent circuit of the *p-i-n* diode and threshold current for charge state transition.

First, at the simplified situation, *p-i-n* diode is represented as LR-series circuit under forward biased [107]. In the LR-series circuit, transient response of forward current until it reaches to steady current I_F, is written as follows with time constant of circuit $\tau_{circ} = \frac{L}{R}$ [115]:

$$i_F(t) = I_F \left\{ 1 - \exp\left(-\frac{t}{\tau_{circ}} \right) \right\}. \tag{D.1}$$

Second, threshold current of charge-state transition (I_{th}) must be considered. If there is no threshold, I_{PL} (and charge state) should immediately responses to forward current

when diode is switched from off- to on-state. However, I_{PL} does not immediately response at turn on-state of p-i-n diode. Here I_{th} is written as follows at $t = t_{th}$:

$$I_{th} = I_F \left\{ 1 - \exp\left(-\frac{t_{th}}{\tau_{circ}} \right) \right\}, \tag{D.2a}$$

then,

$$t_{th} = \tau_{circ} \ln\left(\frac{I_F}{I_F - I_{th}} \right). \tag{D.2b}$$

Third, when a p-i-n diode is forward biased, holes from the p-type layer and electrons from the n-type layer are injected into the i-layer, where the NV resides. Injected carries are recombined with the finite amount of time. This time is called the carrier lifetime and mentioned in the main text (See equation (4.6)). It is thought that the recombination of NV and a hole also requires same order of time because statistics of recombination at NV discussed in the currently available model takes into account carrier lifetime [24]. Thereby carrier lifetime should be considered in t_d as t_{offset}.

Finally, a delay time is expressed as follows:

$$t_d = t_{\text{offset}} + t_{th} = t_{\text{offset}} + \tau_{circ} \ln\left(\frac{I_F}{I_F - I_{th}} \right). \tag{D.3}$$

Curve fitting were performed to determine 3 parameters in the function. As a result, $t_{\text{offset}} = 1.8 \pm 0.3\,\mu\text{s}$, $\tau_{circ} = 3.8 \pm 1.4\,\mu\text{s}$, and $I_{th} = 43.0 \pm 0.4\,\mu\text{A}$ are obtained. The fitting results is shown in figure D.4b as a dashed carve. It is good agreement with measurement results. The offset t_{offset} is close to the carrier lifetime in diamond, $2.3\,\mu\text{s}$ [105]. Time constant of equivalent circuit τ_{circ} also has same order of magnitude as a time response of electroluminescence (EL) mentioned in the next paragraph. If above assumption is reasonable, threshold current exists in charge state transition and it might relates to interaction between injected carriers and NVs in the p-i-n diode.

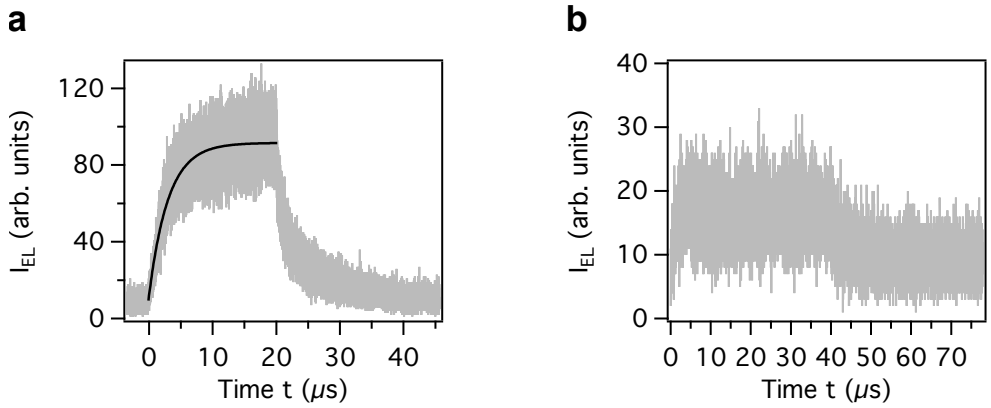

Figure D.5.: Time resolved measurement of electroluminescence from a single NV. a Electroluminescence (EL) under 2 mA current injection is resolved by the fluorescence averaging measurement. The on-state transition is fitted by a single exponential function with time constant of 3.03 µs. **b,** EL from a single NV (or from *i*-layer) appears in the measurement of fluorescence averaging measurement ($I_F = 0.5\,\mathrm{mA}$). No delay time exists in time resolved measurement of EL.

Time resolved measurement of electroluminescence from a single NV or/and *i*-layer Time-resolved averaging measurement of electroluminescence intensity (I_{EL}) from single NV or/and *i*-layer has been performed. In the experimental condition, the origin of EL could not be identified because much larger amount of current ($I_F > 4\,\mathrm{mA}$), which can destroy the sample, is required to distinguish either fluorescence comes from an NV or diamond layer, or from both of them. Figure D.5a is a EL of a single NV under 2-mA current injection. The exponential transient response has been seen on the result. The time constant of transition is 3.03 µs. Figure D.5b is a EL appears in the fluorescence averaging measurement (FAM) in the main text, under 0.5 mA current injection. It is difficult to fit the result because of inadequate fluorescence intensity ($I_{EL} \simeq 1\,\mathrm{kcps}$).

Interestingly, differing from I_{PL} in charge state transition, I_{EL} immediately response to switching of the diode, without delay time. It implies that different mechanism of carrier dynamics are involving in EL and charge state transition in *p*-*i*-*n* diode.

E. Additional data for *n*-type diamond layers

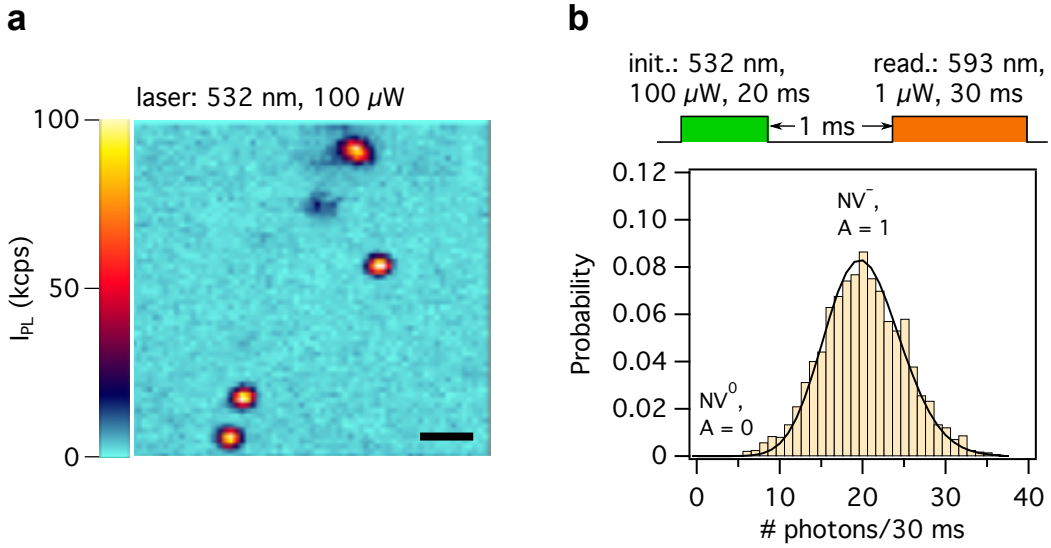

Figure E.1.: Raster scan image and single-shot charge-state measurement on an *n*-layer (h443). a, Scan image was taken under 532 nm, 100 µW excitation. Four single NVs are shown in this image. Scale bar, 1 µm. **b,** A result of single-shot charge-state measurement on a NV in h443 sample. All measured NVs in h443 are completely populated into NV^-.

Raster scan imaging and single-shot charge state detection on h443 sample Fluorescence dynamics of single NVs in h443 sample is not shown in the main text because enough number of experiments cannot be performed on the sample. Figure E.1a is a raster scan image of h443 sample ($[P] = 5 \times 10^{15}\,cm^{-3}$, see table 5.1) under 532 nm, 100 µW excitation. Bright spots are single NV center in a *n*-type layer. Distribution of NVs in the layer and fluorescence intensity of these NVs are almost same as intrinsic diamond (see figure 3.1b). However, a large difference appears in results of SCM as well as h578 sample. Figure E.1b is a result of SCM in h443 sample. All measured NVs (seven NVs) in the sample seems completely populated into NV^- charge state. After these measurements were carried out, ^{15}N ions are additionally implanted (10 keV, 600 °C) in the shallow region of h443 sample. Another isotope of nitrogen is used to

distinguish shallow NVs from deeply implanted one (consists of ^{14}N) by means of spin resonance spectroscopy. Shallow NVs are easily ionized to NV^- but phosphorus might be able to prevent ionization. Stable NV^- at shallower region of the bulk is important because they can sense small magnetic species at the outer of diamond [116–118].

Unfortunately, ion implantation of ^{15}N dramatically changed the charge state population of NVs in this sample because created defects probably compensated the electron carriers. As a result, only 2 of 16 NVs were pure negatively charged. Due to above situations of a h443 sample, investigations on this sample were halted and experiments were continued on another, h578 sample discussed in the main text.

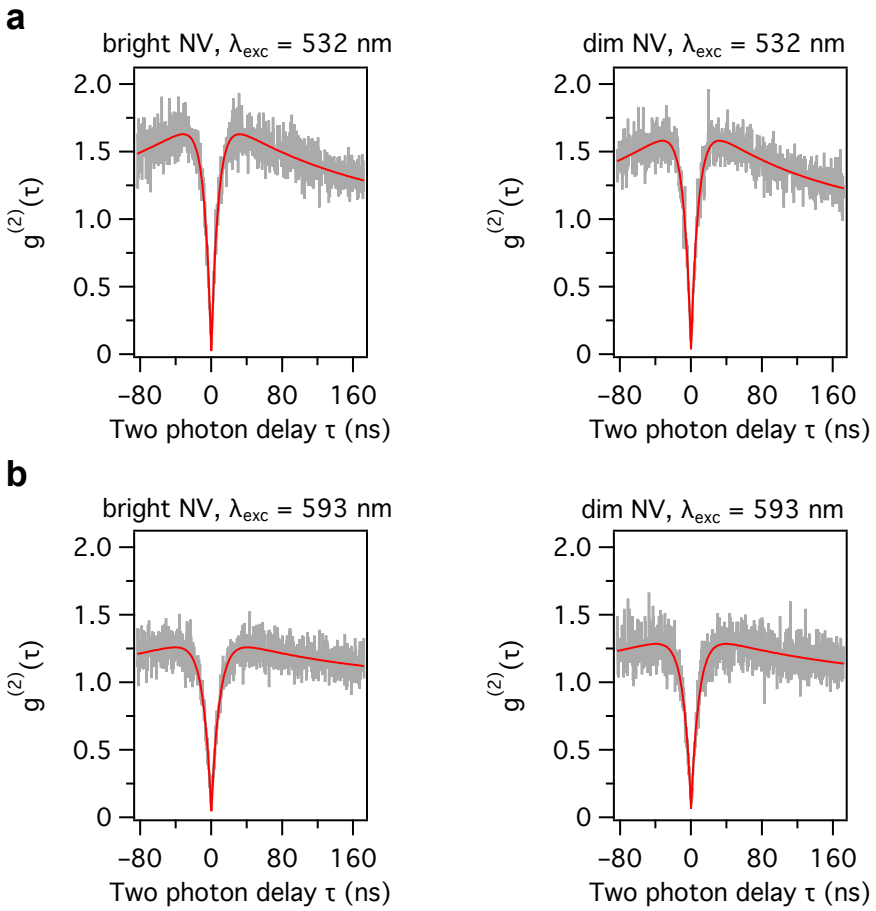

Figure E.2.: Autocorrelation measurement on the dim and bright NVs in an *n*-layer (h578). Second order autocorrelation measurements on bright (panel **a**) and dim NV (panel **b**) under 500 µW of green and orange excitation.

Autocorrelation measurement on the dim and bright NVs in an *n*-layer Figures E.2a,b are the $g^{(2)}(\tau)$ for bright and dim NVs in h578 n-type diamond layer under

green and orange laser excitation (500 µW). First the $g^{(2)}(\tau)$ of two NVs are below 0.5 at $\tau = 0$ indicating two NVs are single photon emitter. Second background fluorescence ($g^{(2)}(\tau)$ at $t = 0$) from both NVs are low. This fact that the background fluorescence of n-type layer is the same as that of intrinsic diamond. There are no significant differences in two NVs even different laser power. Thus it is difficult to discuss difference of dynamics from the measurement. However under lower power excitation, there are possibility that the difference appears.

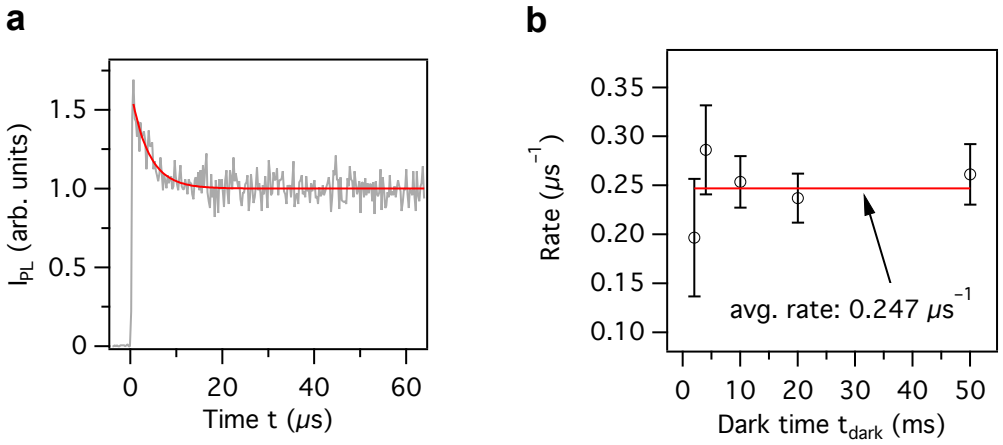

Figure E.3.: Transition rate during orange laser pulse and dark time, in figure 5.7a. a, Transition of I_{PL} at orange laser pulse ($P = 230\,\mu W$) after dark time $t_{dark} = 10\,ms$. **b,** Dark time dependence of transition rate of I_{PL}. Results are obtained by fitting in the panel **a** with various dark time.

Dark time and transition rate during orange excitation This explains that the dark time between initialization and readout pulse does not affect to transition rate during readout pulse. Figures E.3a,b are carve fitting results to pulses in the measurement for charge-state transition rate in the main text, figure E.2 ($\lambda_{exc} = 593\,nm$, $P = 230\,\mu W$). Single exponential decay of I_{PL} is observed in every pulse. Figure E.3b is dark time dependence of a transition rate obtained by a single exponential fitting in figure 5.7. The average rate (solid line in figure, $\gamma = 0.247\,\mu s^{-1}$) covers all data points include each error bar. To check average rate is reasonable or not, substitute $P = 230\,\mu W$ to equation (5.3), then calculate rate. Rate $\gamma_{bright} = 0.237\,\mu s^{-1}$ is obtained as a result. This value is almost same as average value of transition rates in figure E.3b.

Also in the rate measurement during excitation (figures 5.8b–c), transition rate during orange laser excitation do not depend on the dark time. Figures E.4a is a pulse sequence. During orange laser excitation ($P = 100\,\mu W$), transitions of I_{PL} are measured on $t_{dark} =$ 0.1 and 10 ms are shown in figure E.4b,c, respectively. There are no significant differences in the rate.

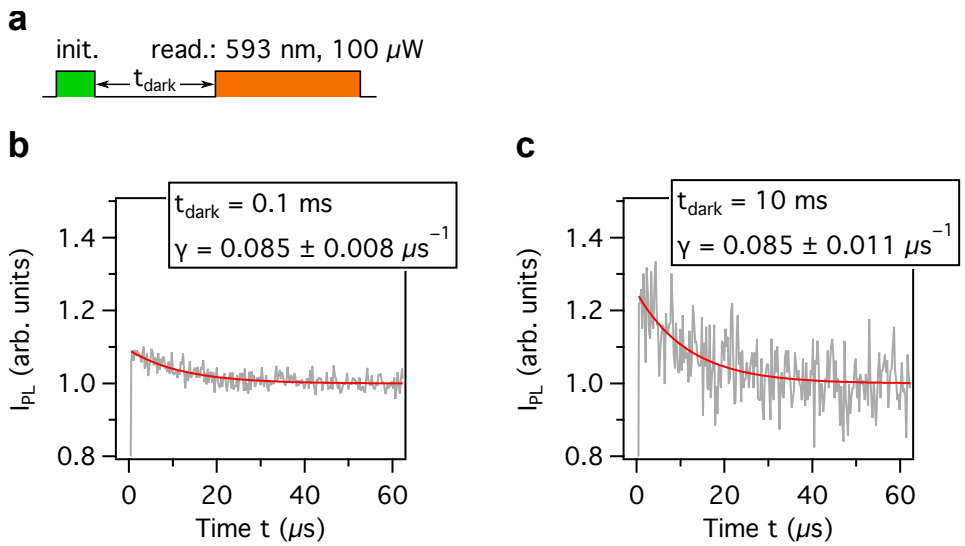

Figure E.4.: Transition rate during orange laser pulse and dark time, in figures 5.8a–d. a, Pulse sequence for the measurement. **b,** For $t_{\text{dark}} = 0.1\,\text{ms}$ **c,** For $t_{\text{dark}} = 10\,\text{ms}$.

Comparison of charge recovering during dark between dim and bright NV Figures E.5a–b is a comparison of recovery of p_- during dark condition between dim and bright NVs. With pulse sequence shown in figure E.5a, bright NV show recovery of p_- during dark time (figure E.5b) as mentioned in the main text. On the contrary to bright NV, dim NV does not show increase of I_{PL} at the initial of pulse is shown in figure E.5c.

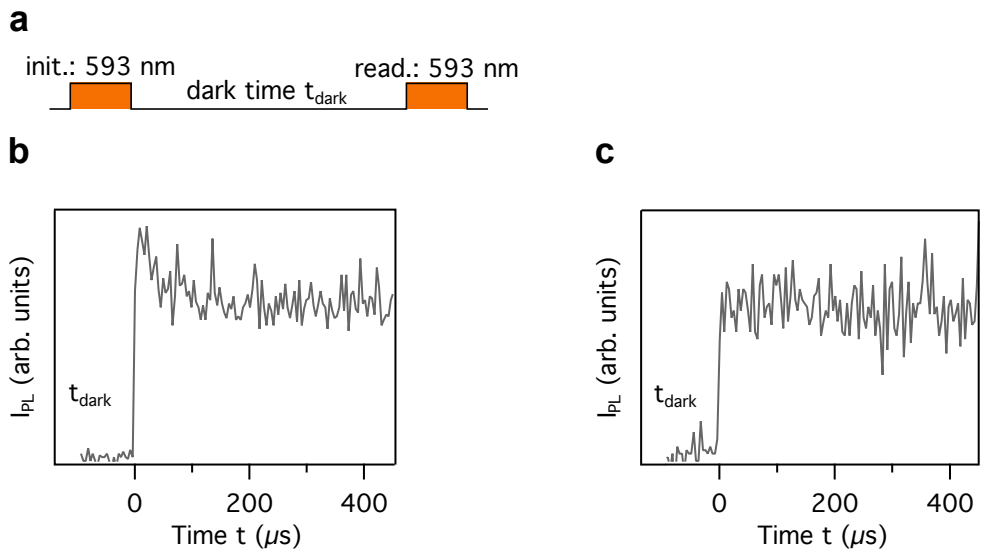

Figure E.5.: Charge state recovering during dark time. **a,** A typical measurement sequence to measure charge state recovery during the dark time t_{dark}. **b,** Fluorescence intensity I_{PL} of a bright NV detected after t_{dark}. **c,** Dim NV does not show charge state recovery after t_{dark}.

Bibliography

[1] D. Deutsch, *Quantum Theory, the Church-Turing Principle and the Universal Quantum Computer*, Proceedings of the Royal Society of London A: Mathematical, Physical and Engineering Sciences **400**, 97 (1985).

[2] D. Deutsch and R. Jozsa, *Rapid Solution of Problems by Quantum Computation*, Proceedings of the Royal Society of London A: Mathematical, Physical and Engineering Sciences **439**, 553 (1992).

[3] L. K. Grover, *A fast quantum mechanical algorithm for database search*, (1996), arXiv:quant-ph/9605043, URL: http://arxiv.org/abs/quant-ph/9605043.

[4] P. Shor, *Polynomial-Time Algorithms for Prime Factorization and Discrete Logarithms on a Quantum Computer*, SIAM Journal on Computing **26**, 1484 (1997).

[5] C. H. Bennett and G. Brassard, *Quantum cryptography: Public key distribution and coin tossing*, in Proceedings of the IEEE International Conference on Computers, Systems, and Signal Processing (1984), p. 175, URL: http://researcher.watson.ibm.com/researcher/files/us-bennetc/BB84highest.pdf.

[6] N. Gisin and R. Thew, *Quantum communication*, Nature Photonics **1**, 165 (2007).

[7] C. L. Degen, *Nanoscale magnetometry: Microscopy with single spins*, Nature Nanotechnology **3**, 643 (2008).

[8] R. P. Feynman, *Simulating physics with computers*, International Journal of Theoretical Physics **21**, 467 (1982).

[9] E. Knill, R. Laflamme, and G. J. Milburn, *A scheme for efficient quantum computation with linear optics*, Nature **409**, 46 (2001).

[10] J. L. O'Brien, *Optical Quantum Computing*, Science **318**, 1567 (2007).

[11] R. Blatt and D. Wineland, *Entangled states of trapped atomic ions*, Nature **453**, 1008 (2008).

[12] J. P. Home, D. Hanneke, J. D. Jost, J. M. Amini, D. Leibfried, and D. J. Wineland, *Complete Methods Set for Scalable Ion Trap Quantum Information Processing*, Science **325**, 1227 (2009).

[13] D. G. Cory, A. F. Fahmy, and T. F. Havel, *Ensemble quantum computing by NMR spectroscopy*, Proceedings of the National Academy of Sciences **94**, 1634 (1997), URL: http://www.pnas.org/content/94/5/1634.

[14] C. Negrevergne, T. S. Mahesh, C. A. Ryan, M. Ditty, F. Cyr-Racine, W. Power, N. Boulant, T. Havel, D. G. Cory, and R. Laflamme, *Benchmarking Quantum Control Methods on a 12-Qubit System*, Physical Review Letters **96**, 170501 (2006).

[15] M. Negoro, K. Tateishi, A. Kagawa, and M. Kitagawa, *Scalable Spin Amplification with a Gain Over a Hundred*, Physical Review Letters **107**, 050503 (2011).

[16] R. Hanson, L. P. Kouwenhoven, J. R. Petta, S. Tarucha, and L. M. K. Vandersypen, *Spins in few-electron quantum dots*, Reviews of Modern Physics **79**, 1217 (2007).

[17] D. Press, T. D. Ladd, B. Zhang, and Y. Yamamoto, *Complete quantum control of a single quantum dot spin using ultrafast optical pulses*, Nature **456**, 218 (2008).

[18] Y. Nakamura, Y. A. Pashkin, and J. S. Tsai, *Coherent control of macroscopic quantum states in a single-Cooper-pair box*, Nature **398**, 786 (1999).

[19] J. M. Martinis, S. Nam, J. Aumentado, and C. Urbina, *Rabi Oscillations in a Large Josephson-Junction Qubit*, Physical Review Letters **89**, 117901 (2002).

[20] L. DiCarlo, J. M. Chow, J. M. Gambetta, L. S. Bishop, B. R. Johnson, D. I. Schuster, J. Majer, A. Blais, L. Frunzio, S. M. Girvin, and R. J. Schoelkopf, *Demonstration of two-qubit algorithms with a superconducting quantum processor*, Nature **460**, 240 (2009).

[21] G. Balasubramanian, P. Neumann, D. Twitchen, M. Markham, R. Kolesov, N. Mizuochi, J. Isoya, J. Achard, J. Beck, J. Tissler, V. Jacques, P. R. Hemmer, F. Jelezko, and J. Wrachtrup, *Ultralong spin coherence time in isotopically engineered diamond*, Nature Materials **8**, 383 (2009).

[22] H. Bernien, B. Hensen, W. Pfaff, G. Koolstra, M. S. Blok, L. Robledo, T. H. Taminiau, M. Markham, D. J. Twitchen, L. Childress, and R. Hanson, *Heralded entanglement between solid-state qubits separated by three metres*, Nature **497**, 86 (2013).

[23] P. C. Maurer, G. Kucsko, C. Latta, L. Jiang, N. Y. Yao, S. D. Bennett, F. Pastawski, D. Hunger, N. Chisholm, M. Markham, D. J. Twitchen, J. I. Cirac, and M. D. Lukin, *Room-Temperature Quantum Bit Memory Exceeding One Second*, Science **336**, 1283 (2012).

[24] N. Mizuochi, T. Makino, H. Kato, D. Takeuchi, M. Ogura, H. Okushi, M. Nothaft, P. Neumann, A. Gali, F. Jelezko, J. Wrachtrup, and S. Yamasaki, *Electrically*

driven single-photon source at room temperature in diamond, Nature Photonics **6**, 299 (2012).

[25] A. Lohrmann, S. Pezzagna, I. Dobrinets, P. Spinicelli, V. Jacques, J.-F. Roch, J. Meijer, and A. M. Zaitsev, *Diamond based light-emitting diode for visible single-photon emission at room temperature*, Applied Physics Letters **99**, 251106 (2011).

[26] H. Kato, M. Wolfer, C. Schreyvogel, M. Kunzer, W. Müller-Sebert, H. Obloh, S. Yamasaki, and C. Nebel, *Tunable light emission from nitrogen-vacancy centers in single crystal diamond PIN diodes*, Applied Physics Letters **102**, 151101 (2013).

[27] K. Groot-Berning, N. Raatz, I. Dobrinets, M. Lesik, P. Spinicelli, A. Tallaire, J. Achard, V. Jacques, J.-F. Roch, A. M. Zaitsev, J. Meijer, and S. Pezzagna, *Passive charge state control of nitrogen-vacancy centres in diamond using phosphorous and boron doping*, physica status solidi (a) **211**, 2268 (2014).

[28] G. Waldherr, J. Beck, M. Steiner, P. Neumann, A. Gali, T. Frauenheim, F. Jelezko, and J. Wrachtrup, *Dark States of Single Nitrogen-Vacancy Centers in Diamond Unraveled by Single Shot NMR*, Physical Review Letters **106**, 157601 (2011).

[29] P. Siyushev, H. Pinto, M. Vörös, A. Gali, F. Jelezko, and J. Wrachtrup, *Optically Controlled Switching of the Charge State of a Single Nitrogen-Vacancy Center in Diamond at Cryogenic Temperatures*, Physical Review Letters **110**, 167402 (2013).

[30] K.-M. C. Fu, C. Santori, P. E. Barclay, and R. G. Beausoleil, *Conversion of neutral nitrogen-vacancy centers to negatively charged nitrogen-vacancy centers through selective oxidation*, Applied Physics Letters **96**, 121907 (2010).

[31] C. Bradac, T. Gaebel, N. Naidoo, M. J. Sellars, J. Twamley, L. J. Brown, A. S. Barnard, T. Plakhotnik, A. V. Zvyagin, and J. R. Rabeau, *Observation and control of blinking nitrogen-vacancy centres in discrete nanodiamonds*, Nature Nanotechnology **5**, 345 (2010).

[32] M. V. Hauf, B. Grotz, B. Naydenov, M. Dankerl, S. Pezzagna, J. Meijer, F. Jelezko, J. Wrachtrup, M. Stutzmann, F. Reinhard, and J. A. Garrido, *Chemical control of the charge state of nitrogen-vacancy centers in diamond*, Physical Review B **83**, 081304 (2011).

[33] T. W. Shanley, A. A. Martin, I. Aharonovich, and M. Toth, *Localized chemical switching of the charge state of nitrogen-vacancy luminescence centers in diamond*, Applied Physics Letters **105**, 063103 (2014).

[34] M. M. Shukla and N. T. Padial, *A calculation of the Debye characteristic temperature of cubic crystals*, Revista Brasileira de Física **3**, 39 (1973), URL: `http://www.sbfisica.org.br/bjp/download/v03/v03a03.pdf`.

[35] S. Koizumi, ed., *Physics and applications of CVD diamond* (Wiley-VCH-Verl, Weinheim, 2008), ISBN: 978-3-527-40801-6.

[36] S. M. Sze and K. K. Ng, *Physics of Semiconductor Devices* (John Wiley & Sons, New York, 2006).

[37] C. M. Breeding and J. E. Shigley, *The "type" classification system of diamonds and its importance in gemology*, Gems and Gemology **45**, 96 (2009).

[38] I. Aharonovich, S. Castelletto, C.-H. Su, A. D. Greentree, and S. Prawer, *Diamond-based single-photon emitters*, Reports on Progress in Physics **74**, 076501 (2011).

[39] R. G. Farrer, *On The Substitutional Nitrogen Donor In Diamond*, Solid State Communications **7**, 685 (1969).

[40] V. K. Sarin, ed., *Comprehensive hard materials* (Elsevier, Amsterdam, 2014), ISBN: 978-0-08-096527-7.

[41] I. Stenger, M.-A. Pinault-Thaury, T. Kociniewski, A. Lusson, E. Chikoidze, F. Jomard, Y. Dumont, J. Chevallier, and J. Barjon, *Impurity-to-band activation energy in phosphorus doped diamond*, Journal of Applied Physics **114**, 073711 (2013).

[42] J. Blakemore, *Semiconductor statistics* (Dover Publications, New York, 1987), ISBN: 978-0-486-49502-6.

[43] E. Gheeraert, N. Casanova, S. Koizumi, T. Teraji, and H. Kanda, *Low temperature excitation spectrum of phosphorus in diamond*, Diamond and Related Materials **10**, 444 (2001).

[44] W. Gajewski, P. Achatz, O. A. Williams, K. Haenen, E. Bustarret, M. Stutzmann, and J. A. Garrido, *Electronic and optical properties of boron-doped nanocrystalline diamond films*, Physical Review B **79**, 045206 (2009).

[45] E. Gheeraert, S. Koizumi, T. Teraji, H. Kanda, and M. Nesládek, *Electronic States of Boron and Phosphorus in Diamond*, physica status solidi (a) **174**, 39 (1999).

[46] A. H. Lettington and J. W. Steeds, *Thin film diamond* (Springer, Dordrecht, 1994), ISBN: 978-94-010-4312-0, URL: http://dx.doi.org/10.1007/978-94-011-0725-9.

[47] M. Katagiri, J. Isoya, S. Koizumi, and H. Kanda, *Lightly phosphorus-doped homoepitaxial diamond films grown by chemical vapor deposition*, Applied Physics Letters **85**, 6365 (2004).

[48] S. Koizumi, M. Kamo, Y. Sato, H. Ozaki, and T. Inuzuka, *Growth and characterization of phosphorous doped {111} homoepitaxial diamond thin films*, Applied Physics Letters **71**, 1065 (1997).

[49] S. Koizumi, M. Kamo, Y. Sato, S. Mita, A. Sawabe, A. Reznik, C. Uzan-Saguy, and R. Kalish, *Growth and characterization of phosphorus doped n-type diamond thin films*, Diamond and Related Materials **7**, 540 (1998).

[50] S. Curat, H. Ye, O. Gaudin, R. B. Jackman, and S. Koizumi, *An impedance spectroscopic study of n-type phosphorus-doped diamond*, Journal of Applied Physics **98**, 073701 (2005).

[51] M. Nesládek, K. Meykens, K. Haenen, L. M. Stals, T. Teraji, and S. Koizumi, *Low-temperature spectroscopic study of* n*-type diamond*, Physical Review B **59**, 14852 (1999).

[52] H. Kato, S. Yamasaki, and H. Okushi, *n-type doping of (001)-oriented single-crystalline diamond by phosphorus*, Applied Physics Letters **86**, 222111 (2005).

[53] H. Sternschulte, K. Thonke, R. Sauer, and S. Koizumi, *Optical evidence for 630-meV phosphorus donor in synthetic diamond*, Physical Review B **59**, 12924 (1999).

[54] A. T. Collins and A. W. S. Williams, *The nature of the acceptor centre in semiconducting diamond*, Journal of Physics C: Solid State Physics **4**, 1789 (1971).

[55] J.-P. Lagrange, A. Deneuville, and E. Gheeraert, *Activation energy in low compensated homoepitaxial boron-doped diamond films*, Diamond and Related Materials **7**, 1390 (1998).

[56] I. Vlasov, V. Ralchenko, A. Khomich, S. Nistor, D. Shoemaker, and R. Khmelnitskii, *Relative Abundance of Single and Vacancy-Bonded Substitutional Nitrogen in CVD Diamond*, physica status solidi (a) **181**, 83 (2000).

[57] J. Meijer, B. Burchard, M. Domhan, C. Wittmann, T. Gaebel, I. Popa, F. Jelezko, and J. Wrachtrup, *Generation of single color centers by focused nitrogen implantation*, Applied Physics Letters **87**, 261909 (2005).

[58] J. P. Goss, R. Jones, P. R. Briddon, G. Davies, A. T. Collins, A. Mainwood, J. A. van Wyk, J. M. Baker, M. E. Newton, A. M. Stoneham, and S. C. Lawson, *Comment on "Electronic structure of the N-V center in diamond: Theory"*, Physical Review B **56**, 16031 (1997).

[59] J. R. Weber, W. F. Koehl, J. B. Varley, A. Janotti, B. B. Buckley, C. G. Van de Walle, and D. D. Awschalom, *Quantum computing with defects*, Proceedings of the National Academy of Sciences of the United States of America **107**, 8513 (2010).

[60] B. Grotz, M. V. Hauf, M. Dankerl, B. Naydenov, S. Pezzagna, J. Meijer, F. Jelezko, J. Wrachtrup, M. Stutzmann, F. Reinhard, and J. A. Garrido, *Charge state manipulation of qubits in diamond*, Nature Communications **3**, 729 (2012).

[61] G. Davies, *Dynamic Jahn-Teller distortions at trigonal optical centres in diamond*, Journal of Physics C: Solid State Physics **12**, 2551 (1979).

[62] S. Felton, A. Edmonds, M. Newton, P. Martineau, D. Fisher, and D. J. Twitchen, *Electron paramagnetic resonance studies of the neutral nitrogen vacancy in diamond*, Physical Review B **77**, 081201 (2008).

[63] G. Liaugaudas, G. Davies, and K. Suhling, *Luminescence lifetimes of neutral nitrogen-vacancy centres in synthetic diamond containing nitrogen*, Journal of Physics: Condensed Matter **24**, 435503 (2012).

[64] N. B. Manson, K. Beha, A. Batalov, L. J. Rogers, M. W. Doherty, R. Bratschitsch, and A. Leitenstorfer, *Assignment of the NV^0 575-nm zero-phonon line in diamond to a ^{2}e-^{2}a$_2$ transition*, Physical Review B **87**, 155209 (2013).

[65] G. Davies and M. F. Hamer, *Optical Studies of the 1.945 eV Vibronic Band in Diamond*, Proceedings of the Royal Society A: Mathematical, Physical and Engineering Sciences **348**, 285 (1976).

[66] N. B. Manson, J. Harrison, and M. Sellars, *Nitrogen-vacancy center in diamond: Model of the electronic structure and associated dynamics*, Physical Review B **74**, 104303 (2006).

[67] A. Gali, E. Janzén, P. Deák, G. Kresse, and E. Kaxiras, *Theory of Spin-Conserving Excitation of The N-V^- Center in Diamond*, Physical Review Letters **103**, 186404 (2009).

[68] V. M. Acosta, E. Bauch, M. P. Ledbetter, A. Waxman, L. S. Bouchard, and D. Budker, *Temperature Dependence of the Nitrogen-Vacancy Magnetic Resonance in Diamond*, Physical Review Letters **104**, 070801 (2010).

[69] A. Lenef and S. C. Rand, *Electronic structure of the N-V center in diamond: Theory*, Physical Review B **53**, 13441 (1996).

[70] P. Deák, B. Aradi, M. Kaviani, T. Frauenheim, and A. Gali, *Formation of NV centers in diamond: A theoretical study based on calculated transitions and migration of nitrogen and vacancy related defects*, Physical Review B **89**, 075203 (2014).

[71] N. Aslam, G. Waldherr, P. Neumann, F. Jelezko, and J. Wrachtrup, *Photo-induced ionization dynamics of the nitrogen vacancy defect in diamond investigated by single-shot charge state detection*, New Journal of Physics **15**, 013064 (2013).

[72] J. P. Goss, P. R. Briddon, M. J. Rayson, S. J. Sque, and R. Jones, *Vacancy-impurity complexes and limitations for implantation doping of diamond*, Physical Review B **72**, 035214 (2005).

[73] A. T. Collins, *The Fermi level in diamond*, Journal of Physics: Condensed Matter **14**, 3743 (2002).

[74] A. Wotherspoon, J. W. Steeds, B. Catmull, and J. Butler, *Photoluminescence and positron annihilation measurements of nitrogen doped CVD diamond*, Diamond and Related Materials, 13th European Conference on Diamond, Diamond-Like Materials, Carbon Nanotubes, Nitrides and Silicon Carbide **12**, 652 (2003).

[75] J. H. N. Loubser and J. A. van Wyk, *Electron spin resonance in the study of diamond*, Reports on Progress in Physics **41**, 1201 (1978).

[76] V. M. Acosta, *Optical Magnetometry with Nitrogen-Vacancy Centers in Diamond* (University of California, Berkeley, 2011), URL: http://escholarship.org/uc/item/1rj4p2ch.

[77] M. W. Doherty, N. B. Manson, P. Delaney, F. Jelezko, J. Wrachtrup, and L. C. L. Hollenberg, *The nitrogen-vacancy colour centre in diamond*, Physics Reports **528**, 1 (2013).

[78] F. Jelezko, T. Gaebel, I. Popa, M. Domhan, A. Gruber, and J. Wrachtrup, *Observation of Coherent Oscillation of a Single Nuclear Spin and Realization of a Two-Qubit Conditional Quantum Gate*, Physical Review Letters **93**, 130501 (2004).

[79] B. Smeltzer, L. Childress, and A. Gali, ^{13}C *hyperfine interactions in the nitrogen-vacancy centre in diamond*, New Journal of Physics **13**, 025021 (2011).

[80] A. Gruber, A. Dräbenstedt, C. Tietz, L. Fleury, J. Wrachtrup, and C. Von Borczyskowski, *Scanning Confocal Optical Microscopy and Magnetic Resonance on Single Defect Centers*, Science **276**, 2012 (1997).

[81] S. Felton, A. M. Edmonds, M. E. Newton, P. M. Martineau, D. Fisher, D. J. Twitchen, and J. M. Baker, *Hyperfine interaction in the ground state of the negatively charged nitrogen vacancy center in diamond*, Physical Review B **79**, 075203 (2009).

[82] *CODATA Value: Bohr magneton*, URL: http://physics.nist.gov/cgi-bin/cuu/Value?mub (visited on 02/23/2016).

[83] B. Smeltzer, J. McIntyre, and L. Childress, *Robust control of individual nuclear spins in diamond*, Physical Review A **80**, 050302 (2009).

[84] M. Steiner, P. Neumann, J. Beck, F. Jelezko, and J. Wrachtrup, *Universal enhancement of the optical readout fidelity of single electron spins at nitrogen-vacancy centers in diamond*, Physical Review B **81**, 035205 (2010).

[85] *CODATA Value: nuclear magneton*, URL: http://physics.nist.gov/cgi-bin/cuu/Value?mun%7Csearch_for=magneton (visited on 02/23/2016).

[86] D. A. Redman, S. Brown, R. H. Sands, and S. C. Rand, *Spin dynamics and electronic states of N-V centers in diamond by EPR and four-wave-mixing spectroscopy*, Physical Review Letters **67**, 3420 (1991).

[87] H.-J. Wang, C. S. Shin, S. J. Seltzer, C. E. Avalos, A. Pines, and V. S. Bajaj, *Optically detected cross-relaxation spectroscopy of electron spins in diamond*, Nature Communications **5**, 4135 (2014).

[88] A. Gali, *Theory of the neutral nitrogen-vacancy center in diamond and its application to the realization of a qubit*, Physical Review B **79**, 235210 (2009).

[89] W. Happer and A. C. Tam, *Effect of rapid spin exchange on the magnetic-resonance spectrum of alkali vapors*, Physical Review A **16**, 1877 (1977).

[90] C. P. Slichter, *Principles of magnetic resonance*, 3rd enl. and updated ed (Springer, Berlin ; New York, 1996), ISBN: 978-3-540-50157-2.

[91] L. Jiang, M. V. G. Dutt, E. Togan, L. Childress, P. Cappellaro, J. M. Taylor, and M. D. Lukin, *Coherence of an Optically Illuminated Single Nuclear Spin Qubit*, Physical Review Letters **100**, 073001 (2008).

[92] J. J. Macklin, J. K. Trautman, T. D. Harris, and L. E. Brus, *Imaging and Time-Resolved Spectroscopy of Single Molecules at an Interface*, Science **272**, 255 (1996).

[93] R. W. Cole, T. Jinadasa, and C. M. Brown, *Measuring and interpreting point spread functions to determine confocal microscope resolution and ensure quality control*, Nature Protocol **6**, 1929 (2011).

[94] S. Wilhelm, B. Gröbler, M. Gluch, and H. Heinz, *Confocal laser scanning microscopy principles* (Carl Zeiss Jena, Jena, 2003), URL: http://zeiss-campus.magnet.fsu.edu/referencelibrary/pdfs/ZeissConfocalPrinciples.pdf.

[95] C. Kurtsiefer, S. Mayer, P. Zarda, and H. Weinfurter, *Stable Solid-State Source of Single Photons*, Physical Review Letters **85**, 290 (2000).

[96] E. Neu, D. Steinmetz, J. Riedrich-Möller, S. Gsell, M. Fischer, M. Schreck, and C. Becher, *Single photon emission from silicon-vacancy colour centres in chemical vapour deposition nano-diamonds on iridium*, New Journal of Physics **13**, 025012 (2011).

[97] C. Wang, C. Kurtsiefer, H. Weinfurter, and B. Burchard, *Single photon emission from SiV centres in diamond produced by ion implantation*, Journal of Physics B: Atomic, Molecular and Optical Physics **39**, 37 (2006).

[98] A. T. Collins, M. F. Thomaz, and M. I. B. Jorge, *Luminescence decay time of the 1.945 eV centre in type Ib diamond*, Journal of Physics C: Solid State Physics **16**, 2177 (1983).

[99] A. Beveratos, R. Brouri, T. Gacoin, J.-P. Poizat, and P. Grangier, *Nonclassical radiation from diamond nanocrystals*, Physical Review A **64**, 061802 (2001).

[100] N. Mizuochi, P. Neumann, F. Rempp, J. Beck, V. Jacques, P. Siyushev, K. Nakamura, D. J. Twitchen, H. Watanabe, S. Yamasaki, F. Jelezko, and J. Wrachtrup, *Coherence of single spins coupled to a nuclear spin bath of varying density*, Physical Review B **80**, 041201 (2009).

[101] F. Jelezko, T. Gaebel, I. Popa, A. Gruber, and J. Wrachtrup, *Observation of Coherent Oscillations in a Single Electron Spin*, Physical Review Letters **92**, 076401 (2004).

[102] M. A. Nielsen and I. L. Chuang, *Quantum computation and quantum information* (Cambridge University Press, Cambridge ; New York, 2000), ISBN: 978-0-521-63235-5.

[103] A. G. Redfield, *Nuclear Magnetic Resonance Saturation and Rotary Saturation in Solids*, Physical Review **98**, 1787 (1955).

[104] T. Makino, K. Oyama, H. Kato, D. Takeuchi, M. Ogura, H. Okushi, and S. Yamasaki, *Diamond electronic devices fabricated using heavily doped hopping p^+ and n^+ layers*, Japanese Journal of Applied Physics **53**, 05FA12 (2014).

[105] A. Fujii, K. Takiyama, R. Maki, and T. Fujita, *Lifetime and quantum efficiency of luminescence due to indirect excitons in a diamond*, Journal of Luminescence **94**, 355 (2001).

[106] R. Palomera-Arias, *Pin diode switch circuit for short time high current pulse signal*, Thesis (Massachusetts Institute of Technology, 1998), URL: http://dspace.mit.edu/handle/1721.1/47505.

[107] W. E. Doherty, Jr. and R. D. Joos, *The PIN Diode Circuit Designers' Handbook* (Microsemi-Watertown, 1998), URL: http://www.ieee.li/pdf/essay/pin_diode_handbook.pdf.

[108] D. A. Neamen, *Semiconductor physics and devices: basic principles*, 4th ed (McGraw-Hill, New York, NY, 2012), ISBN: 978-0-07-352958-5.

[109] C. M. Bishop, *Pattern Recognition and Machine Learning* (Springer-Verlag, New York, 2006), ISBN: 978-0-387-31073-2.

[110] M. Nesladek, K. Meykens, K. Haenen, L. M. Stals, T. Teraji, and S. Koizumi, *Photocurrent and optical absorption spectroscopic study of n-type phosphorus-doped CVD diamond*, Diamond and Related Materials **8**, 882 (1999).

[111] K. Haenen, K. Meykens, M. Nesládek, G. Knuyt, C. Quaeyhaegens, L. M. Stals, S. Koizumi, and E. Gheeraert, *Low Temperature Photoconductivity Detection of Phosphorus in Diamond*, physica status solidi (a) **174**, 53 (1999).

[112] A. Dréau, M. Lesik, L. Rondin, P. Spinicelli, O. Arcizet, J.-F. Roch, and V. Jacques, *Avoiding power broadening in optically detected magnetic resonance of single NV defects for enhanced dc magnetic field sensitivity*, Physical Review B **84**, 195204 (2011).

[113] J. A. van Wyk, E. C. Reynhardt, G. L. High, and I. Kiflawi, *The dependences of ESR line widths and spin-spin relaxation times of single nitrogen defects on the concentration of nitrogen defects in diamond*, Journal of Physics D: Applied Physics **30**, 1790 (1997).

[114] N. Mizuochi, H. Watanabe, J. Isoya, H. Okushi, and S. Yamasaki, *Hydrogen-related defects in single crystalline CVD homoepitaxial diamond film studied by EPR*, Diamond and Related Materials **13**, 765 (2004).

[115] K. S. Suresh Kumar, *Electric circuits and networks* (Dorling Kindersley, New Delhi, 2009), ISBN: 978-81-317-1390-7.

[116] B. K. Ofori-Okai, S. Pezzagna, K. Chang, M. Loretz, R. Schirhagl, Y. Tao, B. A. Moores, K. Groot-Berning, J. Meijer, and C. L. Degen, *Spin properties of very shallow nitrogen vacancy defects in diamond*, Physical Review B **86**, 081406 (2012).

[117] C. Osterkamp, J. Lang, J. Scharpf, C. Müller, L. P. McGuinness, T. Diemant, R. J. Behm, B. Naydenov, and F. Jelezko, *Stabilizing shallow color centers in diamond created by nitrogen delta-doping using SF6 plasma treatment*, Applied Physics Letters **106**, 113109 (2015).

[118] Y. Romach, C. Müller, T. Unden, L. J. Rogers, T. Isoda, K. M. Itoh, M. Markham, A. Stacey, J. Meijer, S. Pezzagna, B. Naydenov, L. P. McGuinness, N. Bar-Gill, and F. Jelezko, *Spectroscopy of Surface-Induced Noise Using Shallow Spins in Diamond*, Physical Review Letters **114**, 017601 (2015).

Acknowledgments

First of all, I would like to thank my Ph.D. adviser Prof. Yoshishige Suzuki for giving me the opportunity of studying in Osaka university. I have learned a lot from him, such as how to conduct my research and scientific way of thinking. I would like to also appreciate Prof. Norikazu Mizuochi for his advises in my research. I was able to be involving in such a fascinating research field thanks to his guidance.

I would like to thank Dr. Shinji Miwa, for his kind advises in a lot of aspects of my research and life. I also appreciate to Dr. Hiroki Morishita and Dr. Toshiyuki Tashima for their supports in my experiments. The easy-to-use measurement platform help us to acquire measurement data and kindly helps in building a charge-state measurement system open the new way of my research.

I would like to appreciate to joint researchers in AIST, Dr. Toshiharu Makino, Dr. Hiromitsu Kato, Dr. Daisuke Takeuchi, Dr. Masahiko Ogura, Dr. Hideyo Okushi, and Dr. Satoshi Yamasaki. Always I was welcomed warmly when I visited there and could have fruitful discussions.

I would like to thank to Prof. Jörg Wrachtrup, Dr. Philipp Neumann, and Prof. Fedor Jelezko. Their comprehensive supports finally lead to two wonderful publications and I have great experiences and memories of visiting German.

I would like to thank to Prof. Eiichi Tamura for his kind helps especially in theory. His activities in the laboratory always cheer me up. I want to thank to Takaaki Shimo-Oka for his honest uncompromising advises for physics.

Finally, I would like to express my thanks to Ms. Yumi Oda, Ms. Rie Hasegawa, for their daily supports. I would like to thank all other members in Prof. Suzuki's group.

This work was supported by JSPS KAKENHI Grant Number 15J05801.

List of Publications

Journal Articles

1. Y. Doi, T. Fukui, H. Kato, T. Makino, S. Yamasaki, T. Tashima, H. Morishita, S. Miwa, F. Jelezko, Y. Suzuki, and N. Mizuochi, *Pure negatively charged state of the NV center in n-type diamond*, Physical Review B **93**, 081203 (February 3, 2016).

2. T. Iwasaki, F. Ishibashi, Y. Miyamoto, Y. Doi, S. Kobayashi, T. Miyazaki, K. Tahara, K. D. Jahnke, L. J. Rogers, B. Naydenov, F. Jelezko, S. Yamasaki, S. Nagamachi, T. Inubushi, N. Mizuochi and M. Hatano, *A Germanium-Vacancy Single Photon Source in Diamond*, Scientific Reports **5**, 12882 (August 7, 2015).

3. T. Miyazaki, R. Miyamoto, T. Makino, H. Kato, S. Yamasaki, T. Fukui, Y. Doi, N. Tokuda, M. Hatano, and N. Mizuochi, *Atomistic mechanism of perfect alignment of nitrogen-vacancy centers in diamond*, Applied Physics Letter **105**, 261601 (December 29, 2014).

4. T. Fukui, Y. Doi, T. Miyazaki, Y. Miyamoto, H. Kato, T. Matsumoto, T. Makino, S. Yamasaki, R. Morimoto, N. Tokuda, M. Hatano, Y. Sakagawa, H. Morishita, T. Tashima, S. Miwa, Y. Suzuki, and N. Mizuochi, *Perfect selective alignment of nitrogen-vacancy centers in diamond*, Applied Physics Express **7**, 055201 (April 9, 2014).

5. Y. Doi, T. Makino, H. Kato, D. Takeuchi, M. Ogura, H. Okushi, H. Morishita, T. Tashima, S. Miwa, S. Yamasaki, P. Neumann, J. Wrachtrup, Y. Suzuki, and N. Mizuochi, *Deterministic Electrical Charge-State Initialization of Single Nitrogen-Vacancy Center in Diamond*, Physical Review X **4**, 011057 (March 31, 2014).

List of Conference Presentations

Circles (∘) represent the speakers at conferences.

International Conferences

Oral Presentations

1. ∘T. Fukui, Y. Doi, T. Miyazaki, Y. Miyamoto, H. Kato, T. Matsumoto, T. Makino, S. Yamasaki, R. Morimoto, N. Tokuda, M. Hatano, H. Morishita, T. Tashima, S. Miwa, Y. Suzuki, and N. Mizuochi, *Perfect selective orientation of nitrogen vacancy centers in diamond*, APS March Meeting 2015, D37.00011, San Antonio, Texas, USA (March 2, 2015).

2. ∘T. Miyazaki, Y. Miyamoto, T. Makino, H. Kato, S. Yamasaki, T. Fukui, Y. Doi, N. Tokuda, M. Hatano, and N. Mizuochi, *Possible scenario of perfect alignment of nitrogen-vacancy centers in CVD diamond*, Hasselt Diamond Workshop 2015 SBDD XX, 12.1, Hasselt, Belgium (February 27, 2015).

3. ∘Y. Doi, T. Makino, H. Kato, D. Takeuchi, M. Ogura, H. Okushi, H. Morishita, T. Tashima, S. Miwa, S. Yamasaki, P. Neumann, J. Wrachtrup, Y. Suzuki, and N. Mizuochi, *Deterministic charge state control of single nitrogen vacancy center in diamond*, International Conference on Diamond and Carbon Materials, O4.1, Madrid, Spain (September 8, 2014).

4. ∘T. Fukui, Y. Doi, T. Miyazaki, Y. Miyamoto, H. Kato, T. Matsumoto, T. Makino, S. Yamasaki, R. Morimoto, N. Tokuda, M. Hatano, Y. Sakagawa, H. Morishita, T. Tashima, S. Miwa, Y. Suzuki, and N. Mizuochi, *Perfect alignment of the orientation of nitrogen-vacancy center in diamond*, The 15th IUMRS-International Conference in Asia (IUMRS-ICA 2014), C3-O25-008, Fukuoka, Japan (August 15, 2014).

5. ∘Y. Doi, T. Makino, H. Kato, D. Takeuchi, M. Ogura, H. Okushi, H. Morishita, T. Tashima, S. Miwa, S. Yamasaki, P. Neumann, J. Wrachtrup, Y. Suzuki, and N. Mizuochi, *Electrical charge state control of individual atomic defect in diamond*, PASPS-18, A-9, Osaka, Japan (December 9, 2013).

6. ∘Y. Doi, T. Makino, H. Kato, M. Ogura, D. Takeuchi, H. Okushi, S. Yamasaki, J. Wrachtrup, S. Miwa, Y. Suzuki, and N. Mizuochi, *Single Photon, Spin, and Charge in Diamond Semiconductor At Room Temperature*, CLEO-PR & OECC/PS 2013, MG1–3, Kyoto, Japan (July 1, 2013).

7. ∘N. Mizuochi, Y. Doi, T. Shimooka, S. Mori, T. Makino, H. Kato, D. Takeuchi, M. Ogura, H. Okushi, M. Nothaft, P. Neumann, A. Gali, F. Jelezko, J. Wrachtrup, S. Miwa, Y. Suzuki, and S. Yamasaki, *Electrically driven single photon source at room temperature in diamond*, International Conference on the Physics of Semiconductors the 31st ICPS 2012, 76.4, Zurich, Switzerland (August 3, 2012).

8. ∘N. Mizuochi, T. Shimooka, Y. Doi, S. Mori, T. Makino, H. Kato, D. Takeuchi, M. Ogura, H. Okushi, M. Nothaft, P. Neumann, A. Gali, F. Jelezko, J. Wrachtrup, S. Miwa, Y. Suzuki, and S. Yamasaki, *Control of single spins and single photons in diamond at room temperature*, The 2nd International Symposium on Electron Spin Science (ISESS 2012), O26, Sendai, Japan (July 25, 2012).

9. ∘S.-Y. Lee, Y. Doi, S. Mori, T. Shimooka, T. Rendler, N. Zhao, H. Fedder, S. Miwa, Y. Suzuki, N. Mizuochi, and J. Wrachtrup, *Coherent spin states of vacancy defects in silicon carbide*, der Deutschen Physikalischen Gesellschaft, HL 48.2, Berlin, German (March 28, 2012).

Poster Presentations

1. ∘Y. Sakagawa, H. Morishita, T. Tashima,T. Shimooka, Y. Doi, S. Yamasaki, H. Kato, S. Miwa, Y. Suzuki, and N. Mizuochi, *Toward observation of real-time dynamics of a nuclear spin in phosphorus doped n-type diamond*, QCrypt 2015, 96, Tokyo, Japan (September 29, 2015).

2. Y. Doi, T. Fukui, H. Kato, T. Makino, S. Yamasaki, ∘T. Tashima, H. Morishita, S. Miwa, F. Jelezko, Y. Suzuki, and N. Mizuochi, *Pure negatively charged state of NV center in n-type diamond*, Diamond Quantum Sensing Workshop 2015, P-22, Takamatsu, Japan (August 5, 2015).

3. T. Fukui, Y. Doi, T. Miyazaki, Y. Miyamoto, N. Tokuda, M. Hatano, Y. Sakagawa, Y. Suzuki, and ∘N. Mizuochi, *Perfect alignment of nitrogen-vacancy center in diamond*, International Conference on Diamond and Carbon Materials, P1.057, Madrid, Spain (September 8, 2014).

4. ∘Y. Doi, T. Makino, H. Kato, D. Takeuchi, M. Ogura, H. Okushi, H. Morishita, T. Tashima, S. Miwa, S. Yamasaki, P. Neumann, J. Wraptrup, Y. Suzuki, and N. Mizuochi, *Deterministic charge state control of single NV center in diamond with p-i-n diamond diode*, AQIS 2014, 40, Kyoto, Japan (August 21, 2014).

5. ○Y. Doi, T. Makino, H. Kato, M. Ogura, D. Takeuchi, H. Okushi, S. Yamasaki, J. Wrachtrup, S. Miwa, Y. Suzuki and N. Mizuochi, *Charge state manipulation of NV center in Diamond at Room Temperature*, 2013 JSAP-MRS Joint Symposia, 18p–PM3–1, Doshisha Univ., Kyoto, Japan (September 18, 2013).

6. ○Y. Doi, T. Makino, H. Kato, M. Ogura, D. Takeuchi, H. Okushi, S. Yamasaki, J. Wrachtrup, S. Miwa, Y. Suzuki, and N. Mizuochi, *Single Photon, Spin, and Charge in Diamond Semiconductor at Room Temperature*, Artificial Atoms: from Quantum Physics to Applications (The conference of the EU FP7–ICT DIAMANT Project (Diamond based atomic nanotechnologies) and the EU FP7 ITN CC-QED Project (Circuit and Cavity Quantum Electrodynamics)), Budapest, Hungary (May 20–23, 2013).

7. ○Y. Doi, T. Makino, H. Kato, M. Ogura, D. Takeuchi, H. Okushi, S. Yamasaki, J. Wrachtrup, S. Miwa, Y. Suzuki, and N. Mizuochi, *Single Photon, Spin, and Charge in Diamond Semiconductor at Room Temperature*, 8th Handai Nanoscience and Nanotechnology International Symposium, P2–10, Osaka, Japan (December 11, 2012).

8. ○Y. Doi, T. Makino, H. Kato, D. Takeuchi, M. Ogura, H. Okushi, M. Nothaft, A. Gali, F. Jelezko, J. Wrachtrup, S. Yamasaki, Y. Suzuki, and N. Mizuochi, *Single-Photon Emission from NV-center in Diamond by Current Injection*, The 38th Special Meeting of Special Session for Spin electronics, Magnetic Society in Japan, Osaka, Japan (January, 2012).

9. Y. Doi, ○C. Yoshikawa, M. Fujii, and S. Hayashi, *Fluorescence enhancement caused by Si and GaP particles*, The 5th International Conference on Surface Plasmon Photonics, MP-80, Busan, Korea, (May 15, 2011).

Domestic Conferences

1. ○村井拓哉, 牧野俊晴, 加藤宙光, 土井悠生, 鈴木義茂, 波多野睦子, 山崎聡, 水落憲和, 「nin 構造を用いたダイヤモンド NV 中心の電荷状態制御」, 第 29 回ダイヤモンドシンポジウム, P2-31, 東京理科大学 葛飾キャンパス, 東京, 2015 年 11 月 18 日.

2. ○岩崎孝之, 石橋史隆, 宮本良之, 土井悠生, 小林悟士, 宮崎剛英, 長町信治, 犬伏俊郎, 水落憲和, 波多野睦子, 「ダイヤモンド中の単一ゲルマニウム-空孔センター」, 第 76 回応用物理学会秋季学術講演会, 15p-4F-24, 名古屋国際会議場, 名古屋, 2015 年 9 月 15 日.

3. ○土井悠生, 「Pure negatively charged state of NV center in n-type diamond」, 関西地区スピントロニクス研究室合同ゼミナール, P12, 大阪大学豊中キャンパス, 大阪, 2015 年 9 月 2 日.

4. ○ 土井悠生, 福井貴大, 加藤宙光, 牧野俊晴, 山崎聡, 田嶌俊之, 森下弘樹, 三輪真嗣, Fedor Jelezko, 鈴木義茂, 水落憲和, 「リンドナーによるダイヤモンド NV 中心の電荷状態制御」, 第 62 回応用物理学会春季学術講演会, 11p-C1-14, 東海大学湘南キャンパス, 神奈川, 2015 年 3 月 11 日.

5. ○ 宮崎剛英, 宮本良之, 牧野俊晴, 加藤宙光, 山崎聡, 福井貴大, 土井悠生, 徳田規夫, 波多野睦子, 水落憲和, 「ダイヤモンド (111) 基板における窒素-空孔複合欠陥の配向整列機構」, 第 62 回応用物理学会春季学術講演会, 11p-C1-13, 東海大学湘南キャンパス, 神奈川, 2015 年 3 月 11 日.

6. ○ 福井貴大, 土井悠生, 宮崎剛英, 宮本良之, 加藤宙光, 松本翼, 牧野俊晴, 山崎聡, 森本隆介, 徳田規夫, 波多野睦子, 坂川優希, 森下弘樹, 田嶌俊之, 三輪真嗣, 鈴木義茂, 水落憲和, 「ダイヤモンド中 NV センターの選択的な一軸方向制御」, 第 28 回ダイヤモンドシンポジウム, 107, 東京電機大学, 東京, 2014 年 11 月 19 日.

7. ○ 福井貴大, 土井悠生, 宮崎剛英, 宮本良之, 加藤宙光, 松本翼, 牧野俊晴, 山崎聡, 森本隆介, 徳田規夫, 波多野睦子, 坂川優希, 森下弘樹, 田嶌俊之, 三輪真嗣, 鈴木義茂, 水落憲和, 「ダイヤモンド中 NV センターの選択的な一軸方向制御」, 第 75 回応用物理学会秋季学術講演会, 17p-A8-5, 北海道大学, 札幌, 2014 年 9 月 17 日.

8. ○ 土井悠生, 牧野俊晴, 加藤宙光, 竹内大輔, 小倉政彦, 大串秀世, 森下弘樹, 田嶌俊之, 三輪真嗣, 山崎聡, P. Neumann, J. Wrachtrup, 鈴木義茂, 水落憲和, 「電気的手法によるダイヤモンド中の単一 NV 中心の電荷状態制御」, 第 69 回日本物理学会, 28aCC-5, 東海大学湘南キャンパス, 神奈川, 2014 年 3 月 28 日.

9. ○Y. Doi, T. Makino, H. Kato, M. Ogura, D. Takeuchi, H. Okushi, H. Morishita, T. Tashima, S. Miwa, S. Yamasaki, P. Neumann, J. Wrachtrup, Y. Suzuki and N. Mizuochi, *Deterministic electrical charge state control of NV center in diamond*, KAKENHI Quantum Cybernetics Winter Meeting 2013, PO24–3, ハイアットリージェンシー京都, 京都, 2013 年 12 月 16–17 日.

10. ○ 土井悠生, 牧野俊晴, 加藤宙光, 小倉政彦, 竹内大輔, 大串秀世, 山崎聡, J. Wrachtrup, 田嶌俊之, 三輪真嗣, 鈴木義茂, 水落憲和, 「pin ダイヤモンド半導体への電流注入による単一 NV 中心の電荷制御」, 第 27 回ダイヤモンドシンポジウム, 102, 日本工業大学, 埼玉, 2013 年 11 月 20 日.

11. ○ 土井悠生, 牧野俊晴, 加藤宙光, 小倉政彦, 竹内大輔, 大串秀世, 山崎聡, J. Wrachtrup, 三輪真嗣, 鈴木義茂, 水落憲和, 「ダイヤモンド中の単一 NV 中心における電荷状態の電気的制御」, 第 60 回応用物理学会春季学術講演会, 27p-A6-2, 神奈川工科大学, 神奈川, 2013 年 3 月 27 日.

12. ○ 土井悠生, 牧野俊晴, 加藤宙光, 小倉政彦, 竹内大輔, 大串秀世, 山崎聡, J. Wrachtrup, 三輪真嗣, 鈴木義茂, 水落憲和, 「pin ダイヤモンド半導体への電流注入による単一 NV 中心の電荷制御」, 第 26 回ダイヤモンドシンポジウム, 206, 青山学院大学青山キャンパス, 東京, 2012 年 11 月 20 日.

13. ○ 土井悠生, 牧野俊晴, 加藤宙光, 小倉政彦, 竹内大輔, 大串秀世, 山崎聡, J. Wrachtrup, 三輪真嗣, 鈴木義茂, 水落憲和,「ダイヤモンド中の単一 NV 中心における電荷状態の電気的制御」, 第 73 回応用物理学会秋季学術講演会, 13p-C12-21, 愛媛大学, 愛媛, 2012 年 8 月 13 日.

14. ○Y. Doi, T. Makino, H. Kato, M. Ogura, D. Takeuchi, H. Okushi, S. Yamasaki, J. Wrachtrup, S. Miwa, Y. Suzuki and N. Mizuochi, *Single Photon, Spin, and Charge in Diamond Semiconductor at Room Temperature*, KAKENHI Quantum Cybernetics Summer Meeting 2013, PO24–3, ＷＴＣコンファレンスセンター, 東京, 2012 年 7 月 11–12.

15. ○ 土井悠生, 三輪真嗣, J. Wrachtrup , 鈴木義茂, 水落憲和, 「SiC 単結晶および微粒子における光検出磁気共鳴」, 第 59 回応用物理学会春季学術講演会, 16a-B11-5, 早稲田大学, 東京, 2012 年 3 月 16 日.

16. ○ 水落憲和, 土井悠生, 下岡孝明, 森周太, 牧野俊晴, 加藤宙光, 小倉政彦, 竹内大輔, 大串秀世, M. Nothaft, J. Wrachtrup, 山崎聡,「ダイヤモンド半導体中の単一 NV 中心を用いた量子情報の研究」, 第 50 回電子スピンサイエンス学会年会 (SEST2011), 3A-05, 仙台国際センター, 仙台, 2011 年 11 月 18 日.

List of Awards and Grants

1. 第 33 回 (2012 年秋季) 応用物理学会講演奨励賞 (2013 年 3 月 27 日)
2. 大阪大学大学院基礎工学研究科賞 (2013 年 3 月 25 日)
3. ICDCM2014 Gold Young Scholar Award (September 10, 2014, Madrid)
4. 得居奨励金 (2013 年 3 月 25 日, 於:大阪大学)
5. シグマ RA (2014 年 9 月 1 日–2015 年 2 月 28 日, 於:大阪大学)
6. 平成 25 年度 (第 2 回) 若手研究者支援事業 (2014 年 7 月 23 日, 於:大阪大学)
7. JSPS (Japan Society for the Promotion of Science) Research Fellowships for Young Scientists (DC2) with JSPS KAKENHI Grant Number 15J05801, (April 1, 2015 – March 31, 2016)